Integrated Control of Solidification Microstructure and Melt Pool Dimensions in Additive Manufacturing of Ti-6Al-4V

Submitted in partial fulfillment of the requirements for

the degree of

Doctor of Philosophy

in

Mechanical Engineering

Joy E. Gockel

B.S., Mechanical Engineering, Wright State University
M.S., Mechanical Engineering, Wright State University

Carnegie Mellon University
Pittsburgh, PA

May, 2014

Dedication

This dissertation is dedicated to:

My husband, Brian

and

My parents, Doug and Nancy

Acknowledgements

First I would like to acknowledge my advisor, Professor Jack Beuth (chair) for his mentorship and guidance throughout my dissertation research. I am also grateful to the members of my thesis committee, Professor Fred Higgs, Professor Anthony Rollett and Professor Nathan Klingbeil. All of whom have provided valuable insight and advice.

I am very grateful to the organizations that have provided the funding for my dissertation work. This Ph.D. research was sponsored by the National Defense Science and Engineering Graduate (NDSEG) Fellowship, the National Science Foundation under grant CMMI-1131579 and the John and Claire Bertucci Fellowship.

The very nature of this project is very interdisciplinary and collaborative, so I must acknowledge those who have contributed to this research. I would like to thank my colleague and friend, Jason Fox for being a discussion partner and for graciously contributing his finite element models and several melt pool dimension process maps for use in this dissertation. I would also like to thank the other members of the Beuth group who have been present during my time at Carnegie Mellon: Colt Montgomery, Sneha Prabha Narra, Zachary Francis, Daniel Christiansen, Piyapong Reeseewat, Rui Yang, Haipeng Qiao and Amin Anvari. All of you have assisted my research in some way and have made my time at Carnegie Mellon a fun, collaborative experience. A special thanks to several CMU material science students for their much needed experiment sample preparation help: Brian Gockel, Brian Lin and Stephanie Bojarski.

I must also acknowledge the collaborators who have provided experimental samples as well as expert advice guiding this research. Karen Taminger, Rob Hafley, Chris Domack, and Richard Martin from NASA Langley Research Center for work related to the EBF3 process. Ola

Harryson, Harvey West, Tim Horn and Ron Aman from North Carolina State University for the Arcam samples, images and expertise. Heather Doak, John Thompson and Nathan Klingbeil from Wright State University for discussions and contributions to the experimental analysis.

I would like to thank my husband, Brian. He has been a great help, both professionally and personally. He has proofread documents, and helped polish samples. I greatly appreciate everything that he does to make life better and for keeping me sane during the whole PhD process. I would also like to thank my family, especially my parents, for all of their support. Lastly, like to thank my pups, Joule and Newton for their companionship and support.

Abstract

Additive manufacturing (AM) offers reduced material waste and energy usage, as well as an increase in precision. Direct metal AM is used not only for prototyping, but to produce final production parts in the aerospace, medical, automotive and other industries. Process mapping is an approach that represents process outcomes in terms of process input variables. Solidification microstructure process maps are developed for single bead and thin wall deposits of Ti-6Al-4V via an electron beam wire feed and electron beam powder bed AM process. Process variable combinations yielding constant beta grain size and morphology are identified. Comparison with the process maps for melt pool geometry shows that by maintaining a constant melt pool cross sectional area, a constant grain size will also be achieved. Additionally, the grain morphology boundaries are similar to curves of constant melt pool aspect ratio. Experimental results are presented to support the numerical predictions and identify a proportional size scaling between beta grain widths and melt pool widths. Results demonstrate that *in situ,* indirect control of solidification microstructure is possible through direct melt pool dimension control. The ability to control solidification microstructure can greatly accelerate AM process qualification potentially allow for tailored microstructure to the desired application.

Table of Contents

List of Tables

List of Figures and Illustrations

Chapter 1 Introduction

The development of additive manufacturing (AM), or 3D printing, has revolutionized the manufacturing paradigm. AM begins with a computer aided design (CAD) model, which is translated to a layered model. The layered model is used to deposit material layer-by-layer building a near net shape part [1]. Compared to conventional manufacturing methods, AM offers reduced material waste and energy usage, as well as an increase in precision [2,3,4]. With the introduction of direct metal AM processes, AM is used not only for prototyping, but to produce final production parts for aerospace, medical, automotive and many other applications [1].

While AM offers the promise of increased efficiency and flexibility compared to conventional manufacturing, widespread commercialization of AM processes require the ability to predict and control melt pool dimensions and solidification microstructure in terms of process variables. Process maps have been developed to control melt pool dimensions through a wide range of processing variables [5]. However, the ability to correctly deposit a part is not sufficient if the microstructure and resulting mechanical properties of the completed part are not suitable for the desired application [6]. Ti-6Al-4V is an attractive alloy for many aerospace and medical applications. The mechanical properties of Ti-6Al-4V are dependent on the solidification microstructure (grain size and morphology) [7,8], which is controlled by the thermal conditions at the onset of solidification [9].

Process mapping is an approach that plots process outcomes as a function of key identified primary process input variables. This approach allows for understanding and

expansion of processing space. The process mapping approach identifies five primary process variables that are of greatest importance in any thermally based AM process. These process parameters are heat source power, heat source travel velocity, material addition rate, background or initial temperature of the part and part geometry. The effect of the primary process variables on a specified process outcome is then presented in a two-dimensional plot of absorbed heat source power (P) vs. heat source velocity (V) to create a P-V map [10,11,12,13]. The process outcomes of interest in this study are the melt pool geometry and solidification microstructure. Once the primary process variables are mapped, additional studies can be completed on the role of any other secondary process variables that are identified [5].

In this work, the prediction and control of solidification microstructure in terms of process variables in direct metal additive manufacturing is explored. Process maps are first presented for single bead deposits in an electron beam wire feed system. Using a previously developed solidification map for Ti-6Al-4V [14] and thermal conditions from analytical and numerical models, the curves of constant cooling rate and the grain morphology boundaries are plotted in power versus velocity space to create the P-V process map for solidification microstructure of Ti-6Al-4V. The solidification microstructure process map is related to the process map for controlling melt pool dimensions [15]. Experiments are used to assess the melt pool area, beta grain size and morphology predictions. The work is then extended to encompass additional geometries and types of AM processes. Results show that connections can be drawn between the process maps for melt pool dimension and solidification microstructure control. These results provide the potential for in situ microstructure control via direct observation and control of melt pool dimensions.

1.1 Motivation and Applications

Additive manufacturing (AM) is an attractive process for aerospace applications. For small batch production, AM incurs minimal initial cost compared to traditional manufacturing processes such as casting. AM can also be used to decrease initial costs for large components with detailed features [3]. Typically, an engine block is created through subtractive manufacturing by forging a large block and then machining away material to form detailed features. Significant machining of large forged components requires additional time, and creates significant amounts of material waste. By using AM, a simple forging can be manufactured with subsequent detailing done by adding material through additive manufacturing [16]. Additive manufacturing can also be used for repair of cracks or worn components to extend the service life of a part [17].

An example application of AM is the fuel nozzle in the General Electric (GE) Leading Edge Aviation Propulsion (LEAP) engine. The redesigned fuel nozzle cannot be manufactured using traditional methods; it can only be created by AM. The new design was able to combine twenty parts into one, which reduced the complexity of the qualification process. The weight was also reduced by 25% and the part is 5 times more durable, thus increasing the life of the component. With 19 fuel nozzles per engine, GE Aviation proposes a weight reduction of up to 1000 pounds in a single engine through additive production [18].

Gas turbine engines components are a common aerospace application for Ti-6Al-4V, though it is also used structurally for brackets, fittings, propulsion tubing lines and support tubes [19]. Additive manufacturing of Ti-6Al-4V is also used in various medical and automotive

applications [20]. Medical applications include custom bone and joint implants. AM provides the capability to mimic the stiffness of bone by tailoring material properties. This improves the biocompatibility of the metal implants and improves the bonding between bone and implant [21].

1.2 Direct Metal Additive Manufacturing

Numerous specific processes fall under the blanket term additive manufacturing. Typical power sources are either laser or electron beams. Added material can be fed in the form of a wire or powder, or selectively melted from a bed of powder. Additive manufacturing can also refer to polymer and ceramic manufacturing processes, however, results in this document are limited to direct metal additive manufacturing. Direct metal additive manufacturing refers to any additive manufacturing process depositing metallic material into a pool of molten material. Direct metal additive manufacturing is divided into two main categories in which the four specific processes discussed here fall: directed energy deposition (electron beam wire feed and laser beam powder stream) and powder bed fusion (electron beam powder bed and laser beam powder bed) [22,23]. These process span from small scale to large-scale processes. The deposition rates for each process are listed in Table 1.1 and a description of each process is included in the following sections. This work focuses on the electron beam wire feed process and the electron beam powder bed process, however the approach can be extended to all types of direct metal additive manufacturing processes.

Process	Deposition Rate (cm^3/hr.)
Electron Beam Wire Feed	1138-2500 [24,25]
Laser Beam Powder Stream	16-230 [26]
Electron Beam Powder Bed	60-80 [27,28]
Laser Beam Powder Bed	4-35 [29,30,25]

Table 1.1: Deposition rates of direct metal additive manufacturing processes

1.2.1 Electron Beam Wire Fed Additive Manufacturing Process

The Electron Beam Freeform Fabrication (EBF^3) system was developed by the National Aeronautics and Space Administration (NASA) at Langley Research Center and is an example of an electron beam wire fed process. The EBF^3 process is a modified Sciaky machine [31]. The EBF^3 process uses an electron beam as the power source with a wire feed for depositing material, similar to the welding process. The substrate moves under the beam at a specified direction and velocity to create the shape of the part. The wire then moves up and the next layer is deposited [3].

1.2.2 Laser Beam Powder Stream Process

Laser engineered net shaping (LENS™) is an example of a laser beam powder fed additive manufacturing process. The LENS™ process was developed at Sandia National Laboratories and was made commercially available by Optomec Design Company in 1997. The LENS™ process begins with a laser beam creating a melt pool on the substrate and injecting powder particles into the melted material [16,32].

1.2.3 Electron Beam Powder Bed Process

A powder bed AM process is one where a heat source melts powder particles within a large bed of powder. An example of an electron beam powder bed process is the Arcam process. This process starts with a bed of metal powder in a vacuum, and then uses an electron beam to selectively melt the powder for the first layer of a part. The build platform then moves down the amount of one layer thickness and a new layer of powder is spread across the top and this process repeats to build the part through many layers. The bed of powder is held at an optimal elevated temperature, depending on the material used, to reduce residual stresses, avoid martensitic grain structures and to hold powder particles together when the high momentum electron beam hits the bed [33,34].

1.2.4 Laser Beam Powder Bed Process

There are many different companies providing different types of laser powder bed processes. However, they all deposit in a way similar to the electron beam powder bed process. This process also begins with a bed of metal powder and then uses a laser beam to melt the powder particles. The build platform then moves down a distance of one layer, and a new layer of powder is spread across the top. This melting and spreading process repeats to builds the part layer by layer. The process is performed in an inert gas environment [35].

1.3 Material

Many different materials can be used in AM processes. The material used in this research is the titanium alloy Ti-6Al-4V, which consists of Titanium, 6% Aluminum, and 4% Vanadium.

Ti-6Al-4V is an attractive material for the aerospace industry because of its lightweight, high strength properties, excellent behavior at high temperatures, corrosion resistance and composite compatibility [36,37]. Out of the alpha-beta titanium alloys, Ti-6Al-4V has the best weldability, making it an attractive material for AM. This is due to the fact that the more desirable Widmanstätten structure is typically formed even at the relatively high cooling rates that occur during the welding process. The alpha-prime martensite that forms at even higher cooling rates is not as hard and brittle as in other titanium alloys [38]. Because Ti-6Al-4V is prone to hydrogen embrittlement, AM of Ti-6Al-4V must be performed in a vacuum or inert gas environment [39].

Ti-6Al-4V is a two-phase, alpha-beta alloy where the V stabilizes the beta phase body centered cubic (BCC) crystal structure, while the Al stabilizes the hexagonal close packed (HCP) crystal structure of the alpha phase [40]. When cooling from above the melting temperature, a beta grain structure begins forming once the melting temperature is reached. When the material reaches the beta transus (1270 K), the alpha grains begin growing within the beta grains from the grain boundaries. The cooling rate from the melting temperature (1893 K) determines the beta grain size. Experiments in rapid solidification of Ti-6Al-4V have shown that the cooling rate at the onset of solidification and the beta grain size are related by a power law relationship [41]. This relationship is similar to the relationship theoretically developed for aluminum [42]. The alpha grain size and type can be determined by cooling rates at the beta transus temperature and below [8]. The beta grain morphology of Ti-6Al-4V is determined by the solidification parameters thermal gradient (G) and solidification rate (R) [9,14,43,44].

Many material properties, such as yield strength, are dominated by alpha grain size; however, post process heat treatments are typically used to modify the alpha grain structure. Beta

grain structure typically remains unchanged through traditional heat treatments, and is the dominating factor for other mechanical properties, such as fatigue behavior [7,8]. Therefore it is crucial to obtain suitable as deposited beta grain size and morphology. In this work, solidification microstructure is used to refer to the beta grain size and morphology.

1.4 Solidification Microstructure

Solidification maps are used to predict the resulting microstructure based on the thermal conditions at the onset of solidification. In directional cooling, a front of columnar grain growth moves through the region as the liquid solidifies. Solidified columnar grains are elongated in one direction, in contrast to equiaxed grains that have roughly the same dimension in all directions. The designation of where the columnar to equiaxed transition (CET) occurs is based on an analytical model developed by Hunt for steady state columnar and equiaxed growth. In this model, the equiaxed grains are assumed to form due to heterogeneous nucleation in front of the growth front and an analytical solution is used to examine the grain growth and the interaction with the columnar growth front [45]. In order to have a CET, there must be active nuclei ahead of the columnar front as well as thermal conditions that are favorable to equiaxed growth. The undercooling in front of the columnar front is used to determine the competition between the columnar and equiaxed grains. In castings, which have similar thermal conditions to beam-based additive manufacturing, a lower cooling rate results in a lower thermal gradient. This promotes more equiaxed growth ahead of the columnar front due to a larger undercooled region [46]. Additional models have extended Hunt's work to include a more recent dendritic growth model and investigated the effect of nucleation undercooling temperature and the number of nucleation sites on the CET [47].

The grain morphology curves for beam based manufacturing of Ti-6Al-4V are based on the criterion set forth by Hunt and have been determined through experimental calibration by Kobryn et al. The nucleation parameters were modified in order to fit the morphology region boundaries to the observed microstructure [9]. The solidification map for Ti-6Al-4V is seen in Figure 1.1. The y-axis is the variable G, which is the magnitude of the thermal gradient vector. R is the solidification rate, which is on the x-axis. The solidification rate is defined as the cooling rate divided by G, $R = \frac{1}{G}\frac{\partial T}{\partial t}$. The regions defined on the solidification map correspond to the grain morphology: fully equiaxed, mixed or fully columnar.

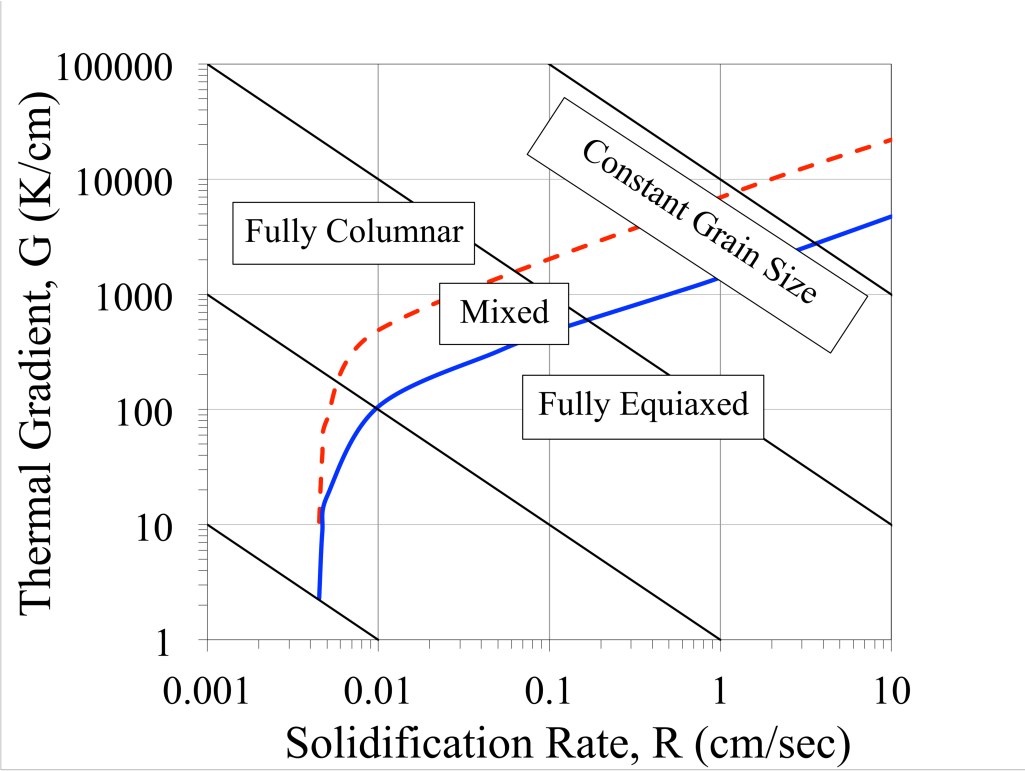

Figure 1.1: Solidification map for Ti-6Al-4V

1.5 Literature Review

In order to replace traditional manufacturing with additive manufacturing, comparable or better than wrought mechanical properties must be obtained. Ti-6Al-4V produced by wire based additive manufacturing has an ultimate tensile strength and strain at failure similar to cast materials when subjected to static tension and high cycle fatigue testing. After heat treatment, the properties are similar to that of wrought material [48,49]. The fatigue limits of additively manufactured Ti-6Al-4V have also been shown to be comparable to cast and even wrought materials [50,51,52]. Porosity in a part can cause a decrease in the mechanical properties of parts produced by wire additive manufacturing. Elongated columnar beta grains typically formed in additive manufacturing can cause anisotropic properties, reducing strength in certain directions [53].

Characterization of the microstructure of a material can be used to draw conclusions about the resulting mechanical properties [7,8]. Many in the material science and manufacturing communities have explored the effect of processing on solidification microstructure produced by additive manufacturing through experimentation and post process microscopy and mechanical testing. The effect of build geometry on the beta grain structure and the texture of electron beam melted Ti-6Al-4V showed that in a bulk section coarse columnar beta grains grow normal to the deposited layers, while in a contour pass, curved columnar grains follow the melt pool surface [54,55]. In selective laser melting, the elongated grains are also affected by the scanning strategy and the part geometry [56]. The effect of melt scan rate shows that an increase in scan rate causes an increase in α'- martensite and a resulting increase in microindentation hardness. Increasing the melt scan rate also increases the potential for porosity caused by unmelted powder pockets

[57]. The effect of distance from the build plate and part size in selective electron beam melting shows that the distance from the build plate has no effect while the part size causes a variation of less than 2% in ultimate tensile and yield strength. The effect of energy input, orientation and location also showed small changes in strength, but orientation causes a large change in percent elongation due to the orientation of the columnar beta grains [58,59]. Though significant insights have been gained through post process experimental characterizations, the results are limited to specific cases and developing trends through post process characterization of material requires much iteration.

Beuth et al. have developed the approach of mapping process outcomes in terms of process variables "process mapping" technique over many years. Process outcomes of interest have included residual stress, melt pool geometry, and microstructure. Residual stress was modeled and measured in both metal and polymer AM processes [60,61,62,63]. Process mapping of the residual stress predicts changes in the final magnitudes of residual stress by using a defined thermal gradient behind the melt pool in thermal simulations [64,65]. The control of steady-state melt pool dimensions for the full range of the LENS® process was investigated by plotting nondimensional melt pool size metrics [66,67,68,69,70,71]. The transient effects on the melt pool geometry for the LENS® have also been investigated using process maps [72]. It has been shown that the melt pool area response can be characterized by a combination of the initial and final melt pool area sizes [73]. The process mapping of melt pool dimensions in steady state has further been extended for the electron beam wire feed system [74]. Recent transient work uses step changes in beam power and velocity to extend this approach to the electron beam wire

feed process showing a similar relationship with melt pool response being related to the initial and final melt pool depths [75].

Ultimately, the microstructure must be determined in terms of process variables in order to control microstructure process relationships. Using analytical and finite element modeling, trends in solidification microstructure can be illustrated using process maps [76,77]. Thermal process maps have been developed for predicting trends in nondimensional thermal conditions and solidification microstructure in terms of process variables for thin wall and bulky geometries. It has been shown that size scale of the AM process has a significant effect on solidification microstructure. At high powers a transition from columnar to equiaxed morphology can occur [78,79,80,81]. For both thin wall and bulky parts, cellular automation modeling has been used to predict the solidification microstructure. Modeling results agreed well with experimental results from both small scale and large-scale beam based deposition processes [82]. A study on the effect of free-edges on melt pool geometry and solidification microstructure showed that there is little effect when approaching an edge. However, there is a large effect when leaving, especially in large power cases when there is a large trailing edge on the melt pool [83,84]. The role of process variables on microstructure and mechanical properties has also been investigated through experimentation and observation of solidification behavior [9,14]. These works predict the microstructure in terms of the investigated process variables independently, whereas it is important to understand the combined effect of important process variables when expanding the processing space.

By determining solidification microstructure in terms of processing parameters, a consistent and predictable microstructure can be obtained. Nickel super alloy applications benefit

from the ability to produce single crystals. Using laser cladding, it has been shown that by controlling processing parameters a fully columnar structure can be obtained so the production of single crystals is possible [85]. Processing-microstructure maps for single crystal deposition have been obtained by using the relationships between local solidification conditions and the resulting solidification microstructure. The local solidification conditions are determined using an analytical heat flux model [86,87]. It is also suggested that for single crystal growth in super alloys, control of the melt pool geometry in a laser glaze can produce a desired growth velocity and microstructure [88].

Modeling methods used in this research have been used throughout the literature. A method used for approximate modeling of a beam-based deposition process is the 3-D Rosenthal solution for a moving point heat source [89]. Dykhuizen and Dobranich first applied the Rosenthal solution to laser based deposition [90,91] and Vasinonta et al. [67] subsequently determined the dimensionless form. Nonlinear finite element modeling of laser deposition processes has also been used to predict steady state melt pool behavior as well as to establish the utility of the Rosenthal solution for predicting trends in solidification microstructure [78,79,80,81,76,77].

1.6 Contributions

In this work, a process mapping approach applicable to the building of 3-D shapes across all direct metal AM processes is used to predict solidification microstructure in terms of two primary process variables (beam power, P and velocity, V). First, the process map for solidification microstructure is created for single bead deposits by an electron beam wire feed

AM process. Solidification microstructure is predicted using the solidification map for Ti-6Al-4V and the cooling rates and thermal gradients from analytical and finite element added material models. The solidification data is used to determine curves of constant cooling rate and the grain morphology boundaries in power versus velocity space, creating the P-V process map for microstructure control. Solidification microstructure predictions are then related to the P-V process map for controlling melt pool dimensions, and the ability for real time indirect microstructure control through melt pool dimension control is explored [15]. Single bead deposit experiments are quantified in order to verify predictions.

For a full understanding of the effect of process variables on the solidification microstructure, additional deposit geometries and types of direct metal additive manufacturing must be explored. The process mapping of solidification microstructure is extended to other deposit geometries and other types of direct metal additive manufacturing processes. Depositing a tall thin wall is investigated. The process maps for solidification microstructure are created for both additional geometries and are compared to the process maps for melt pool dimension control. The solidification microstructure process map for an electron beam powder bed process is also developed. This process map is also compared to the process map for melt pool dimension control. Further extensions of this work are discussed.

The main contributions of this work are:

1. The development of a process mapping approach for solidification microstructure control in direct metal additive manufacturing.

2. Integrated solidification microstructure and melt pool dimension control is identified for single bead deposits in an electron beam wire feed process via process mapping.
3. Process mapping is used to extend the integrated control of solidification microstructure and melt pool geometries to include the deposition of thin walls
4. Process maps have been developed to extend the integrated control of solidification microstructure and melt pool geometries for an electron beam powder bed additive manufacturing process.

1.7 Organization

This thesis is organized into 6 chapters. Chapter 1 includes an introduction of additive manufacturing and motivation behind process mapping of solidification microstructure. A literature review of prior and current work related to this dissertation is included. Chapter 2 introduces the process mapping approach for solidification microstructure. The solidification microstructure process map for single bead deposits of Ti-6Al-4V in an electron beam wire feed additive manufacturing process is given. This process map is related to the process map for melt pool dimensions and the potential for integrated control of solidification microstructure and melt pool dimensions is introduced. Chapter 3 presents the behavior of the thermal conditions at the onset of solidification through the melt pool depth and how this relates to melt pool dimensions.

Chapter 4 extends the solidification microstructure process mapping approach to thin wall geometries. The solidification microstructure process map for thin wall deposits of Ti-6Al-4V is presented and is compared to the process map for melt pool dimensions. Thin wall experiments for several powers and velocities with the same predicted melt pool area are presented to assess the numerical predictions. Chapter 5 extends the integrated process mapping

of solidification microstructure and melt pool dimensions to the electron beam powder bed additive manufacturing process. Single bead no added powder and 1-layer of powder experiments are presented and compared to numerical predictions. The effect of adding powder on solidification microstructure is also discussed.

Chapter 6 presents the major conclusions and contributions from this work. Recommendations for future extensions of this work are presented. Additional experimental images used for measurements are presented in the appendix.

Chapter 2 Solidification Microstructure Process Mapping of Single Bead Deposits in Electron Beam Wire Feed Systems

2.1 Chapter Overview

In direct metal additive manufacturing it is crucial to obtain a consistent solidification microstructure with desirable mechanical properties. A solidification microstructure P-V process mapping procedure is developed in this chapter for the electron beam wire feed AM system. This process mapping approach is the foundation for the work in this thesis. Lines of constant grain size and regions of grain morphology are plotted in P-V space. This process map illustrates the effect of changing process variables on the solidification microstructure of the deposited material.

The following section details the methods used in this research. Material added finite element simulations and an analytical approximation are used to create a process map with curves of constant cooling rate, which corresponds to curves of constant grain size for that point. The boundaries between the columnar, mixed, and equiaxed regions of grain morphology are also identified in P-V space for the point of lowest thermal gradient where the transition will first take place. The result is the solidification microstructure process map for deposition of Ti-6Al-4V in an electron beam wire feed process. The process map for solidification microstructure

control is then compared to the previously developed melt pool dimension process map. This comparison allows for real time control of solidification microstructure by controlling melt pool dimensions. Single bead deposit experiments were performed and compared to the numerical predictions to assess the solidification process mapping procedure and the connections between microstructure and melt pool geometry. Qualitative comparisons are given in this chapter, with further quantification shown in the following chapter.

2.2 Methods

2.2.1 Material Added Finite Element Model

Finite element simulations in the commercial program ABAQUS are used to model single bead deposition and the addition of material by the wire feeder. The FEA model is based on the model developed by Soylemez et al. [74]. The mesh is refined and the mesh biasing adjusted in order to accurately extract the thermal conditions in a reasonable amount of computation time.

Because the deposition takes place in a vacuum, the 3-D models do not include convective heat transfer on their vertical and top surfaces. The surface boundary conditions are insulated. Currently, radiation from the surface is considered negligible [92]. The nodes have an initial temperature of T_0=373 K and a constant temperature of T_0=373 K specified at the base to simulate the ambient atmosphere and a ratio of added material to total material being melted of ϕ = 0.77. Eight-node, linear brick heat transfer elements are used throughout the model. In order to reduce computation time, the model is biased to the region where the material is added. The model takes advantage of the front face being a plane of symmetry with only half of the melt

pool modeled, as seen in Figure 2.1. Temperature-dependent thermal properties and latent heat are included.

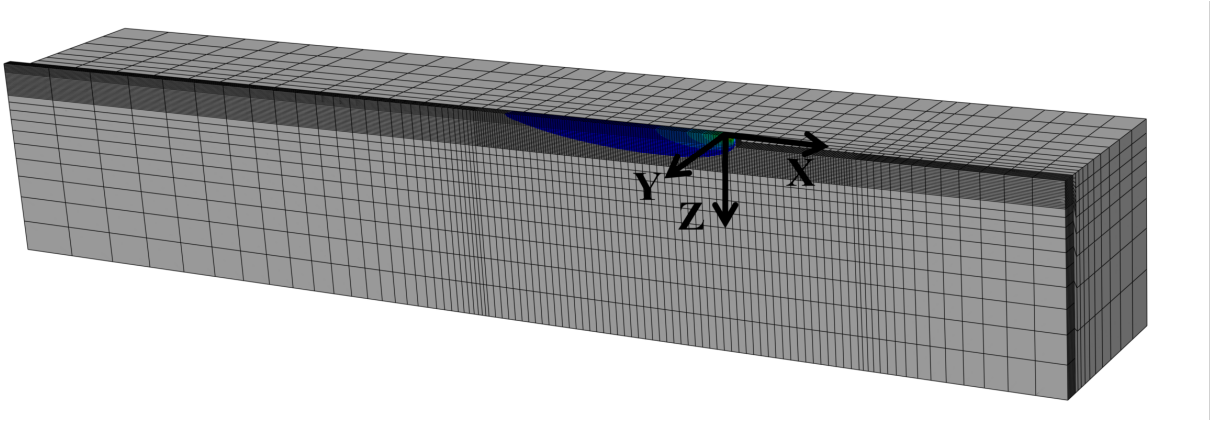

Figure 2.1: Finite element mesh

Material is added ahead of the heat source at each step as the simulation progresses using the model change command as seen in Figure 2.2. A uniform distributed heat flux is applied along the top of the added bead to simulate rapid beam oscillation across the melt pool that is used in the EBF3 process, which reduces the concentration of the heat on the surface. The melt pool travels away from the edge until a steady state is reached and the data is collected. The thermal gradient and cooling rate are obtained as the temperature changes from the liquid to the solid range on the plane of symmetry along the trailing edge of the melt pool as seen in Figure 2.3.

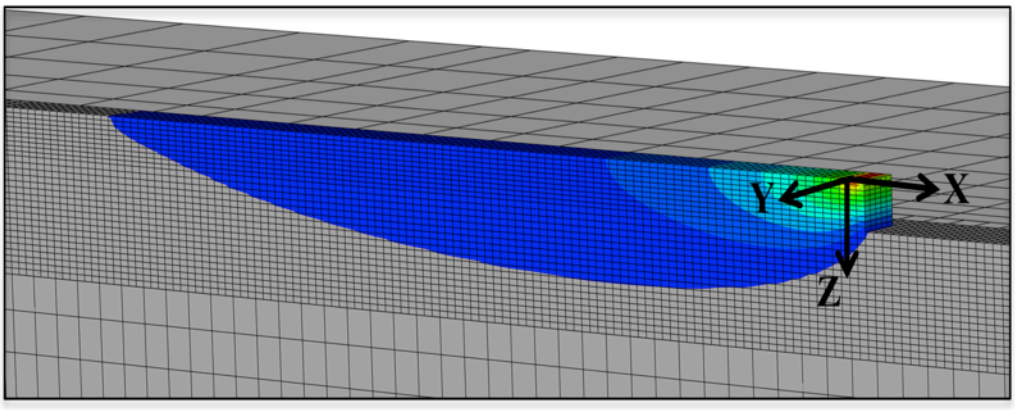

Figure 2.2: Material added to the model

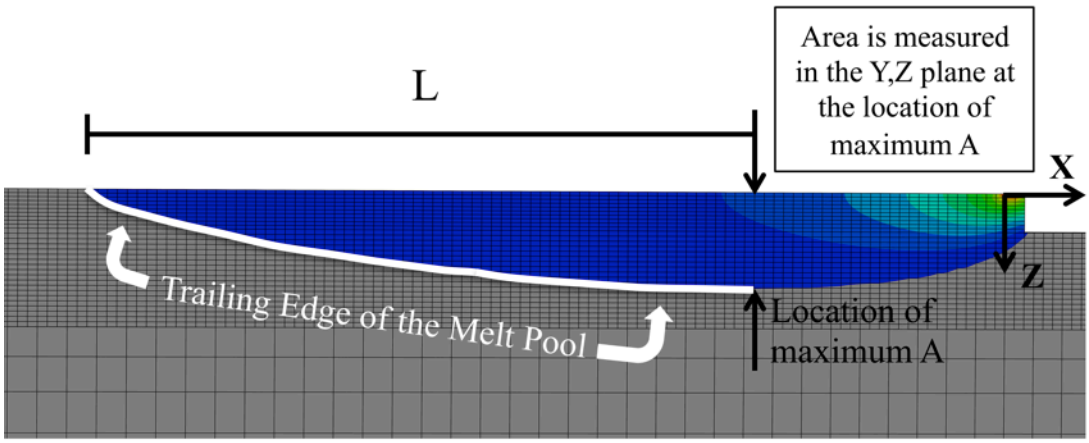

Figure 2.3: Side view along the melt pool boundary on the plane of symmetry

2.2.2 Single Bead Deposit Experiments

Single bead deposit experiments were performed by the NASA Langley Research Center in order to assess predictions. The NASA EBF^3 system is an electron beam system with a wire feed. The experiments performed were deposition of a single bead of Ti-6Al-4V onto a substrate of the same material using various beam powers and velocities. Process variables were chosen for cases with the same predicted melt pool area [74]. Three different areas were investigated and are designated by color: Blue: 10.3mm^2 (0.016in^2), Red: 20.6mm^2 (0.032in^2), and Green: 41.2mm^2 (0.064in^2). The input parameters used in the experiments can be seen in Table 2.1. The experimental plate showing the deposited beads can be seen in Figure 2.4.

Source Power (W)	Absorbed Power (W)	Velocity (in/min)	Velocity (mm/sec)	Wire Feed Rate (in/min)	Wire Feed Rate (mm/sec)
1400	1250	16.1	6.8	63.3	27
1650	1500	21.5	9.1	85	36
2200	2000	31.9	13.5	125	53
3350	3000	52.0	22.0	162	69
4450	4000	68.3	28.9	204	86
5550	5000	85.0	36.0	335	142
1400	1250	5.7	2.4	44.8	19
1650	1500	8.3	3.5	64	27
2200	2000	13.9	5.9	108	46
2800	2500	19.2	8.1	150	63
3350	3000	23.6	10.0	184	78
4450	4000	32.8	13.9	256	108
5550	5000	42.5	18.0	334	141
1650	1500	2.2	0.9	35.4	15
2220	2000	5.2	2.2	81.9	35
3350	3000	10.9	4.6	171	72
5550	5000	19.4	8.2	306	130

Table 2.1: Electron beam wire feed experiment values

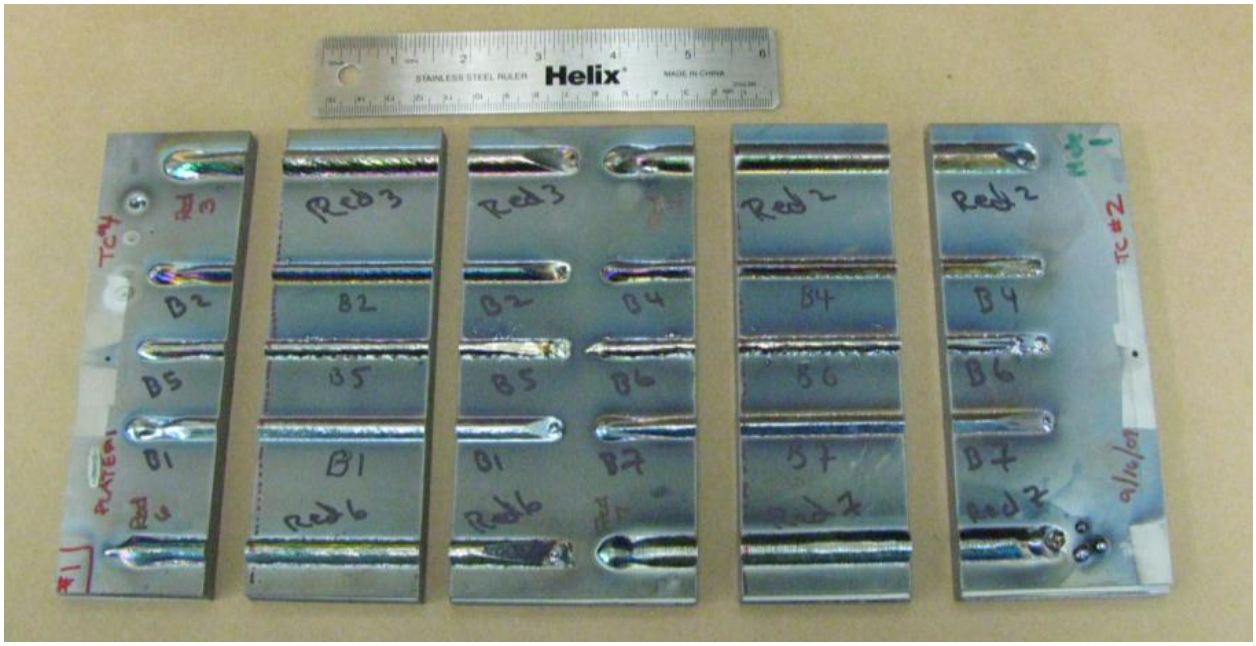

(a)

(b)

Figure 2.4: Electron beam wire feed single bead experiment (a) plate 1 and (b) plate 2

Sectioned specimens were mounted, polished and etched in order to observe the solidification microstructure. The samples were polished and etched using the procedure outlined in Appendix A. The mounted and polished samples can be seen in Figure 2.5. An example micrograph showing the columnar and equiaxed beta grain structure is seen in Figure 2.6.

The beta grain size is measured using the intercept method to obtain the beta grain width [93]. Because columnar grains are elongated in one direction, the grain width is chosen to quantify in order to compare the size of a columnar grain to an equiaxed grain. The width of the columnar grains is measured in the direction perpendicular to the elongated direction. A horizontal line is drawn across the image and a point is counted for each grain boundary that is crossed. A half point is counted for lines ending in the middle of a grain. Dividing the length of the line by the number of points gives the average grain size. This process is repeated throughout the sample and all lines are averaged. Measurements are taken on a two dimensional cross-section and it is assumed that the grain width is the same in the third dimension.

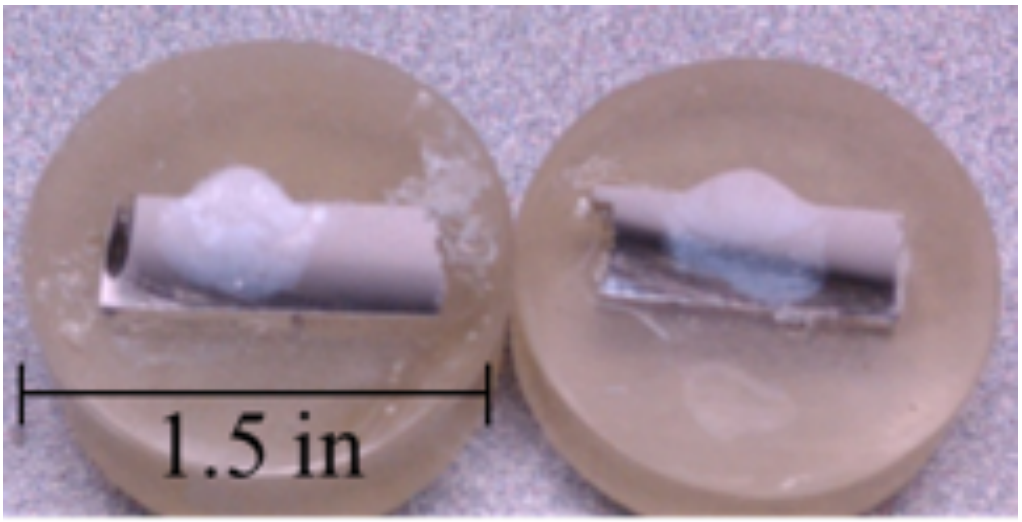

Figure 2.5: Example cross-section samples

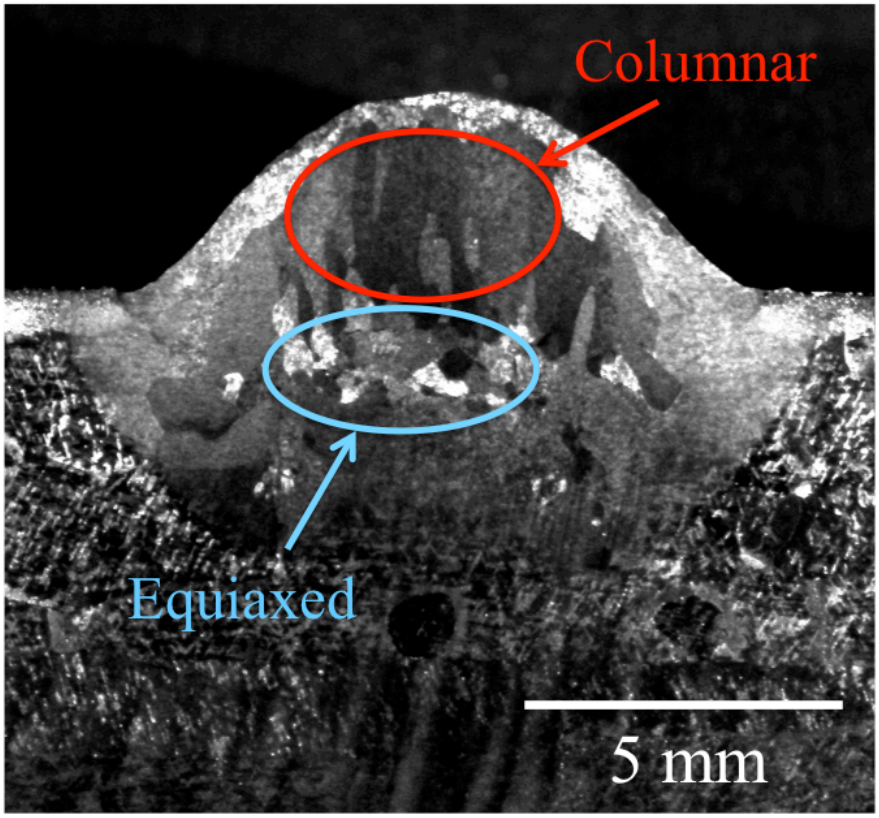

Figure 2.6: Micrograph of melt pool cross section showing grain morphology

2.3 Results

2.3.1 P-V Process Map for Microstructure Control

Solidification maps predict microstructure in terms of thermal gradient and solidification rate, but are difficult to use by process operators. Monitoring the cooling rates and thermal gradients *in situ* is difficult and can only be observed on the surface, so it is rarely done. Even in cases where monitoring of cooling rates and thermal gradients is practical, the solidification map only provides results for individual values of G and R, and does not provide a guide to

controlling solidification microstructure across process variables. Therefore, A P-V process map for solidification microstructure has been developed in order to identify paths through or regions of processing space with constant grain size and different grain morphologies. Absorbed power is a function of the type of process and includes an experimentally determined parameter that accounts for power losses between the power source and the material. For the electron beam powder bed process a value of 0.9 is used as the absorptivity factor [74].

A P-V process map for solidification microstructure is created in order to identify paths or regions of processing space with constant grain size and different grain morphologies. The grain size and morphology data from the G vs. R plot of the solidification map for Ti-6Al-4V in Figure 1.1 [9] is translated onto a plot of power versus velocity in Figure 2.7 using finite element material added simulations. The curves of cooling rate represent doubling the cooling rate, with the lowest cooling rate being on the left side. For one power and velocity combination, the resulting thermal gradients and solidification rates span up to an order of magnitude each along the solidification front. The results presented here are for the top of the melt pool, which is a critical location, where the lowest gradients are present and the transition to a mixed or equiaxed grain morphology will first take place. Therefore, power and velocity combinations yielding thermal conditions for fully equiaxed grains at the top of the melt pool will generally still have thermal conditions yielding columnar grains into the melt pool depth, yielding a deposit with a mix of equiaxed and columnar grains.

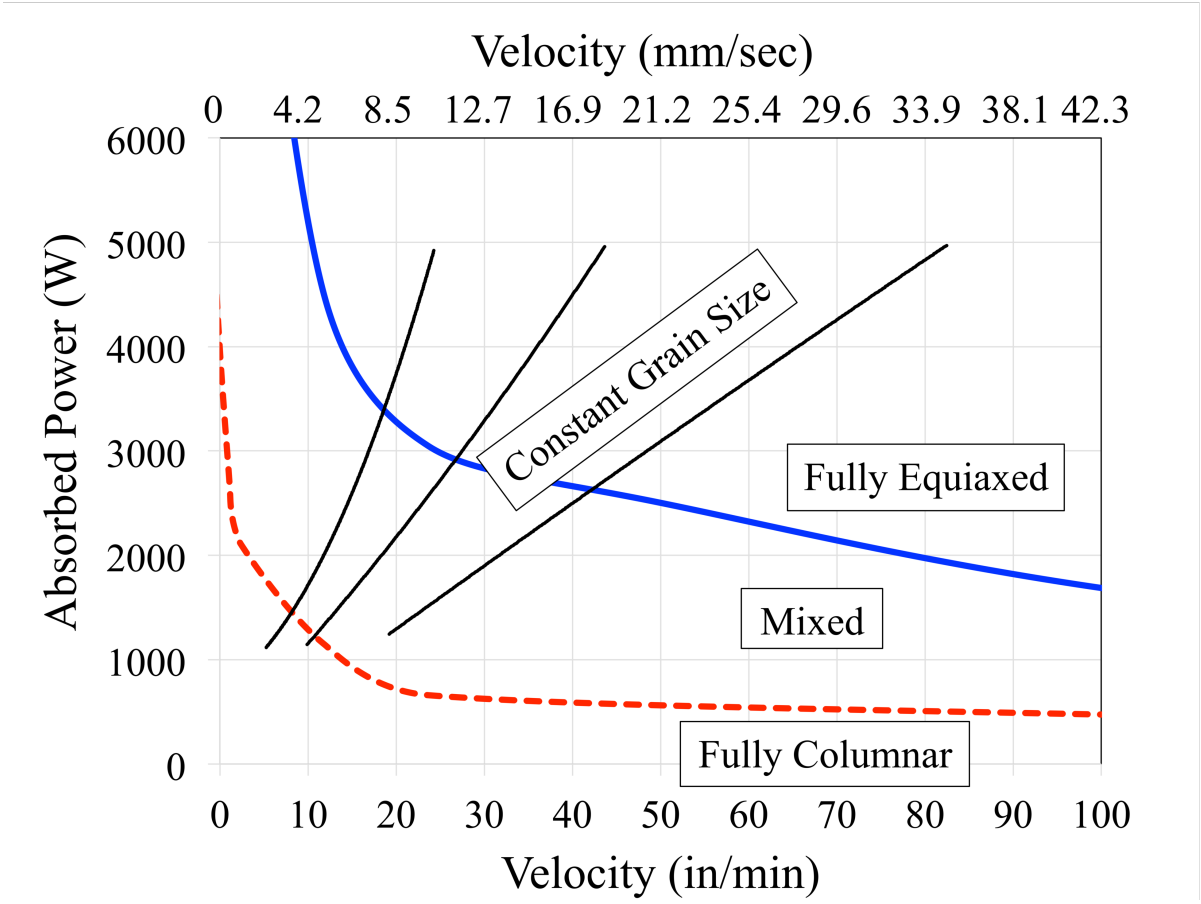

Figure 2.7: The process map for solidification microstructure control in the electron beam wire feed process

The resulting P-V process map for controlling solidification microstructure for single bead deposits of Ti-6Al-4V in an electron beam wire fed process shown in Figure 2.7 (for T_0 = 373K and. ϕ = 0.77). The solid black lines in Figure 2.7 are curves of constant cooling rate. It is possible to maintain a constant grain size while moving from low powers and low velocities, to high powers and high velocities, if the identified path is followed. The dashed line represents the boundary between fully columnar and mixed grain morphology. The boundary between mixed and fully equiaxed grain morphology is the curved solid line. These curves define the boundaries of three regions where columnar, mixed and equiaxed grain morphologies exist.

2.3.2 Integrated Control of Microstructure and Melt Pool Dimensions

Currently, post processing and microscopy is required to observe the solidification microstructure. Resent results by Fox [94] refines the work of Solyemez [74] to create the process map for controlling melt pool area in electron beam wire feed additive manufacturing processes. The previously developed process map for melt pool dimension control is shown in Figure 2.8 [94]. This map is for the geometry of a single bead deposited in the middle of a large part, with T_0 = 373K and a ratio of added material to total material being melted of ϕ = 0.77. Curves of constant melt pool cross sectional area (a melt pool size metric) as well as curves of constant melt pool length to depth ratio (a melt pool shape metric) are plotted in Power vs. Velocity (P-V) space. As indicated in Figure 2.8 the melt pool cross sectional area is the largest melt pool area perpendicular to the travel velocity direction (defined as the x direction in this paper). Melt pool length is the x distance between the location of maximum melt pool cross sectional area and the trailing end of the melt pool. The depth is an effective depth, which is determined from the cross sectional area making the assumption that the area is a semi-circle (the actual depth could also be used, but use of an effective depth yields a direct link to melt pool cross sectional area). By following curves of constant A or L/d, this P-V process map for melt pool dimension control allows these quantities to be maintained across P and V values differing by as much as a factor of 5.

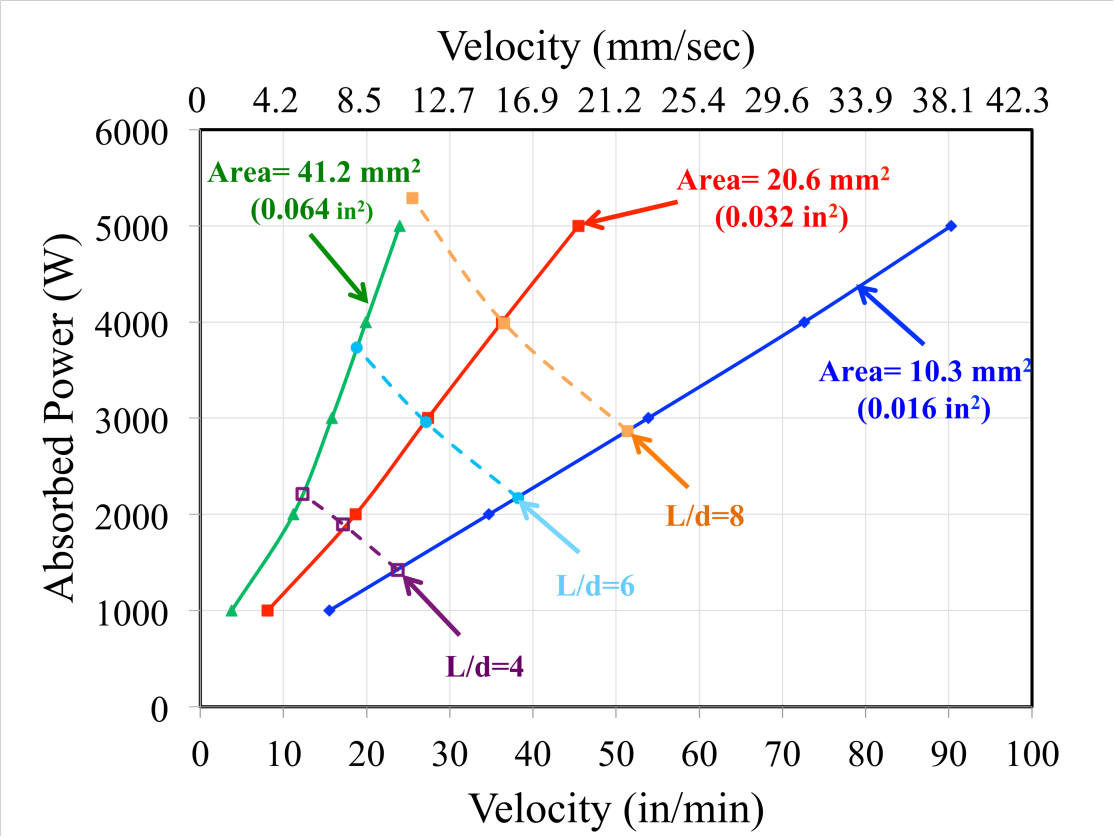

Figure 2.8: The process map for melt pool dimensions in the electron beam wire feed process

When comparing the process map for solidification microstructure in Figure 2.7 to the process map for melt pool dimensions in Figure 2.8, connections can be drawn between the two process maps. The curves of constant grain size are similar to the curves of constant melt pool cross sectional area, A. In other words, by controlling A (which can be related to melt pool width, which is observable in real time during processing), a constant beta grain size is also maintained. The grain morphology region boundaries are similar to curves of constant length-to-depth ratio. The boundary represents the point where the morphology transition will first take place. As a result, an operator can observe the aspect ratio of the melt pool and use that to infer grain morphology.

Melt pool size and shape cannot be independently controlled, with corresponding consequences for microstructure control. While keeping the melt pool area constant and increasing the deposition rate (by increasing P and V), the grain size will remain constant, but the length to depth ratio will become larger and a transition to some equiaxed grains, and then more equiaxed grains will occur. Integration of the solidification microstructure and melt pool dimension process maps allows the ability to indirectly plan and control solidification microstructure by controlling melt pool size and shape in real time. *In situ* microstructure control allows for the potential to tailor the microstructure and the resulting mechanical properties in specific regions of a part build using direct metal AM, with substantially fewer trial and error type tests.

2.3.3 Experimental Analysis

The grain morphology regions and curves of constant grain size are verified using single bead deposit experiments performed by NASA Langley. As seen in Figure 2.9, clear evidence of equiaxed grains is found in experiments within the predicted fully equiaxed region, with the exception of the experimental cases with the smallest melt pool area. Micrographs moving from low power to high power for the melt pool areas of 10.3mm^2 (0.016in^2), 20.6mm^2 (0.032in^2), and 41.2mm^2 (0.064in^2) are seen in Figure 2.10 a, b and c respectively. In general, columnar beta grains are observed, with more equiaxed grains present as the power is increased and the area remains constant. It should be noted that the substate used in these experiments was a laminated Ti-6Al-4V plate, yielding a layered appearance to the substrate in some of the micrographs. Grain morphology behavior through the melt pool depth will be discussed further in Chapter 3.

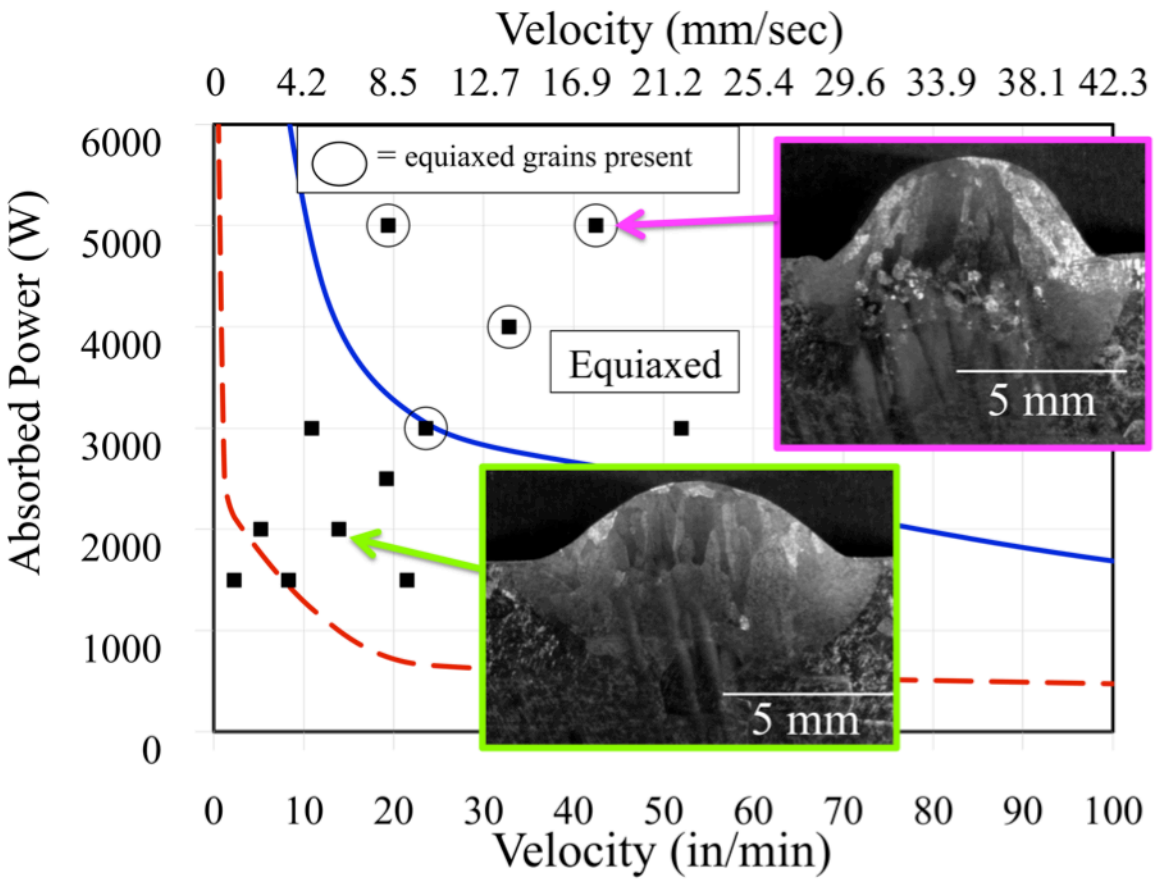

Figure 2.9: Identification of melt pools with equiaxed grains

Qualitative observations of Figure 2.10 indicate that the beta grain size remains constant for power and velocity combinations with the same melt pool area. Furthermore, the micrographs for different melt pool areas, which are scaled to make the melt pool areas roughly the same size (though they differ over a factor of 4), also have beta grains that appear to be similarly sized. This suggests that the beta grain sizes are scaling with the sizes of the melt pool areas. The beta grain widths have been measured, and measurements have been averaged for cases with the same melt pool area. The average beta grain width is plotted against the average experimentally measured effective melt pool width in Figure 2.11 with error bars showing the full range of measured results. The data points tend to fall on a straight line, indicating a constant ratio of beta

grain width to effective melt pool width. In all experimental cases, approximately 20 beta grains are seen across the melt pool width.

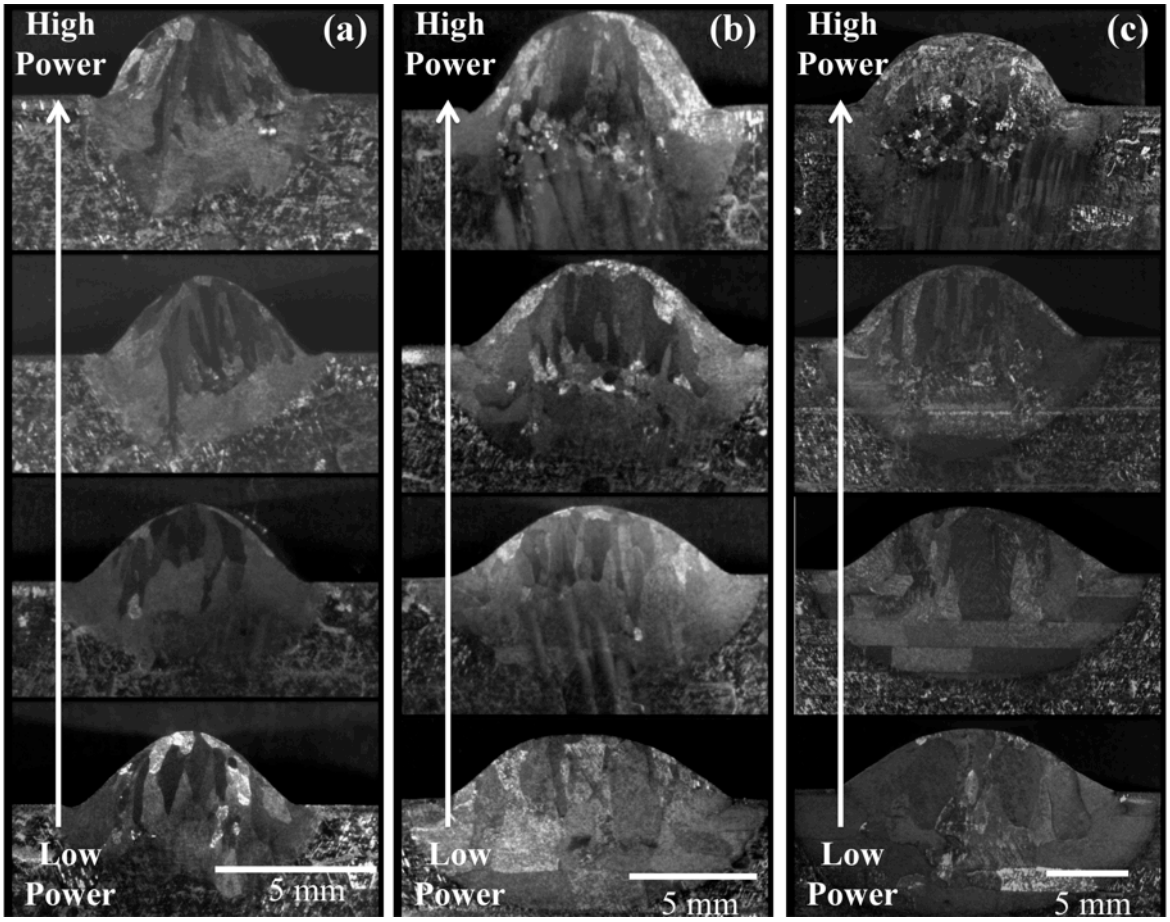

Figure 2.10: Solidification microstructure for melt pool cross sectional areas (a) $0.016in^2/10.3mm^2$ (b) $0.032in^2/20.6mm^2$ and (c) $0.064in^2/41.2mm^2$

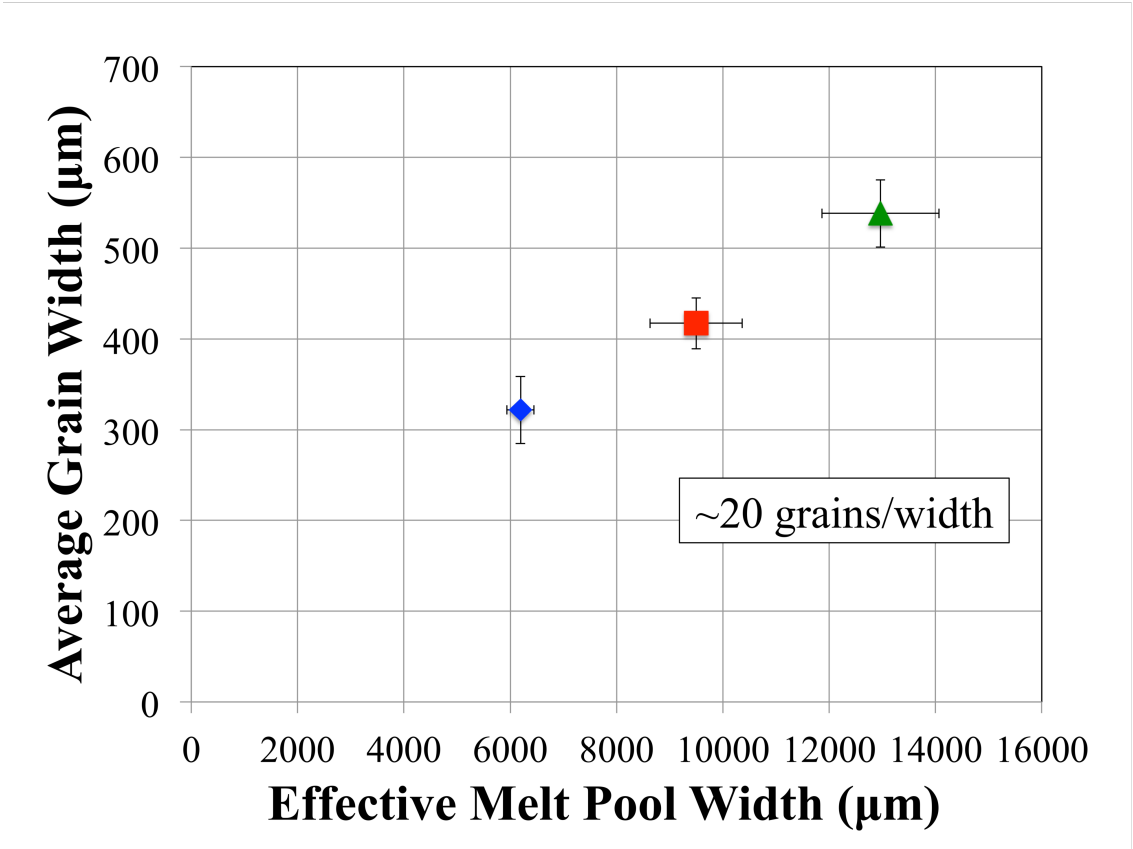

Figure 2.11: Beta grain size scaling with melt pool width

2.4 Chapter Summary

Part and process qualification is an important concern within the AM field. This chapter gives related insight into regions of processing space that can produce desired solidification microstructures. A P-V process map has been created for single bead deposition of Ti-6Al-4V, which predicts solidification microstructure in terms of process variables. Curves of constant beta grain size and regions of grain morphology are identified in beam power versus velocity space.

Comparing the microstructure process map to the process map for controlling melt pool dimensions exposes relationships that can potentially be used to indirectly control solidification microstructure through melt pool dimension control. Results demonstrate that a constant melt pool cross sectional area results in a constant grain size throughout processing space for the electron beam wire feed process. Similarly, monitoring the melt pool length to depth ratio can be used to control the grain morphology. Experimental results support the numerical predictions. Along a line of constant area, increased power results in an increase in the population of equiaxed grains with a constant grain size. Additionally, increasing the melt pool area increases the grain size.

Chapter 3 Thermal Behavior Through the Melt Pool Depth

3.1 Chapter Overview

The solidification microstructure process map and the integrated control of solidification microstructure and melt pool geometry present valuable insight for process development. However, the results presented are for one point in the melt pool, and do not tell the whole story. Results shown in Chapter 2 for grain size and morphology are for the top of the melt pool contour, where thermal gradients are the lowest and morphology transitions will first take place, but the thermal conditions span a large range through the depth of the melt pool.

This chapter will investigate the behavior of the thermal conditions through the depth of the melt pool, which will give insight into the consistency of the microstructure across the entire melt pool cross section. Trends in thermal conditions are developed using material added finite element simulations and an analytical approximation fitted to the numerical solution. The cooling rate, magnitude of the thermal gradient, and the individual components of the thermal gradient are investigated.

3.2 Methods

3.2.1 Material Added Finite Element Models

The material added finite element models outlined in Chapter 2 are also used in this chapter. The finite element models take a significant amount of time to complete when using the high mesh resolution needed in order to accurately capture the thermal conditions through the depth of the melt pool. For this chapter, the finite element simulations are used to fit an analytical approximation, which is outlined in the following section. This allows for the development of trends in the thermal conditions at a higher resolution through the depth of the material.

3.2.2 Analytical Approximation

The 3-D Rosenthal closed form solution is used to guide the finite element modeling. The Rosenthal solution gives the temperature field around a moving point heat source. The finite element models are used to fit the constant material properties of the Rosenthal solution to accurately predict the desired quantity, which in this case is the solidification microstructure. The Rosenthal solution assumes a point heat source, with no material added, constant material properties and no latent heat. This study considers the bulky 3-D geometry of Figure 3.1, in which the process variables of interest are the absorbed beam power αQ and velocity V. It is assumed that the height h, length L and width b are sufficiently large such that the steady-state Rosenthal solution for a moving point source of heat applies.

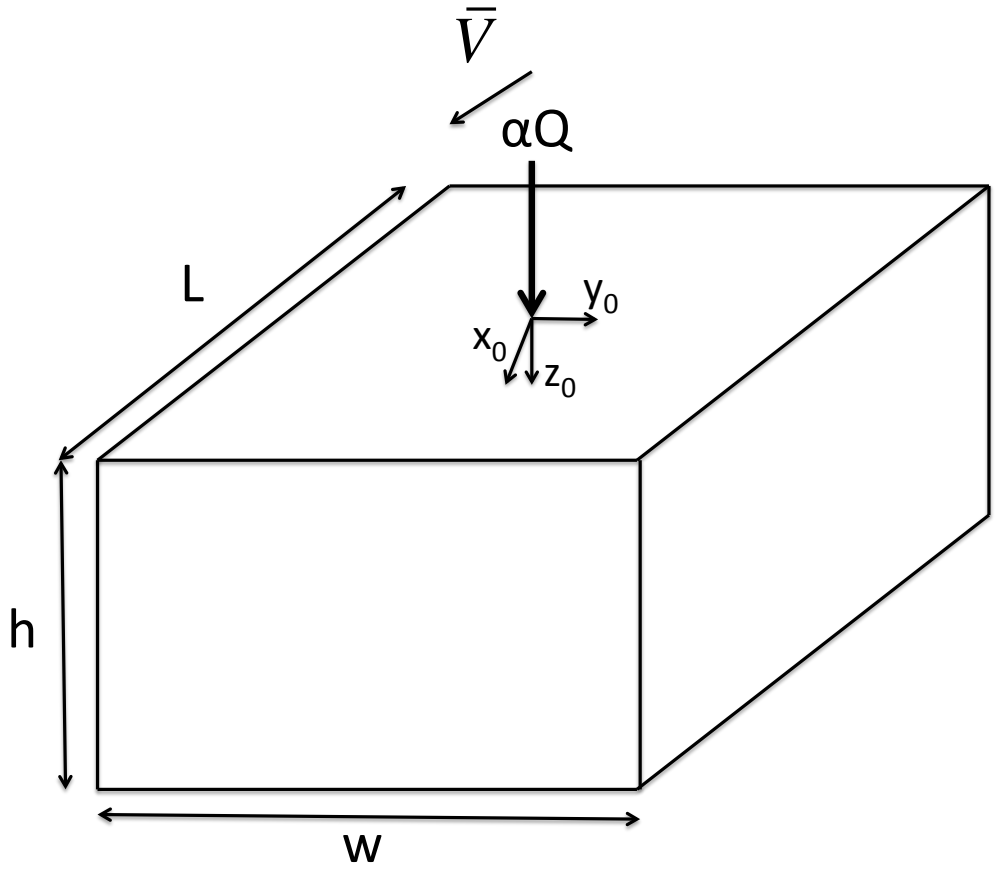

Figure 3.1: 3D Rosenthal geometry

Relative to the position of the point heat source, the nondimensional temperature field is given by Vasinonta et al. [71] as,

$$\bar{T} = \frac{e^{-\left(\bar{x}_0+\sqrt{\bar{x}_0^2+\bar{y}_0^2+\bar{z}_0^2}\right)}}{2\sqrt{\bar{x}_0^2+\bar{y}_0^2+\bar{z}_0^2}}. \tag{3.1}$$

The dimensionless variables of the temperature equation are defined in terms of the process parameters and thermal properties as,

$$\bar{x}_0 = \frac{x_0}{2k/\rho cV}, \bar{y}_0 = \frac{y_0}{2k/\rho cV}, \bar{z}_0 = \frac{z_0}{2k/\rho cV}, and\ \bar{T} = \frac{T-T_0}{\left(\frac{\alpha Q}{\pi k}\right)\left(\frac{\rho cV}{2k}\right)}.$$

In the above normalizations, T is the temperature at a location (x_0, y_0 ,z_0) relative to the moving point heat source and T_0 is the initial temperature of the wall. The relative coordinates (x_0, y_0 ,z_0) are related to fixed spatial coordinates (x,y,z) at any time t as (x_0, y_0 ,z_0) =(x-Vt,y,z), where V is the velocity of the beam. The thermal properties ρ, c and k are the density, specific heat and thermal conductivity of the material respectively, which are assumed to be temperature-independent. αQ is the absorbed power of the heat source. The melt pool is assumed to be symmetric so y_0 is set to 0 when analyzing the thermal conditions.

The solidification microstructure of deposited metals depends on cooling rates and thermal gradients at the onset of solidification (i.e., along the trailing edge of the melt pool). The trailing edge of the melt pool is where solidification occurs. In the Rosenthal solution, T_m is set equal to the melting temperature of the material and nondimensionalized as

$$\bar{T}_m = \frac{T_m - T_0}{\left(\frac{\alpha Q}{\pi k}\right)\left(\frac{\rho c V}{2k}\right)}.$$

Expressions for the dimensionless cooling rate and thermal gradient can be obtained by analytical differentiation of equation 1. The cooling rate is given as

$$\frac{\overline{\partial T}}{\overline{\partial t}} = \frac{e^{-\left\{(\bar{x}-\bar{t})+\sqrt{(\bar{x}-\bar{t})^2+\bar{y}_0^2+\bar{z}_0^2}\right\}}}{2\sqrt{(\bar{x}-\bar{t})^2+\bar{y}_0^2+\bar{z}_0^2}}\left\{1+\frac{(\bar{x}-\bar{t})}{\sqrt{(\bar{x}-\bar{t})^2+\bar{y}_0^2+\bar{z}_0^2}}+\frac{(\bar{x}-\bar{t})}{(\bar{x}-\bar{t})^2+\bar{y}_0^2+\bar{z}_0^2}\right\} \quad (3.2)$$

The thermal gradient is defined as

$$\overline{\nabla T} = \sqrt{\left(\frac{\overline{\partial T}}{\partial \bar{x}_0}\right)^2+\left(\frac{\overline{\partial T}}{\partial \bar{y}_0}\right)^2+\left(\frac{\overline{\partial T}}{\partial \bar{z}_0}\right)^2} \quad (3.3)$$

where the x, y and z derivatives are given as,

$$\frac{\partial \bar{T}}{\partial \bar{x}_0} = \frac{e^{-\left\{\bar{x}_0+\sqrt{\bar{x}_0^2+\bar{y}_0^2+\bar{z}_0^2}\right\}}}{2\sqrt{\bar{x}_0^2+\bar{y}_0^2+\bar{z}_0^2}} \left\{1+\frac{\bar{x}_0}{\left(\sqrt{\bar{x}_0^2+\bar{y}_0^2+\bar{z}_0^2}\right)}+\frac{\bar{x}_0}{\left(\bar{x}_0^2+\bar{y}_0^2+\bar{z}_0^2\right)}\right\} \tag{3.4}$$

$$\frac{\overline{\partial T}}{\overline{\partial y_0}} = \frac{\overline{y_0} e^{\left\{\overline{x_0}+\sqrt{\bar{x}_0^2+\bar{y}_0^2+\bar{z}_0^2}\right\}}}{2\left(\bar{x}_0^2+\bar{y}_0^2+\bar{z}_0^2\right)} \left\{1+\frac{1}{\sqrt{\bar{x}_0^2+\bar{y}_0^2+\bar{z}_0^2}}\right\} \tag{3.5}$$

and

$$\frac{\overline{\partial T}}{\overline{\partial z_0}} = \frac{\bar{z}_0 e^{\left\{\overline{x_0}+\sqrt{\bar{x}_0^2+\bar{y}_0^2+\bar{z}_0^2}\right\}}}{2\left(\bar{x}_0^2+\bar{y}_0^2+\bar{z}_0^2\right)} \left\{1+\frac{1}{\sqrt{\bar{x}_0^2+\bar{y}_0^2+\bar{z}_0^2}}\right\} \tag{3.6}$$

As discussed by Bontha [78], the dimensionless cooling rate and thermal gradient can be dimensionalized using

$$\frac{\overline{\partial T}}{\overline{\partial t}} = \left(\frac{2k}{\rho c V}\right)^2 \left(\frac{\pi k}{\alpha Q V}\right) \frac{\partial T}{\partial t} \tag{3.7}$$

and

$$|\overline{\nabla T}| = \left(\frac{2k}{\rho c V}\right)^2 \left(\frac{\pi k}{\alpha Q}\right) |\nabla T|. \tag{3.8}$$

3.3 Results

This section explores the behavior of the cooling rate the thermal gradient through the depth of the melt pool. These thermal conditions are plotted for low, medium and high power and velocity cases used in the single bead deposit experiments outlined in Chapter 1. In this section, blue, red and green correspond to experimental cases along the curves of constant melt pool areas 10.3mm^2 (0.016in^2), 20.6mm^2 (0.032in^2), and 41.2mm^2 (0.064in^2) respectively. The thermal

conditions through the depth of the melt pool are explored for the experimental cases of Power= 1500, 3000, and 5000 Watts on each of the predicted constant area curves. The experimental micrographs of the single bead deposits are quantified. The melt pool cross sectional area is measured and the beta grain size and morphology are measured using standard stereology procedures.

3.3.1 Effect of Bead Geometry

In the finite element models, the bead of added material is approximated as a rectangle. The actual deposited bead is a rounded shape. The difference between the thermal conditions along the solidification front of a rectangular bead finite element simulation and a simulation with no material added is shown in Figure 3.2. The cooling rate differs by almost a factor of two between the added and no added material simulations. A rounded bead would fall somewhere between these two cases. It is important to note that the cooling rates reported here are for an approximated bead shape and may differ from the actual experimental cooling rates, however, the trends are the same.

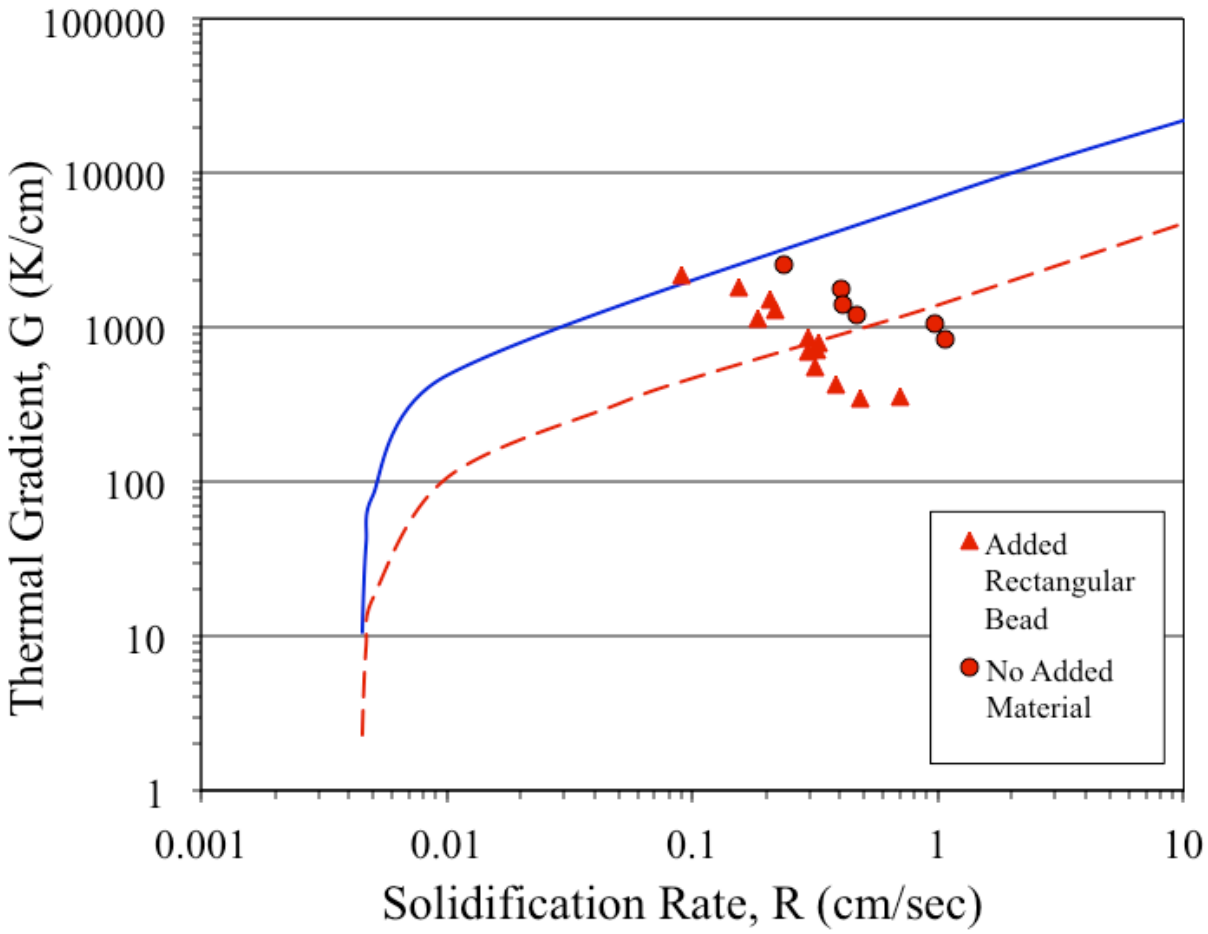

Figure 3.2: Solidification map showing effect of bead geometry

3.3.2 Cooling Rate

In chapter 2, the curves of constant cooling rate were given in P-V process space. These values are for the top of the melt pool contour only. Because the cooling rate varies through the melt pool depth, this section will explore whether the curves of constant cooling rate remain similar to the curves of constant melt pool area at other portions in the melt pool depth. The cooling rate versus the normalized melt pool depth is seen in Figure 3.3. The melt pool depth is normalized to have a maximum depth of 1, for comparison of melt pools with different depths.

The cooling rate decreases through the melt pool depth and will theoretically reach zero for an instant at the very bottom when the transition from melting on the leading edge of the melt pool to solidification on the trailing edge of the melt pool occurs. However, the cooling rate remains relatively constant through the melt pool depth, and does not begin to decrease until after half way through the depth of the melt pool. The behavior of the cooling rate through the depth of the melt pool is similar for cases with different powers when the cross sectional area is the same. Though the lines group by area, in the 1500W cases for all areas the cooling rate is lower than the higher power cases seen in Figure 3.3. At lower powers the curves of constant area are no longer the curves of constant grain size. The average grains size is expected to increase as the power is decreased to 1500 W and below for cases with a constant area melt pool area. The higher power cases on the blue line switch positions because different fitting parameters were used in the low and high velocity cases when planning the experiments.

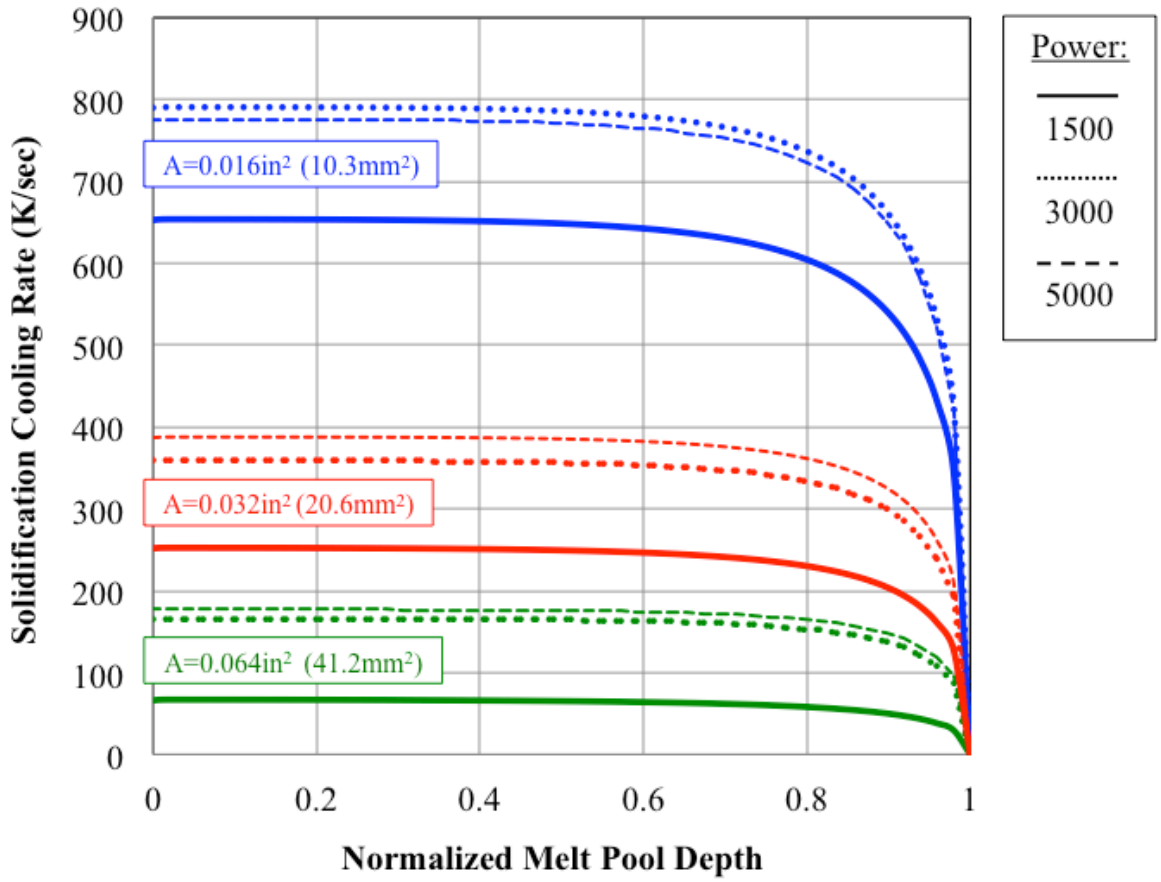

Figure 3.3: Cooling rate versus melt pool depth

3.3.3 Thermal Gradient

The thermal gradient is a dominating factor in determining the beta grain morphology. In Chapter 2, the grain morphology boundaries were given for the point of lowest thermal gradient where the grain morphologies take place. However, the thermal gradient spans a large range through the depth of the melt pool. An inconsistent microstructure is produced when both columnar and equiaxed microstructures are present through a single melt pool depth.

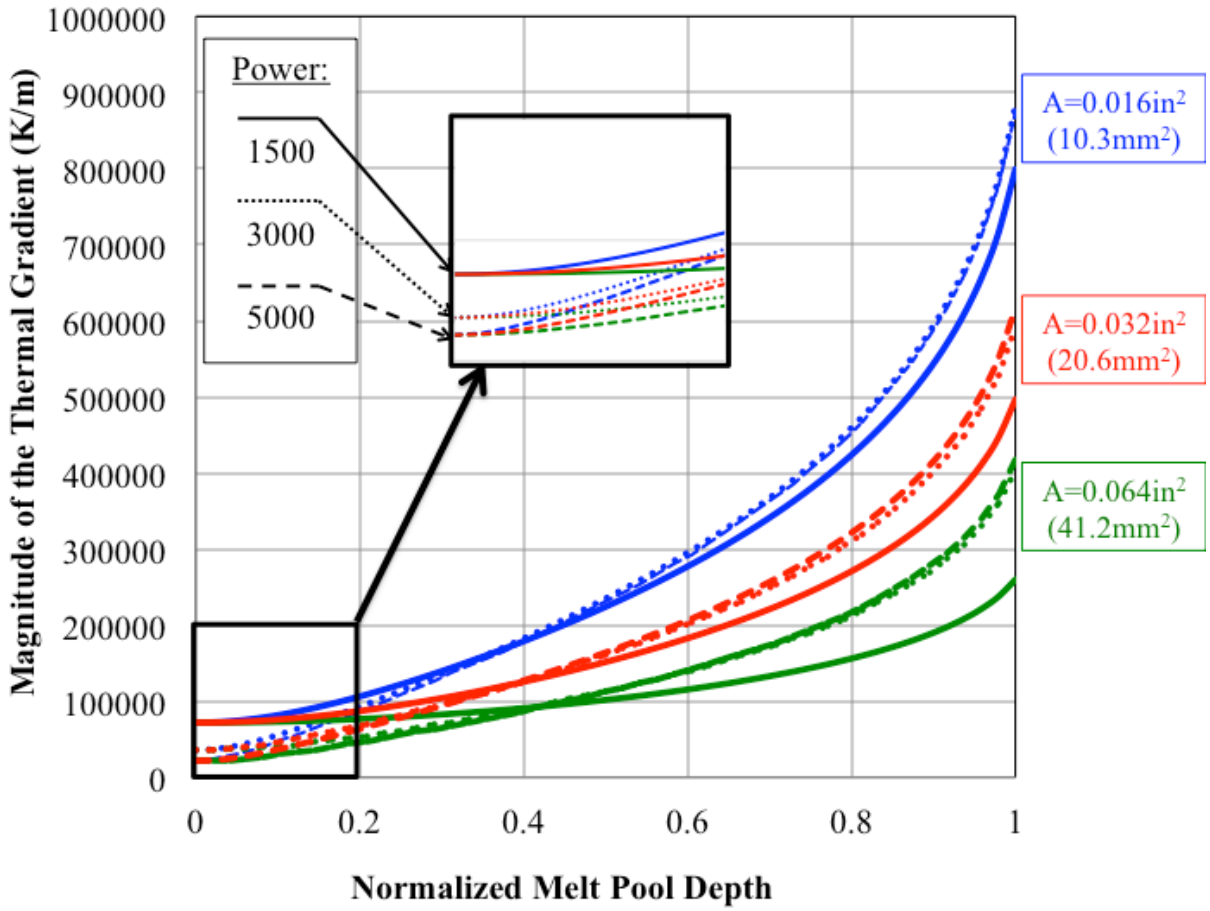

Figure 3.4: Magnitude of the thermal gradient through the melt pool depth

In Figure 3.4, the magnitude of the thermal gradient is plotted through the melt pool depth using the fitted analytical approximation. At the top of the melt pool (normalized depth=0) the thermal gradient is grouped by beam power. For example, all of the 1500W cases have the same thermal gradient value at that point. At the bottom of the melt pool (normalized depth=1), the thermal gradient groups by melt pool area (green, red and blue).

To investigate the behavior of the magnitude of the thermal gradient, the thermal gradient is split into its individual components. Directions are taken to be consistent with those used for the Rosenthal solution. Results are investigated along the plane of y=0, with y being the direction

perpendicular to the travel direction on the top surface. The thermal gradient in the y-direction on this plane is zero. The z-direction is perpendicular to the travel direction through the melt pool depth. The x-direction is parallel to the travel direction.

The curves of thermal gradient in the x-direction group by beam power, as seen in Figure 3.5. The curves are fairly constant through the depth until the curves approach the maximum depth (normalized depth =1), where the x-gradient goes to zero. As seen in Figure 3.6, the thermal gradient in the z-direction is zero at the top of the melt pool contour and rapidly increases through the depth. At the top of the melt pool contour, the x-gradient is the dominating portion of the magnitude, therefore the magnitude groups by power at this point. Because the z-component of the gradient is so much larger than the x-component, the z-component quickly begins to dominate and the overall solidification is directional in the z-direction.

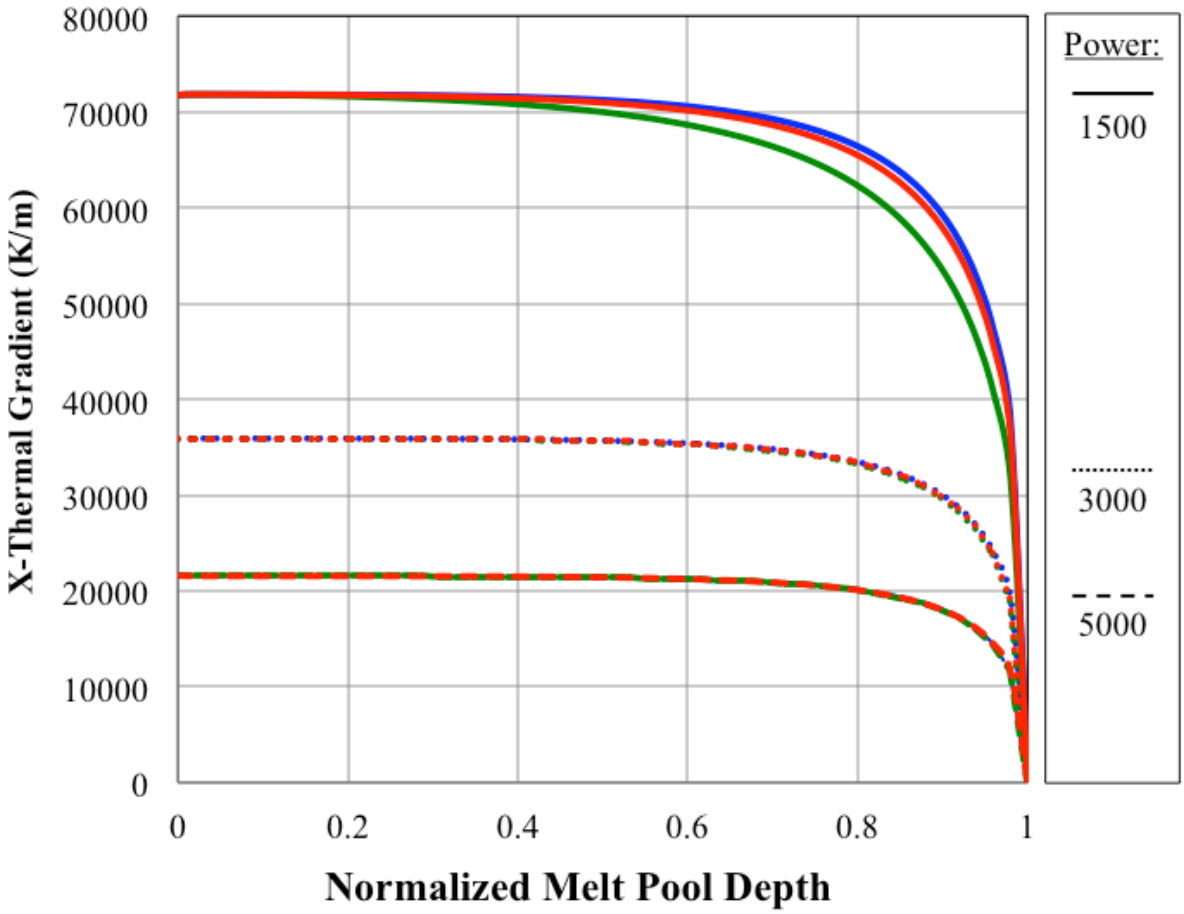

Figure 3.5: Thermal gradient in the x-direction through the melt pool depth

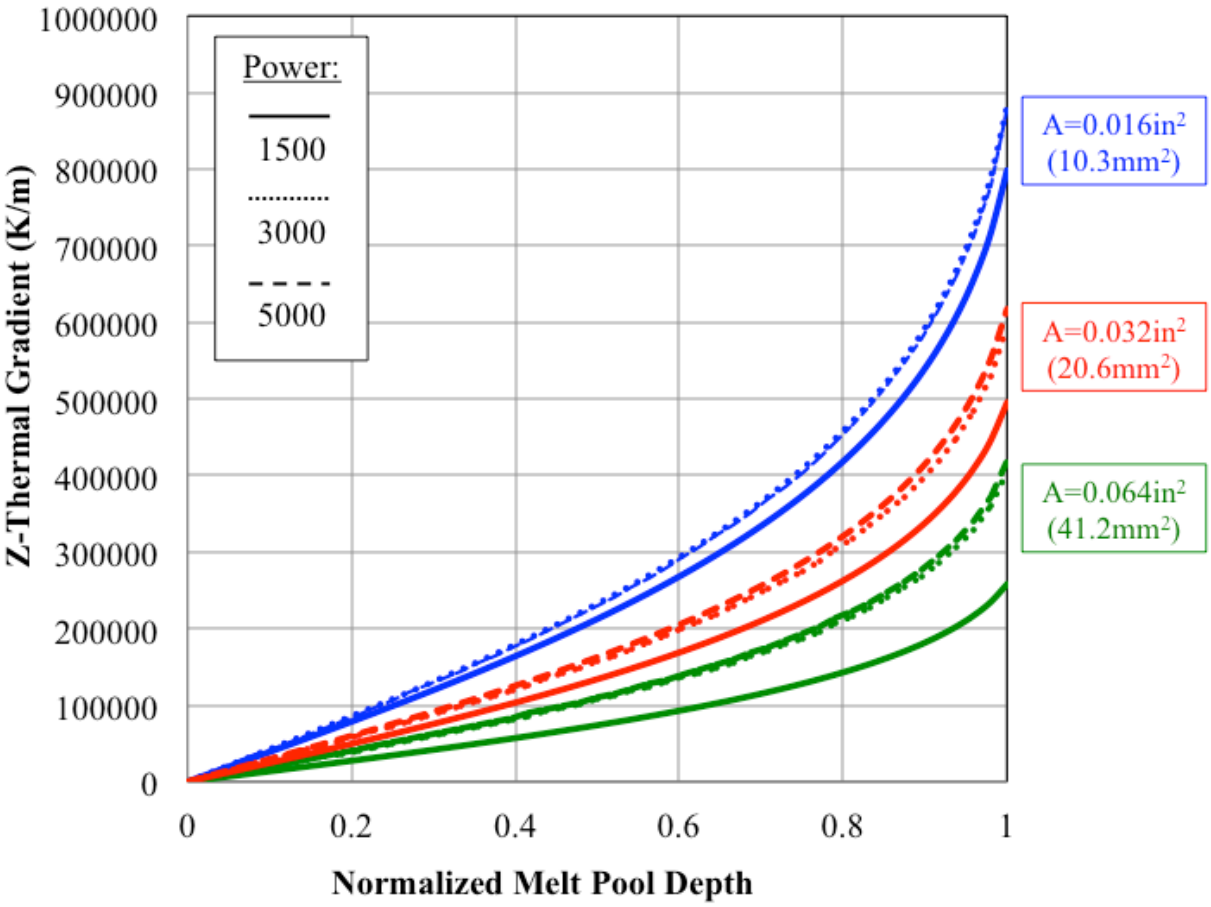

Figure 3.6: Thermal gradient in the z-direction through the melt pool depth

3.3.3.1 Effect on Grain Morphology

Due to the large variation in thermal gradient through the depth of the melt pool, one melt pool cross section can span both the columnar and equiaxed regions. In Chapter 2 the grain morphology region boundaries are presented for the top of the melt pool where the transition to equiaxed morphology will first take place. Figure 3.7 presents the mixed to equiaxed grain morpholology boundary, from the solidification map of Figure 1.1, for different percentages of depth through the melt pool where Top represents the 0% boundary. Within the range for the electron beam wire feed process, it is not possible to obtain more than 30% equiaxed grains in the melt pool cross section. The 40% equiaxed grains curve is outside the electron beam wire feed processing space. This plot suggests that, in general, increasing the power will increase the amount of equiaxed grains in a melt pool. However, only equiaxed grains cannot be obtained. This means that in order to obtain a consistent microstructure (not a mix of columnar and equiaxed), the processing variables must be in the columnar region.

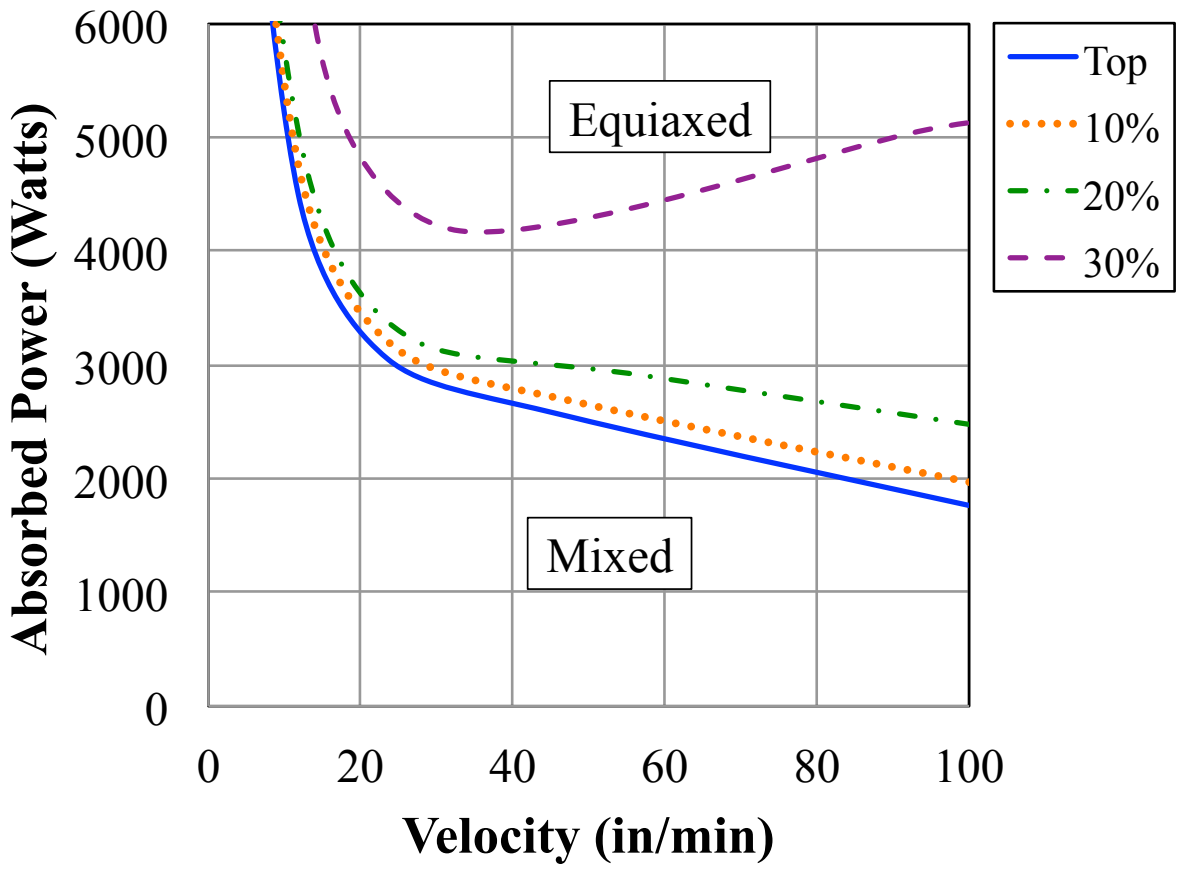

Figure 3.7: Equiaxed morphology boundaries through the melt pool depth

3.4 Chapter Summary

In this chapter, the thermal conditions at the onset of solidification for cases of constant melt pool area are investigated through the depth of the melt pool. The cooling rate remains relatively constant through the melt pool depth, with a decrease in cooling rate at the bottom of the melted region. Also, for cases of constant melt pool area, the cooling rate (grain size) remains constant for the medium and high power cases. For the low power cases, the cooling rate

decreases. If the melt pool area is held constant, the grain size will remain constant until the power is decreased to ~1500W and below.

The magnitude of the thermal gradient groups by power at the top of the melt pool contour, because the gradient in the x-direction is dominating and the z-gradient is zero. The z-gradient quickly increases and begins to dominate as the depth increases. At the bottom of the melt pool, the magnitude of the gradient groups by melt pool area. Because the z-gradient is much larger than the x-gradient, there is directional solidification in the z-direction. The large span of thermal gradient values result in multiple grain morphologies within a single melt pool cross-section. Within the electron beam wire feed range, up to around 30% of the melt pool will have equiaxed morphology and the rest is columnar. This inconsistency in microstructure can make design difficult due to inconsistency determining mechanical properties.

Chapter 4 Process Mapping of Solidification Microstructure for Deposition of a Thin Wall in Electron Beam Wire Feed Systems

4.1 Chapter Overview

Depositing of an entire part can be broken down into a combination of different geometries. The previous chapters show that indirect microstructure (prior beta grain size and morphology) control is possible through direct melt pool dimension control in single bead deposits of Ti-6Al-4V. In this topic, the connection between microstructure and melt pool dimensions is explored for the deposition of a tall thin wall.

This chapter focuses on a tall, thin wall where steady state conditions are reached and the substrate material has no effect on the thermal conditions. Finite element modeling and a 2D analytical approximation is used to create the process map for controlling solidification microstructure in tall thin wall deposits. The solidification microstructure process map is then compared to the process map for controlling melt pool dimensions. Comparison of the two process maps shows that integrated control of solidification microstructure and melt pool dimensions can be extended to thin wall geometries. By controlling melt pool area, a constant grain size is also maintained. Select experiments are presented in order to assess the numerical predictions.

4.2 Methods

4.2.1 Finite Element Model

The deposition of a tall, thin wall is modeled using 2D finite element simulations, performed in the commercial program ABAQUS. Because the deposition takes place in a vacuum, the model does not include convective heat transfer. The nodes have an initial temperature and a constant temperature specified at the base of T_0=293 K to simulate the ambient temperatures in deposition experiments. A distributed heat flux is applied to the side of each element traveling across the top of the model to simulate the velocity of the beam. Four node, linear heat transfer elements are used throughout the model and temperature dependent material properties and latent heat are included. In order to reduce computation time, the model is biased to the region where the heat flux is applied. The model also does not model the addition of new material with beam travel (which also reduces computational time) but the effects of added material on the thermal problem are expected to be very small for this geometry. The 2D mesh can be seen in Figure 4.1. The melt pool area is determined by multiplying the wall thickness *t* by the maximum depth *d* with t/d=1.95 in each of the models (also consistent with experimental observations). The cooling rate and thermal gradient are extracted along the solidification front using the same method as outlined in Chapter 2. Temperature-dependent thermal properties and latent heat are included in the model.

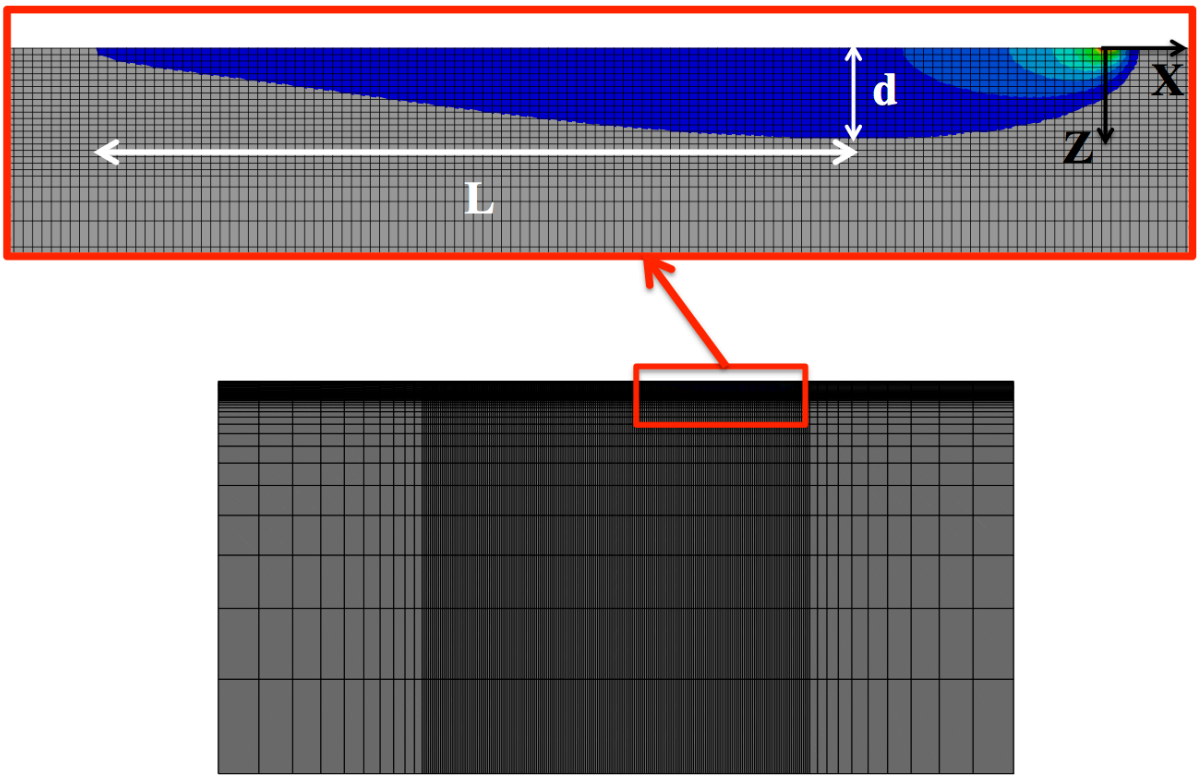

Figure 4.1: 2D finite element mesh

4.2.2 Analytical Approximation

The 2D Rosenthal closed form solution is used to guide the finite element modeling. The Rosenthal solution gives the temperature field around a moving point heat source. The finite element models are used to fit the constant material properties of the Rosenthal solution, using the same procedure as in Chapter 3, to accurately predict the desired quantity, which in this case is the solidification microstructure. The Rosenthal solution assumes a point heat source, with no

material added, constant material properties and no latent heat. This study considers the 2D thin wall geometry of Figure 4.2, in which the process variables of interest are the absorbed beam power αQ and velocity V. It is assumed that the height h and length L are sufficiently large such that the steady-state Rosenthal solution for a moving point source of heat applies.

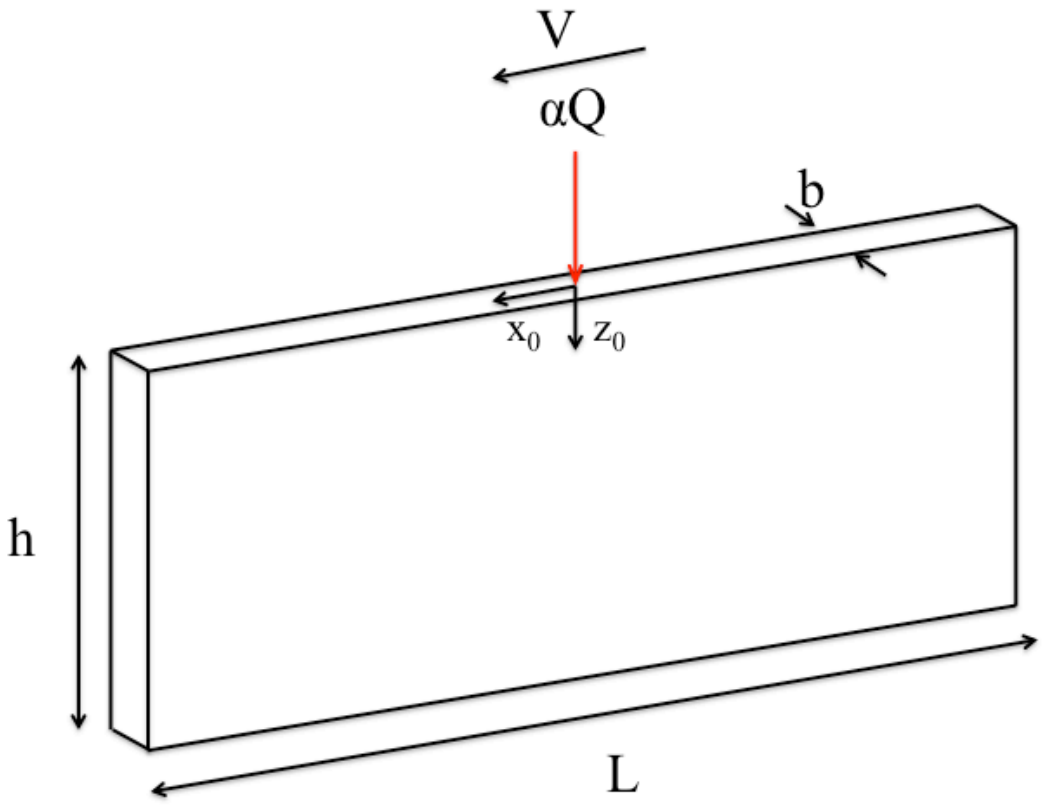

Figure 4.2: 2D Rosenthal geometry

Relative to the position of the point heat source, the nondimensional temperature field is given by Vasinonta et al. [71] as,

$$\bar{T} = e^{-\bar{x}_0} K_0 \left(\sqrt{\bar{x}_0^2 + \bar{z}_0^2} \right). \tag{4.1}$$

The dimensionless variables of the temperature equation are defined in terms of the process parameters and thermal properties as,

$$\bar{x}_0 = \frac{x_0}{2k/\rho cV}, \bar{z}_0 = \frac{z_0}{2k/\rho cV}, and\ \bar{T} = \frac{T-T_0}{\alpha Q/\pi kb}.$$

In the above normalizations, T is the temperature at a location (x_0, z_0) relative to the moving point heat source and T_0 is the initial temperature of the wall. The relative coordinates (x_0, z_0) are related to fixed spatial coordinates (x, z) at any time t as (x_0, z_0) =(x-Vt,z), where V is the velocity of the beam. The thermal properties ρ, c and k are the density, specific heat and thermal conductivity of the material respectively, which are assumed to be temperature-independent. αQ is the absorbed power of the heat source.

The solidification microstructure of deposited metals depends on cooling rates and thermal gradients at the onset of solidification on the trailing edge of the melt pool. The trailing edge of the melt pool is where solidification occurs. In the Rosenthal solution, T_m is set equal to the melting temperature of the material and non-dimensionalized as

$$\bar{T}_m = \frac{T_m - T_0}{\frac{\alpha Q}{\pi kb}}.$$

Expressions for the dimensionless cooling rate and thermal gradient can be obtained by analytical differentiation of equation 1. The cooling rate is given as,

$$\frac{\partial \bar{T}}{\partial \bar{t}} = -e^{-(\bar{x}-\bar{t})}\left\{\frac{(\bar{x}-\bar{t})}{\sqrt{(\bar{x}-\bar{t})^2+\bar{z}_0^2}}K_1\left(\sqrt{(\bar{x}-\bar{t})^2+\bar{z}_0^2}\right)+K_0\left(\sqrt{(\bar{x}-\bar{t})^2+\bar{z}_0^2}\right)\right\}. \quad (4.2)$$

The thermal gradient is defined as

$$\left|\nabla \overline{T}\right| = \sqrt{\left(\frac{\partial \overline{T}}{\partial \overline{x}_0}\right)^2 + \left(\frac{\partial \overline{T}}{\partial \overline{z}_0}\right)^2} \tag{4.3}$$

where the x and z derivatives are

$$\frac{\partial \overline{T}}{\partial \overline{x}_0} = -e^{-\overline{x}_0}\left\{\frac{\overline{x}_0}{\sqrt{\overline{x}_0^2 + \overline{z}_0^2}} K_1(\sqrt{\overline{x}_0^2 + \overline{z}_0^2}) + K_0(\sqrt{\overline{x}_0^2 + \overline{z}_0^2})\right\} \tag{4.4}$$

and

$$\frac{\partial \overline{T}}{\partial \overline{z}_0} = -e^{-x_0}\left\{\frac{\overline{z}_0}{\sqrt{\overline{x}_0^2 + \overline{z}_0^2}} K_1(\sqrt{\overline{x}_0^2 + \overline{z}_0^2})\right\}. \tag{4.5}$$

As discussed by Bontha [78], the dimensionless cooling rate and thermal gradient can be dimensionalized using

$$\frac{\overline{\partial T}}{\overline{\partial t}} = \left(\frac{2\pi k^2 b}{\alpha Q \rho c V^2}\right)\frac{\partial T}{\partial t} \tag{4.6}$$

and

$$\left|\overline{\nabla T}\right| = \left(\frac{2\pi k^2 b}{\alpha Q \rho c V}\right)\left|\nabla T\right|. \tag{4.7}$$

4.2.3 Thin Wall Experiments

Tall thin wall deposit experiments were performed at NASA Langley Research Center in order to assess the numerical predictions. The NASA EBF^3 system is an electron beam system with a wire feed. The experiments performed were deposition of Ti-6Al-4V onto the side of a substrate plate of the same material, representing a tall thin wall, using various beam powers and

velocities. A schematic of the experiment set up can be seen in Figure 4.3. Four Ti-6Al-4V plates are clamped together with a clamp on either end with aluminum spacers in between the Ti-6Al-4V plates. A plate of aluminum is mounted under the samples in order to protect the build plate in case the work piece shifts. Toe clamps that are mounted to the table are used in order to hold the assembly to the table so the work piece does not move.

The origin is specified at the bottom left corner of the first experiment plate. The distance of each power and velocity combination is at least 3 melt pool lengths, in order to ensure that a steady state has been reached. Each bead has one inch on the edge of the plate in order to eliminate the effect of the edges. Process variables were chosen for cases with the same predicted melt pool area. Due to limited availability of plate thicknesses, a standard plate thickness of 0.25" is chosen for an area of 20.6mm^2 (0.032in^2). This is the area that is referred to as the red area in the single bead analysis. Samples are sectioned using a water jet cutter and are seen in Figure 4.5.

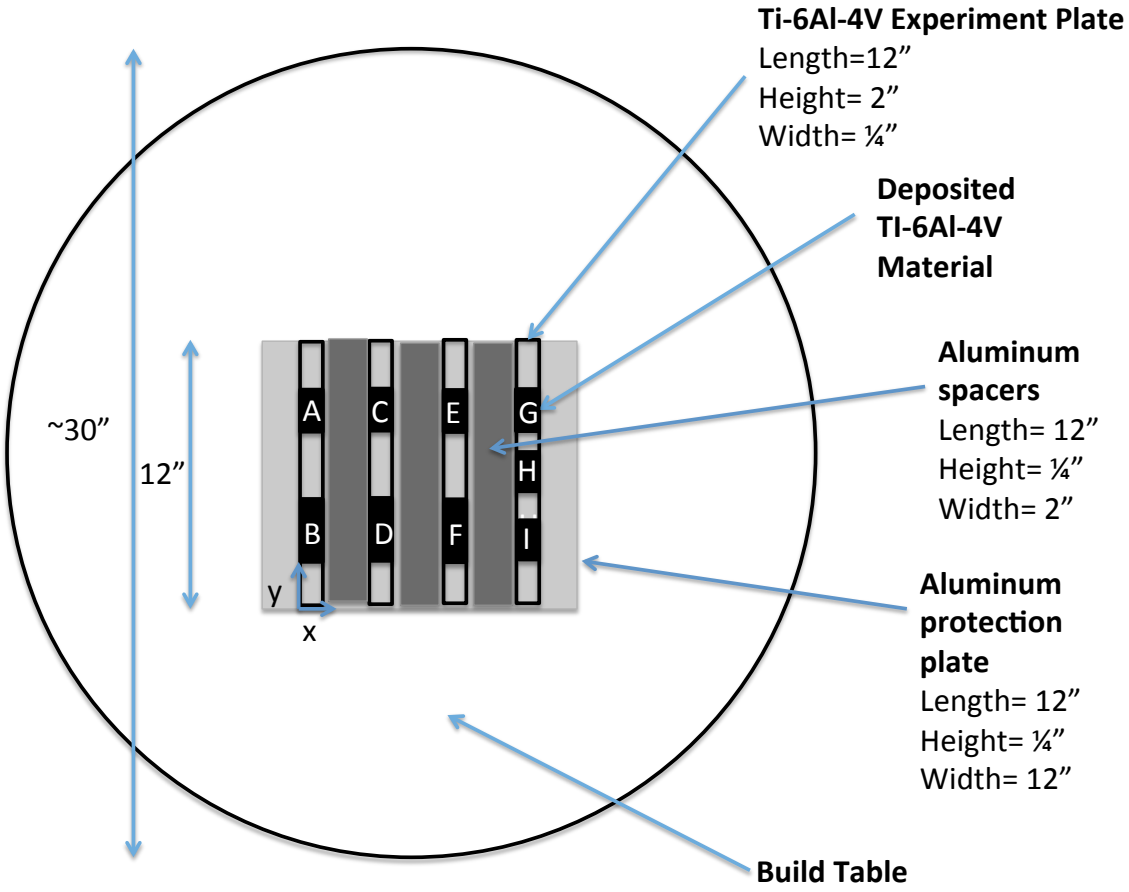

Figure 4.3: Experimental set-up schematic

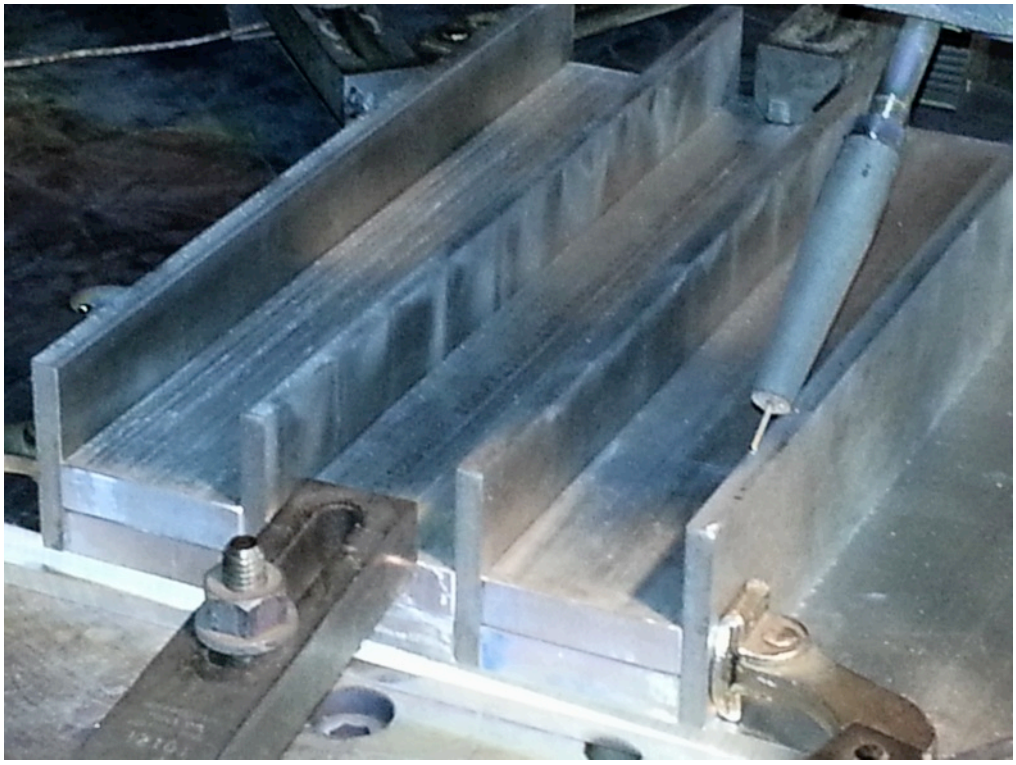

Figure 4.4: Experimental set-up

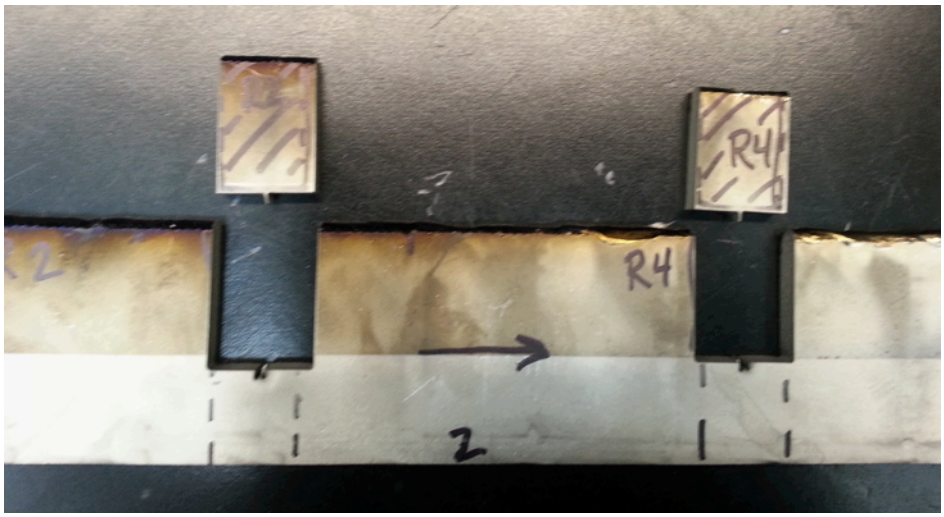

Figure 4.5: Sectioning of experiments

Name	Absorbed Power (W)	Source Power (W)	Velocity (in/min)	Wire Feed Rate (in/min)	Wire Diameter (in)
Wall 1					
R1	1000	1111	8.8	51.8	0.063
R5	5000	5556	52.7	310.3	0.063
Wall 2					
R2	2000	2222	20.0	117.8	0.063
R4	4000	4444	41.9	246.7	0.063
Wall 3					
R3	3000	3333	31.0	182.6	0.063

Table 4.1: Thin wall experiment processing parameters

Name	Bead Length for steady state (in)	Sample Position	Bead Start Coordinates	Bead End Coordinates
Wall 1				
R1	2	B	(0.125, 1)	(0.125, 3)
R5	7	A	(0.125, 4)	(0.125, 11)
Wall 2				
R2	3	D	(2.375, 1)	(2.375, 4)
R4	6	C	(2.375, 5)	(2.375, 11)
Wall 3				
R3	5	F	(4.625, 1)	(4.625, 6)

Table 4.2: Thin wall experiment locations

Sectioned specimens were mounted in resin using 1.5” diameter molds, polished and etched in order to observe the solidification microstructure. The samples were polished using the procedure outlined in Appendix A. The mounted and polished samples can be seen in Figure 4.6.

Figure 4.6: Mounted, polished and etched thin wall samples

4.3 Results

4.3.1 Solidification Microstructure Process Map for Thin Wall Geometries

A P-V process map for solidification microstructure in thin wall deposits is created in order to identify paths or regions of processing space with constant grain size and different grain morphologies. The paths of constant cooling rate are identified using 2D finite element simulations. The curves of cooling rate represent different cooling rate, with successive doubling of the cooling rate with the lowest being on the left side. The morphology data from the G vs. R plot of the solidification map for Ti-6Al-4V in Figure 1.1 [9] is translated onto a plot of power versus velocity in using the fitted analytical approximation seen in Figure 4.7. The results presented here are for the top of the melt pool, which is a critical location, where the lowest gradients are present and the transition to a mixed or equiaxed grain morphology will first take place. Results indicate that all cases for the thin wall deposits will have some equiaxed grains.

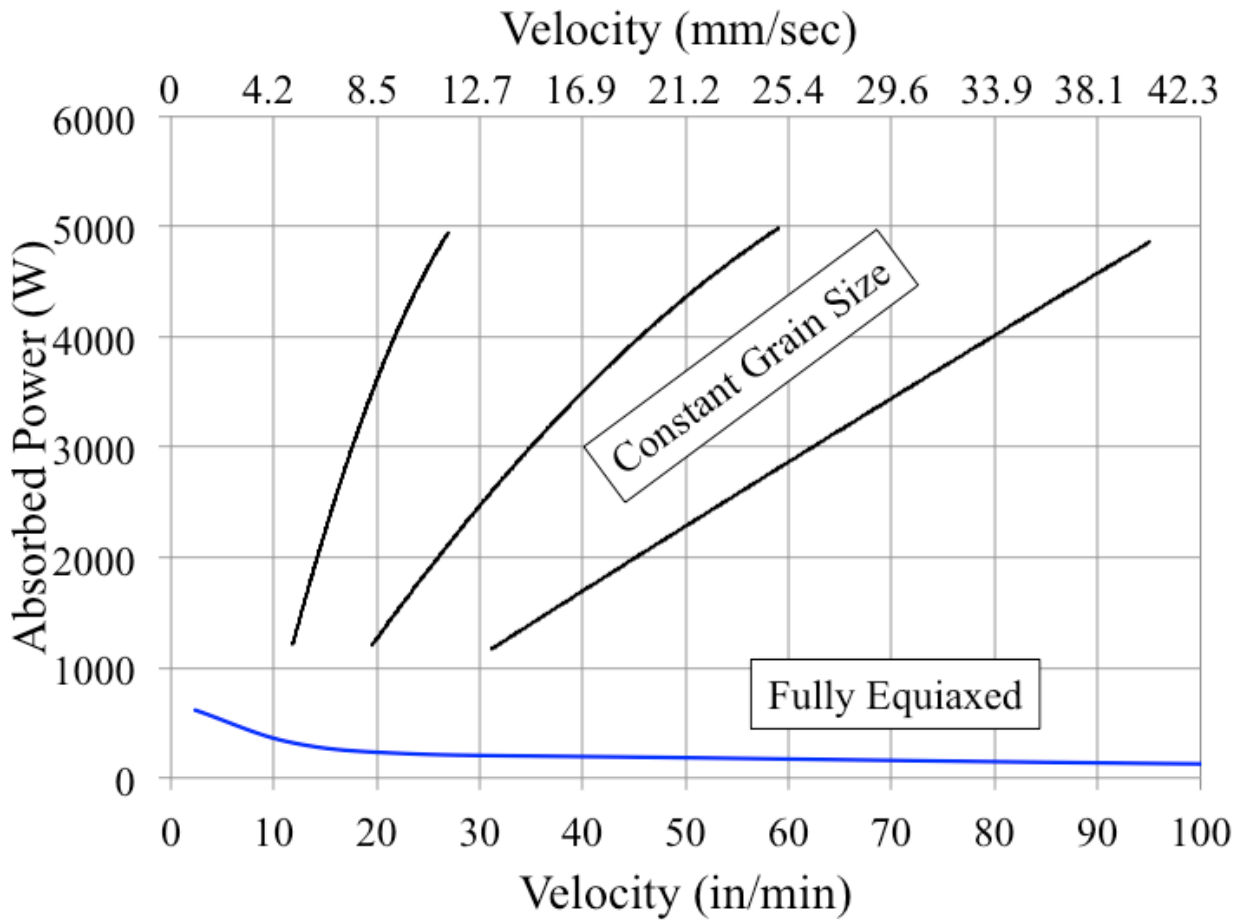

Figure 4.7: Solidification microstructure process map for deposition of thin wall geometries of Ti-6Al-4V

The resulting P-V process map for controlling solidification microstructure for thin wall deposits of Ti-6Al-4V in an electron beam wire feed process shown in Figure 4.7 (for $T_0 = 298$ K and wall thickness/depth= 1.95). The solid black lines in Figure 4.7 are curves of constant cooling rate, which are nearly linear in P-V space. It is possible to maintain a constant grain size while moving from low powers and low velocities, to high powers and high velocities, if the identified path is followed. The boundary between mixed and fully equiaxed grain morphology is the curved solid line. This curves defines the boundary of the regions where mixed and equiaxed

grain morphologies exist. The boundary between the columnar and mixed regions is not shown because it is below the mixed to equiaxed boundary and is outside the parameters for this process.

4.3.1.1 Integrated Control of Solidification Microstructure and Melt Pool Dimensions

Resent results by Fox [94], creates the process map for controlling melt pool area in thin wall deposits in the electron beam wire feed additive manufacturing processes. The process map for melt pool dimension control is shown in Figure 4.8 [94]. This map is for the geometry of a tall thin wall, with T_0 = 298K and a ratio of wall thickness to depth=1.95. Curves of constant melt pool cross sectional area (a melt pool size metric) as well as curves of constant melt pool length to depth ratio (a melt pool shape metric) are plotted in P-V space. The thin wall area is calculated as a rectangle by multiplying the maximum depth by the wall width by the specified melt pool width for cases when the ratio of t/d=1.95 is obtained. The length is the distance behind the maximum melt pool depth to the end of the melted region. By following curves of constant area or L/d, this P-V process map for melt pool dimension control allows these quantities to be maintained across P and V values differing by as much as a factor of 5.

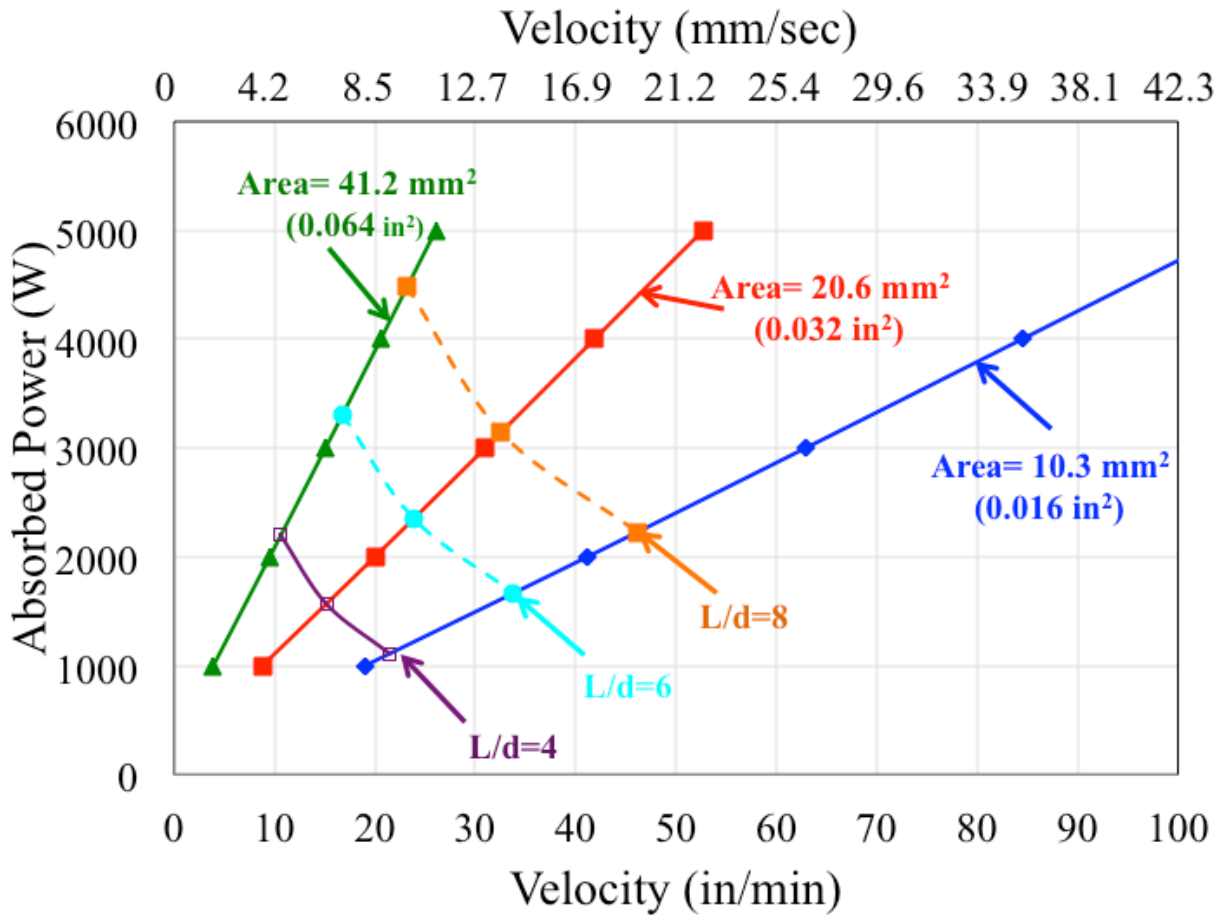

Figure 4.8: Melt pool dimensions process map for thin wall deposits

When comparing the thin wall process map for solidification microstructure in Figure 4.7 to the process map for melt pool dimensions in Figure 4.8, connections can be drawn between the two process maps similar to those seen for the single bead deposits. The curves of constant grain size are similar to the curves of constant melt pool cross sectional area, A. In other words, by controlling A (which can be related to melt pool width, which is observable in real time during processing), a constant beta grain size is also maintained. The relationship seems to deviate at the lower powers. At the lowest power, the area corresponding the constant cooling

rate is approximately double that of the higher power. The grain morphology region boundary is below the process variables investigated, so it cannot be compared to the melt pool metrics.

Integration of the solidification microstructure and melt pool dimension process maps allows the ability to indirectly plan and control solidification microstructure by controlling melt pool size and shape in real time. Results show that this can be accomplished for both thin walls and single bead deposits.

4.3.2 Experimental Results

Thin wall deposits experiments with P-V combinations along the red line of constant area were performed in order to investigate the grain size and melt pool area relationship. Micrographs of the polished and etched thin wall samples are seen in Figure 4.9. The experiment performed for P=1000 W did not turn out well. The wire being fed into the melt pool was walking from side to side and there are portions of unmelted wire next to the bead seen in Figure 4.10. Following the recommendation of researchers at NASA Langley, an additional test was performed reducing the wire feed rate by 20% and that bead is seen in Figure 4.11. The quality of the bead is improved, and all wire is melted. This indicates that at low powers the melted material to added material ratio needs to be adjusted. Depositing the material directly on the center of the thin wall is a challenge. It is evident in the micrographs that the heat was not applied directly to the middle of the wall because the melt pools are not symmetric. Seen in Figure 4.9 (c), this case is very off center.

The numerical predictions show that significant equiaxed grains should be present within the melt pool. Qualitatively, it can be seen that there are equiaxed grains present in all melt pools.

There does not seem to any correlation with increased presence of equiaxed grains with an increase in power, as was seen in the single bead deposits. There are two experimental cases with significant columnar grains seen in Figure 4.9 (a) and (c), which is likely due the experimental errors of unmelted wire and depositing off center. Results indicate that a fully equiaxed grain structure can be obtained in deposition of a tall thin wall.

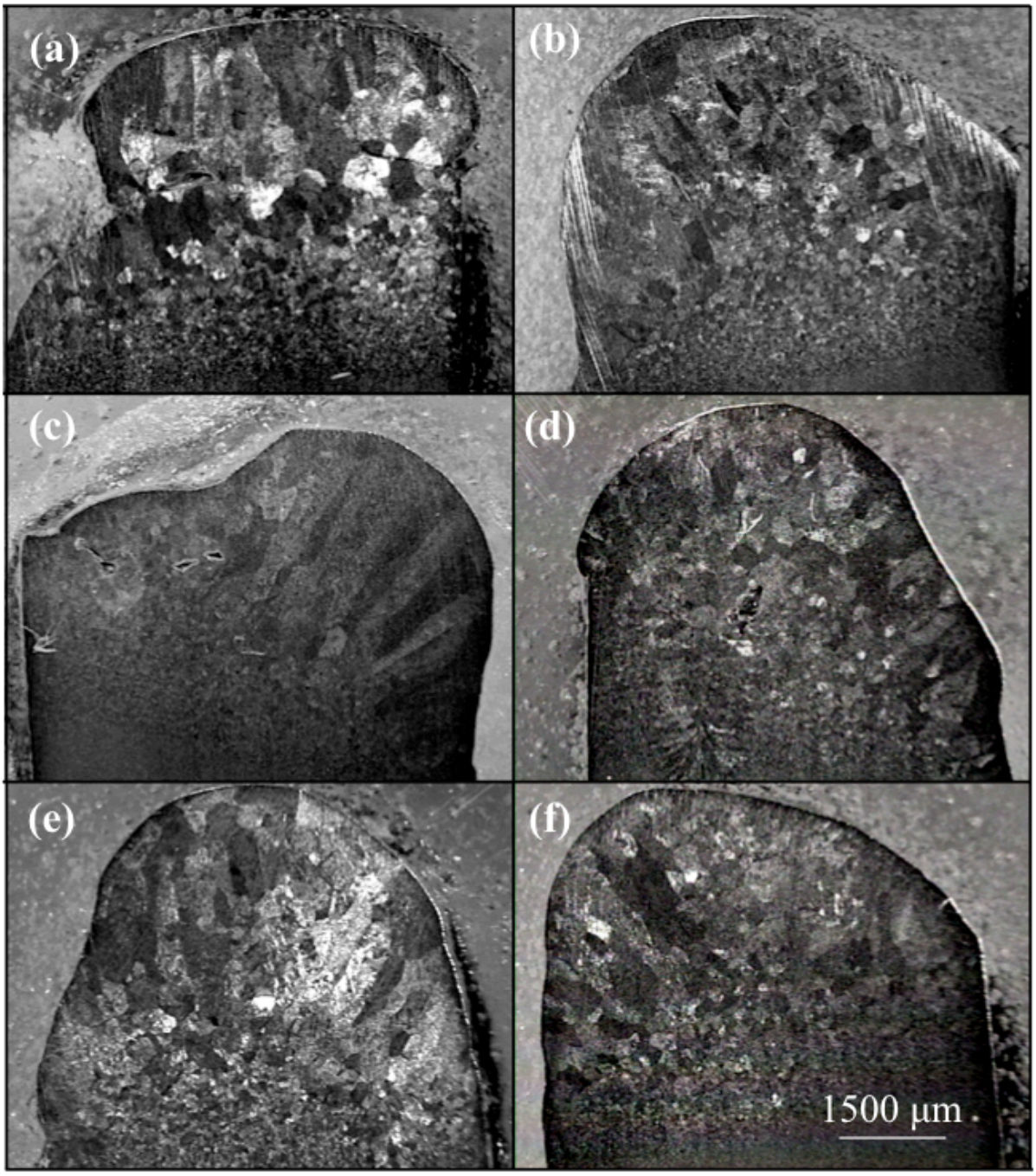

Figure 4.9: Thin wall experiment micrographs for P (W) ,V (in/min) combinations: (a) 1000, 8.8, (b) 2000, 20, (c) 3000, 31, (d) 4000, 41.9, (e) 5000, 104.9 and (f) 1000, 8.8 with a reduced wire feed rate

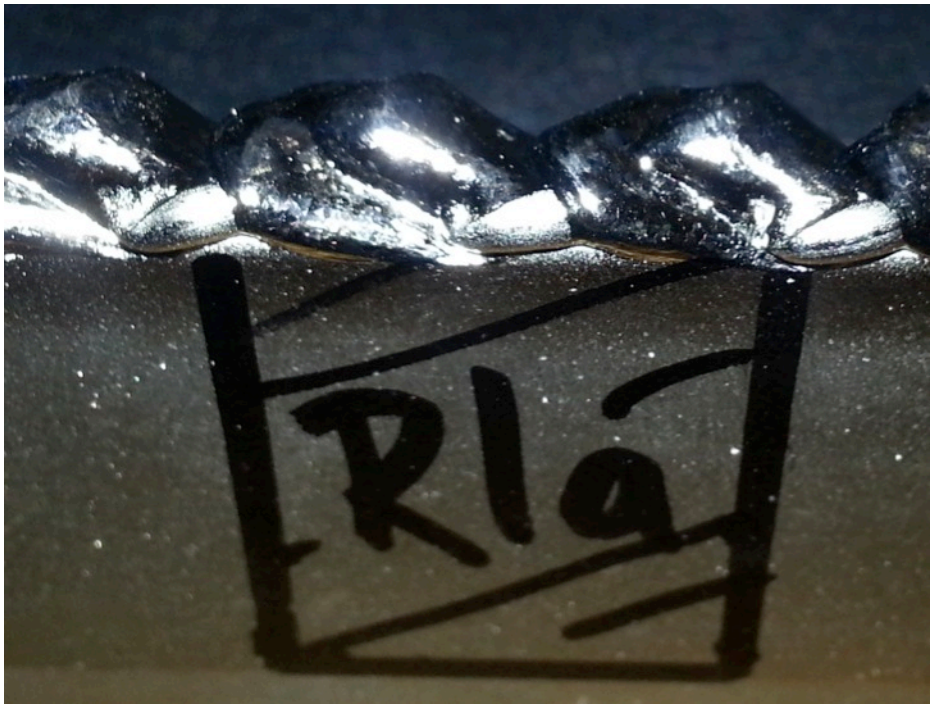

Figure 4.10: Thin wall P=1000 W original experimental bead

Figure 4.11: Thin wall P=1000 W reduced wire feed rate experimental bead

The melt pool area was measured using the same procedure as in Chapter 3, and the measurements are shown in Figure 4.12. The predicted melt pool area is 0.032 in^2. The measured melt pool area is relatively constant, and is close to the predicted value. There seems to be a trend of increasing area with increasing power, however additional experiments are needed to confirm a correlation.

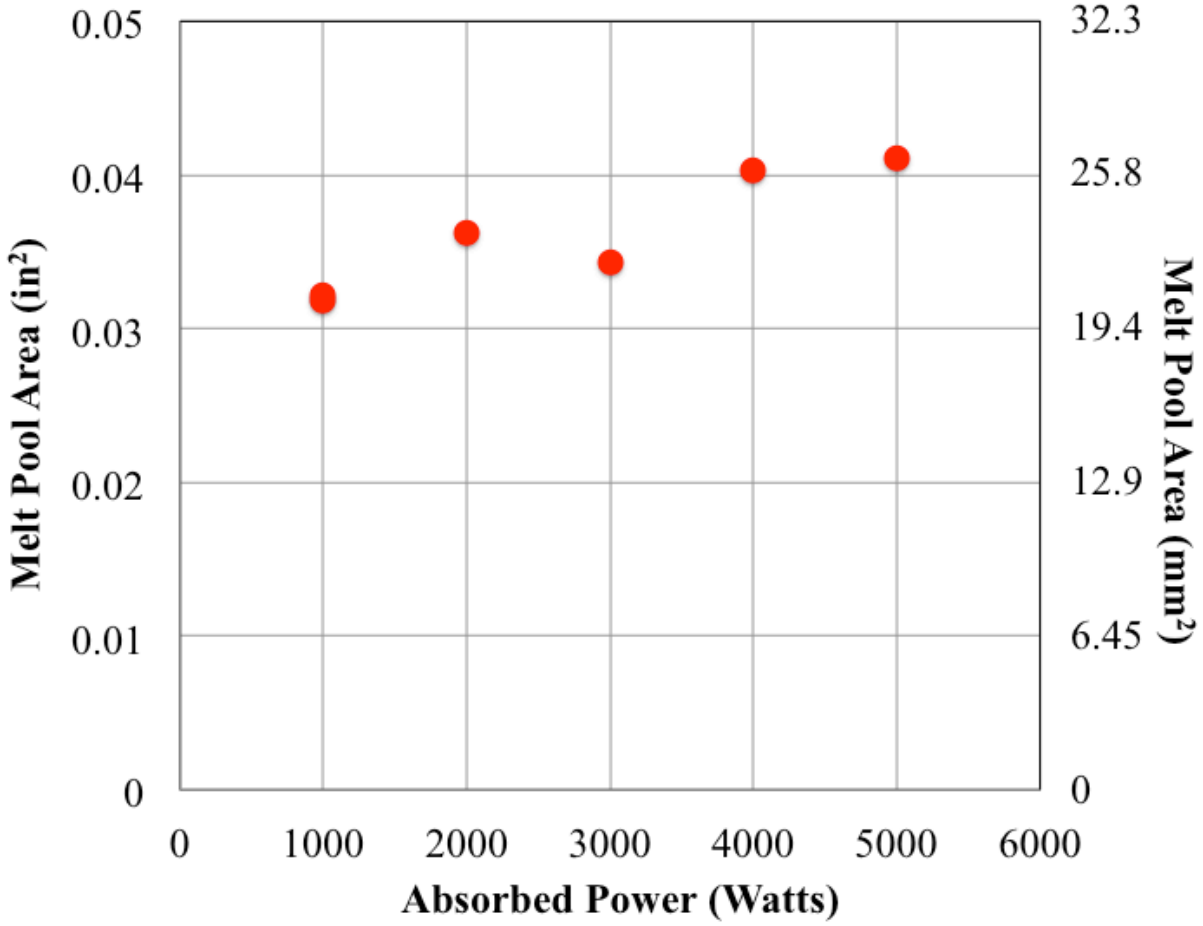

Figure 4.12: Thin wall experimental melt pool area

The beta grain widths are measured using the intercept method, which is the method used in Chapter 2. The grain size remains relatively constant for all experimental cases. This result shows that by maintaining a constant melt pool area, a constant grain size can be achieved.

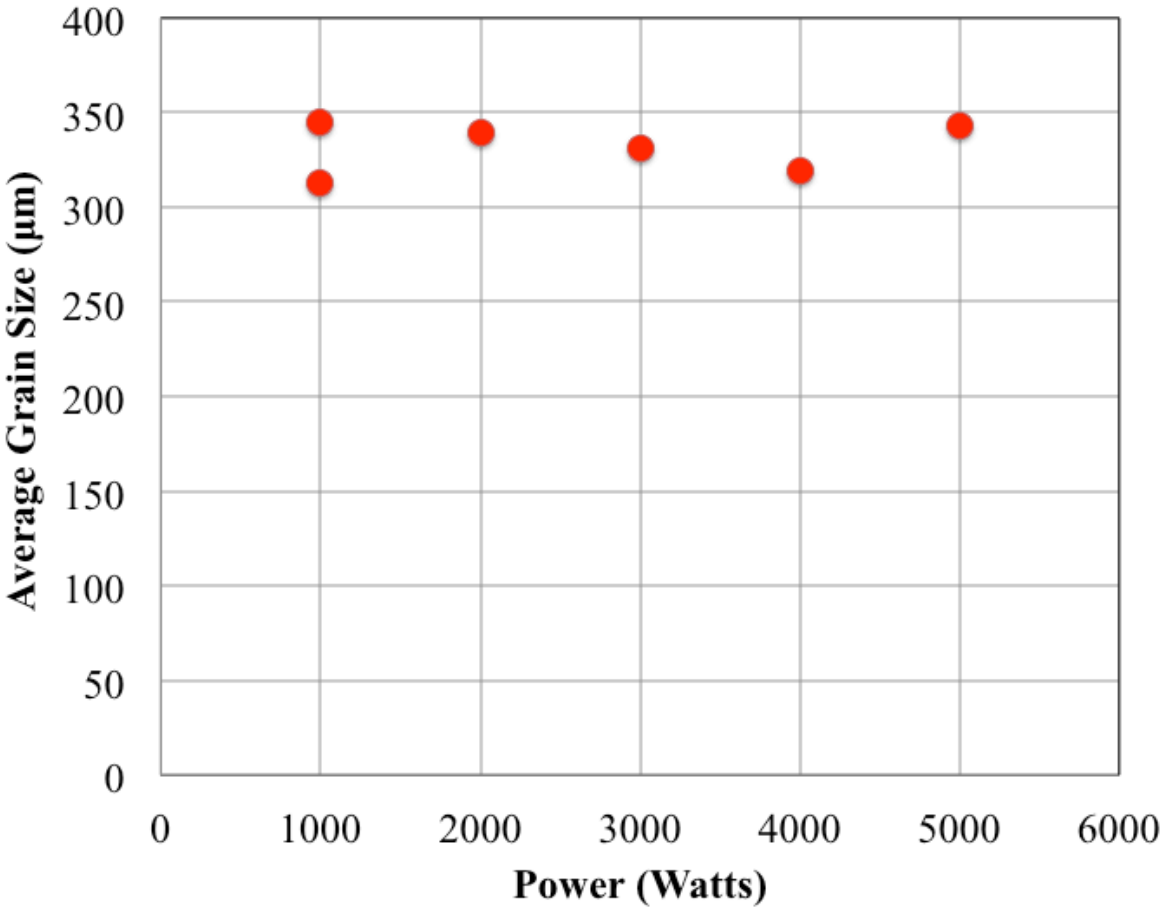

Figure 4.13: Thin wall experimental beta grain width measurements

4.4 Discussion: Single Bead and Thin Wall Integrated Control of Solidification Microstructure and Melt Pool Dimensions

In Chapter 2 it was shown that for single bead deposits onto large substrates Ti-6Al-4V beta grain width scales with the melt pool width. Figure 4.14 combines results from Chapter 2 (single beads) with those from this chapter (thin walls), plotting average beta grain width versus the effective melt pool width. Note that the effective melt pool widths are calculated differently for thin walls and single beads as outlined in their respective sections. This result shows that by maintaining a constant melt pool width, a constant grain size can be achieved for both single beads and thin walls with a scaling factor of ~20 grains per melt pool width.

These findings have significant implications for AM process control, where imaging from above of maximum melt pool widths can be part of a real-time control system. What this research has shown is that such a system can be used not only as a means for direct control of melt pool size, but also as a means for indirect real-time control of beta grain widths. Beta grain widths have been shown to be approximately $1/20^{th}$ of maximum melt pool widths across two geometries. Also, those two geometries represent extreme cases for constraint on conduction into the substrate (single beads are least constrained, single pass thin walls are most constrained). This suggests the possibility of a geometry-independent relationship between maximum melt pool width and beta grain width for this process.

This result and the earlier results for melt pool geometry also suggest an overall strategy for controlling both melt pool geometry and beta grain width across geometries. In transitioning between geometries, beam powers and travel speeds must be adjusted to maintain a constant melt pool size (maximum cross-sectional area or width) and shape (L/d). P-V process maps for these

quantities for each geometry can be used to determine the adjustments needed and changing both P and V allows for both melt pool size and melt pool shape to be controlled. However, once melt pool size is controlled, beta grain size is also controlled due to links between the two.

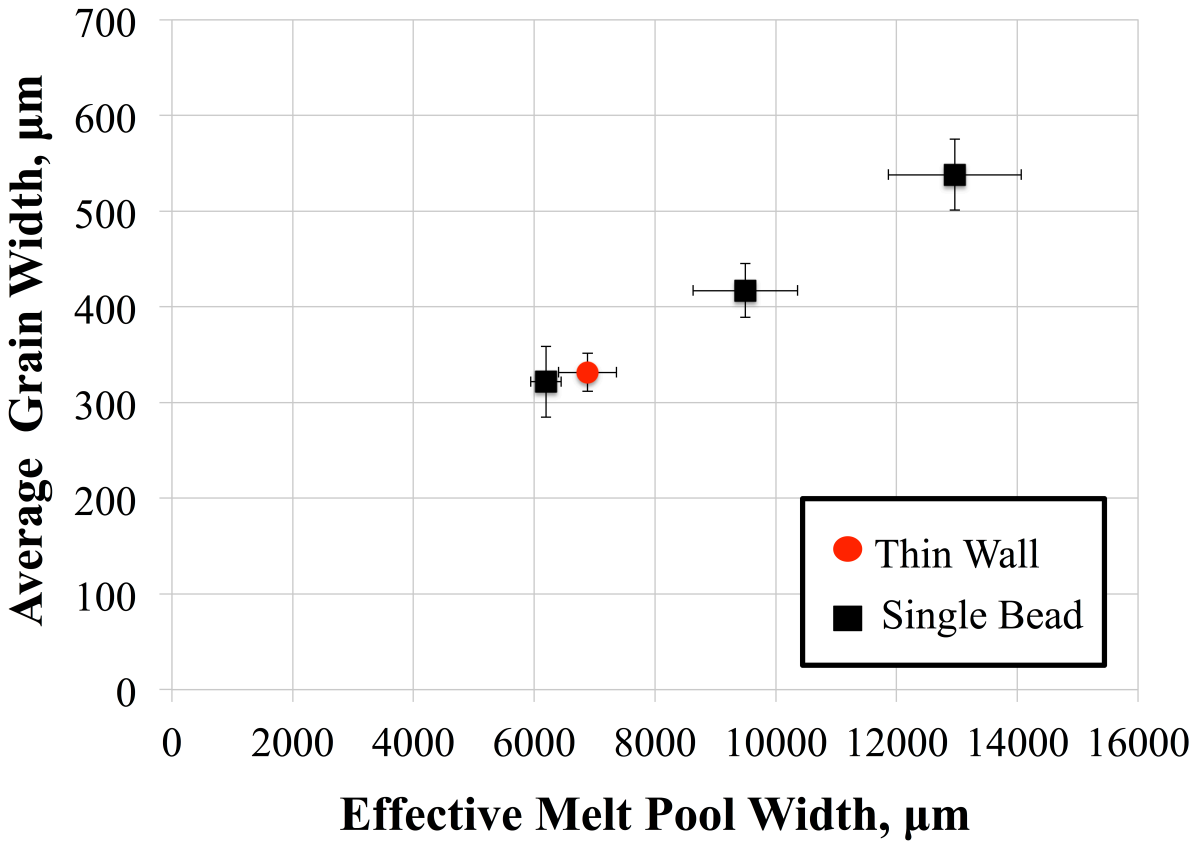

Figure 4.14: Comparison of single bead and thin wall grains per melt pool width

4.5 Chapter Summary

A P-V process map has been created for solidification microstructure control for thin wall depositions of Ti-6Al-4V using the electron beam wire feed process. Curves of constant beta grain size and regions of grain morphology are identified in beam power versus velocity space. Comparing the microstructure process map to the process map for controlling melt pool dimensions shows that a constant melt pool cross-sectional area results in a constant solidification cooling rate and therefore a constant beta grain size. Experimental results show that along a line of constant area a constant beta grain width is maintained. By comparing the beta grain width to the effective melt pool width for thin walls to that of single beads, it is seen that a scaling factor of ~20 grains per width is seen for both geometries. Also, there is evidence of equiaxed grains being present in all experimental cases, consistent with predictions from the simulations. Thin wall experiments for additional melt pool areas need to be performed in order to validate the relationship.

Results across two extreme cases of geometric constraint on conduction into the substrate suggest controlling melt pool width could be a geometry-independent means for indirectly controlling solidification microstructure. A control strategy for both melt pool geometry and microstructure also emerges. In transitioning between deposition geometries, beam power and velocity must be changed to maintain melt pool size and shape. However, once the melt pool size is maintained, beta grain size is also maintained, yielding consistent melt pool sizes, shapes and beta grain widths via a single control strategy.

Chapter 5 Process Mapping of Solidification Microstructure for Single Bead Deposits in the Electron Beam Powder Bed Process

5.1 Chapter Overview

The term "additive manufacturing" spans a variety of processes. As discussed in Chapter 1, the major direct metal AM processes can be split into four types: wire feed electron beam, electron beam powder bed, laser beam powder stream and laser beam powder bed. Each type of process works in a different area of processing space (different ranges of power and velocity) [5]. Results presented thus far are for the wire feed electron beam process. In this chapter, the process mapping of melt pool dimensions and solidification microstructure used for the electron beam wire feed process will be extended to the electron beam powder bed process. The paths of constant cooling rate in this region of processing space will be determined using finite element modeling and compared to the curves of constant melt pool dimensions. No added material and 1-layer of powder single pass experiments are analyzed for both melt pool dimensions and solidification microstructure.

5.2 Methods

5.2.1 Finite Element Analysis

The finite element model previously used to model the electron beam wire feed process is modified for the electron beam powder bed system and the modified version is seen in Figure 5.1. This model does not currently include the addition of powder, so no material is being added to the model. The applied heat flux is distributed over a specified width to simulate the spot size of the electron beam. Because the deposition takes place in a vacuum, the 3-D model does not include convective heat transfer the surfaces of the model. The problem is conduction dominated, so radiation is currently not being modeled. The nodes have an initial temperature of 973 K to simulate the preheating of the powder bed in the process. Eight-noded, linear brick elements are used throughout the model. The model is biased to the region where the data is being collected in order to reduce computation time. The height and width are chosen to be sufficiently large so there is no effect of the edges on the heat transfer. Temperature-dependent properties and latent heat are included to capture the nonlinear effects during solidification. The thermal gradients and cooling rates are extracted as the temperature changes from liquid to solid along the trailing edge of the melt pool.

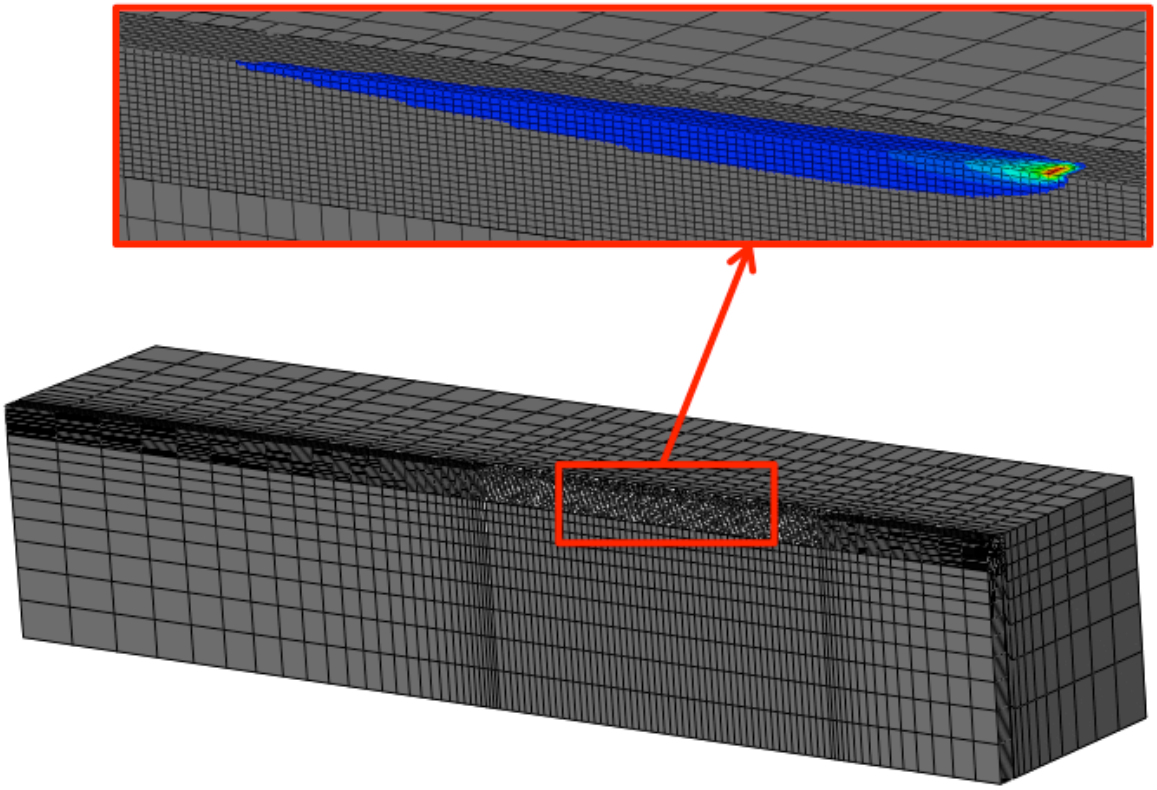

Figure 5.1: No added material FEA model for the electron beam powder bed process

5.2.2 Experiments

Two rounds of single pass Ti-6Al-4V deposition experiments for several power and velocity combinations were performed by North Carolina State University on the Arcam additive manufacturing machine. The first set of experiments did not add powder and was only "beam on plate." The second round of experiments included the addition of one layer of powder.

The plates are sectioned polished and etched to observe the melted boundary and the solidification microstructure. Images of the melt pool cross-sections and the top view of the

experiment plates are provided by collaborators at North Carolina State University. The top view of the no powder and 1-layer of powder cases are seen in Figure 5.2 and Figure 5.3. A sample micrograph can be seen in Figure 5.4. The melt pool area, melt pool width and beta grain size (grain width) are measured using Image J analysis program and the procedure that was outlined in Chapter 3.

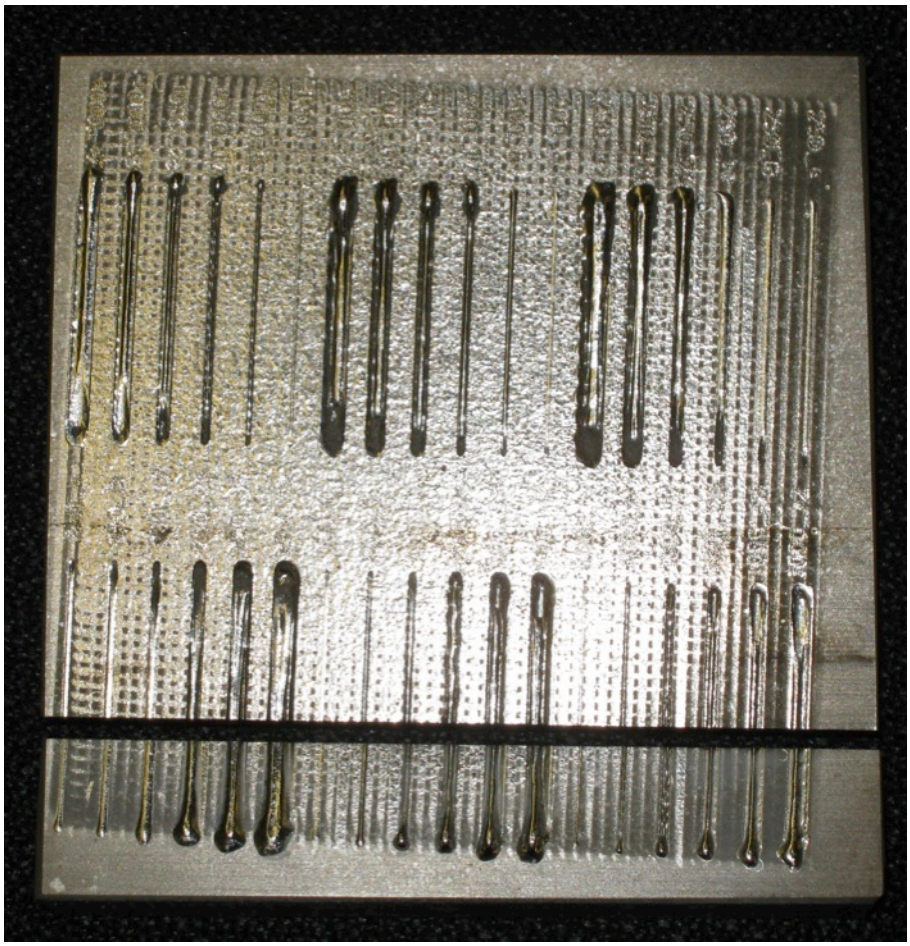

Figure 5.2: No added material single pass experiments

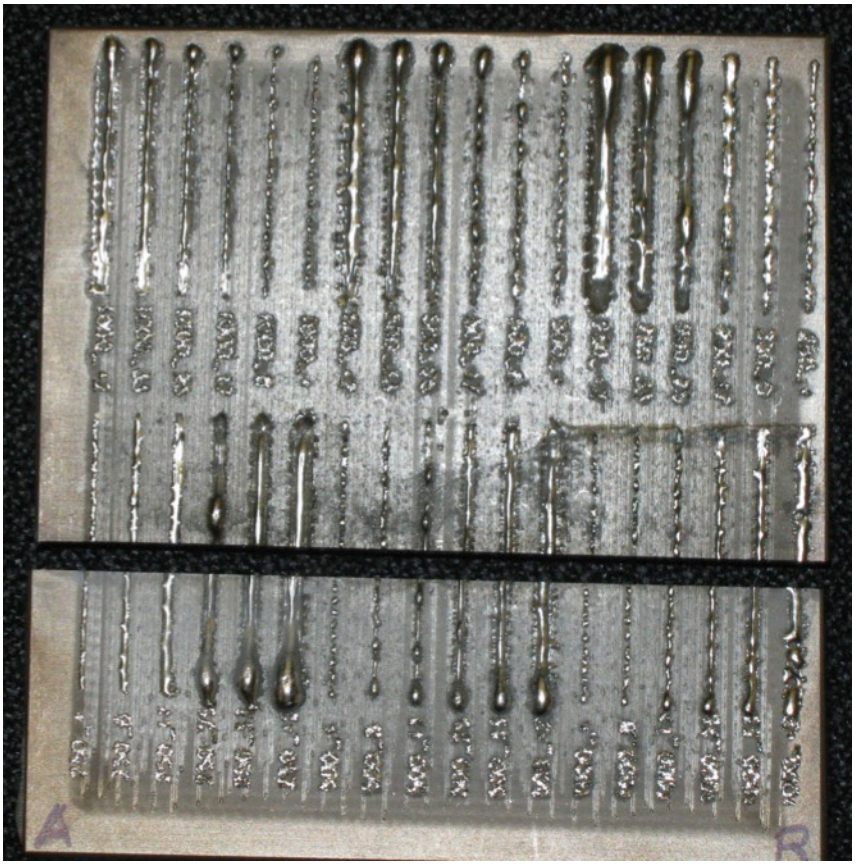

Figure 5.3: 1-layer of powder single pass experiments

Figure 5.4: Example cross section for the electron beam powder bed process

5.3 Modeling Results

5.3.1 Process Map for Solidification Microstructure Control in Electron Beam Powder Bed Processes

The P-V process map for solidification microstructure in the electron beam powder bed process is created in order to identify paths in processing space with a constant cooling rate and as well as regions of grain morphology. A constant cooling rate is assumed to result in a constant grain size. The grain morphology boundary is determined using a method similar to that used in in the previous sections of and the solidification map for Ti-6Al-4V. In order to encompass the high solidification rates obtained in the electron beam powder bed process, the G and R data is extrapolated linearly as seen in Figure 5.5.

The grain size and morphology data from the G vs. R plot in Figure 1 from Chapter 1, is translated onto a plot of power versus velocity using finite element material added simulations. Note that this is not the same morphology boundary as in the electron beam wire feed process The powder bed process has a higher background temperature because the entire build chamber is preheated and held at a higher temperature. The data presented here is for the top of the trailing edge of the melt pool, where the lowest gradients are present and the morphology region transitions will first take place. The thermal gradients along the solidification front span a larger range than those in the electron beam wire feed process, thus it is expected that there will only be a small percentage of the area with equiaxed grains. The result is the P-V process map for controlling solidification microstructure for single pass deposits of Ti-6Al-4V in an electron beam powder bed process seen in Figure 5.6.

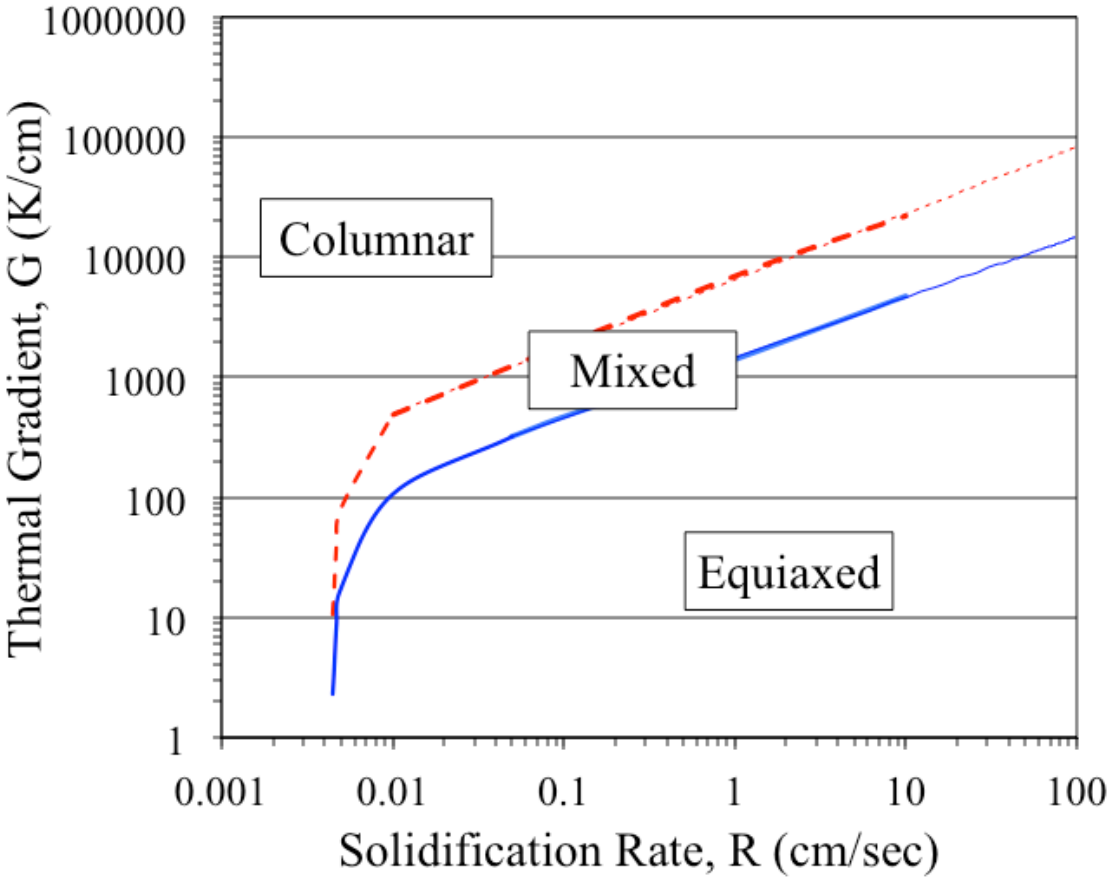

Figure 5.5: Extrapolated solidification map for Ti-6Al-4V

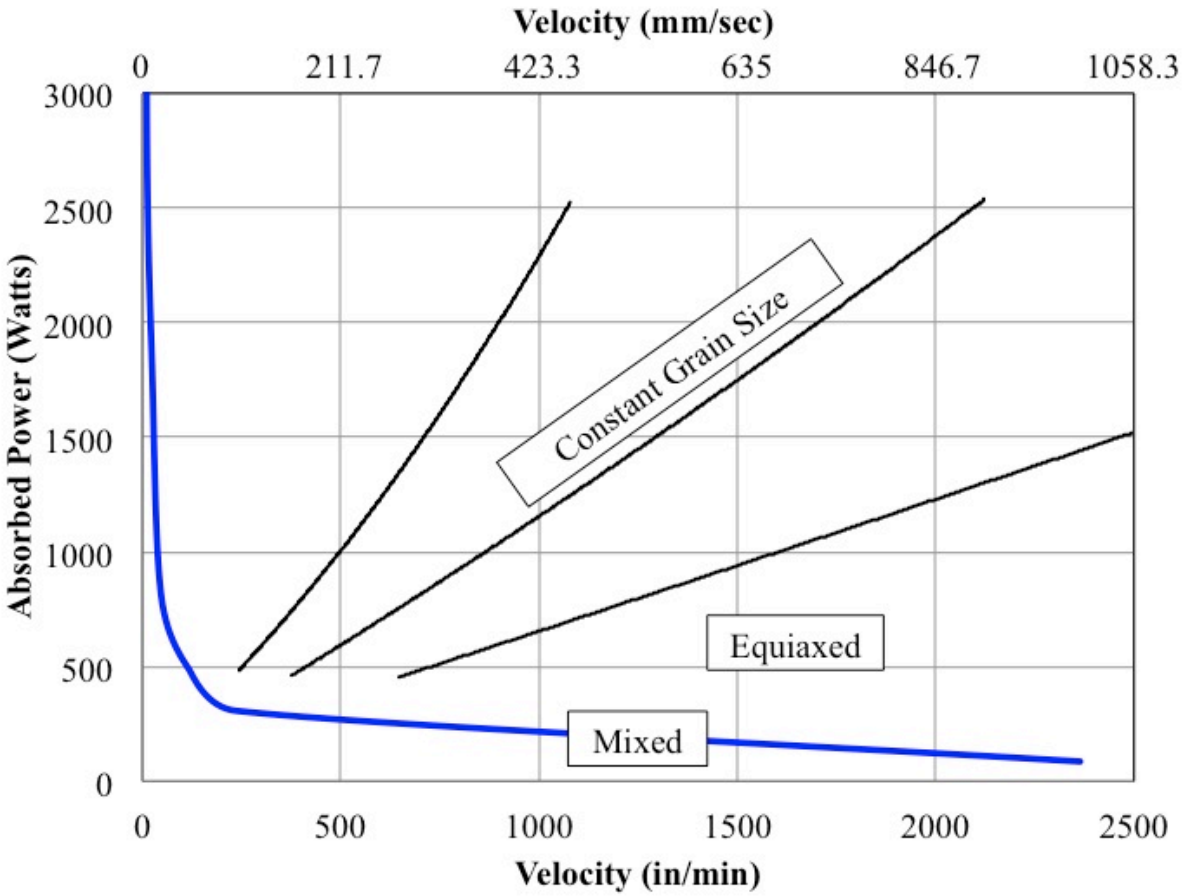

Figure 5.6: Solidification microstructure process map for the electron beam powder bed process

5.3.2 Integrated Control of Microstructure and Melt Pool Dimensions

In Chapter 2, it is shown that for the electron beam wire feed process, when maintaining a constant melt pool area, the grain size also remains constant. The process map for melt pool geometry control in the electron beam powder bed processes is seen in Figure 5.7 [94], the solidification microstructure is related to melt pool dimensions for electron beam powder bed processes. The curves of constant grain size in Figure 5.6 are similar to the curves of constant

melt pool area in Figure 5.7. Therefore, by controlling the melt pool area, a constant grain size is also maintained. This is the same relationship that was seen for the electron beam wire feed system. The grain morphology region boundaries are no longer similar to a line of constant length to depth ratio.

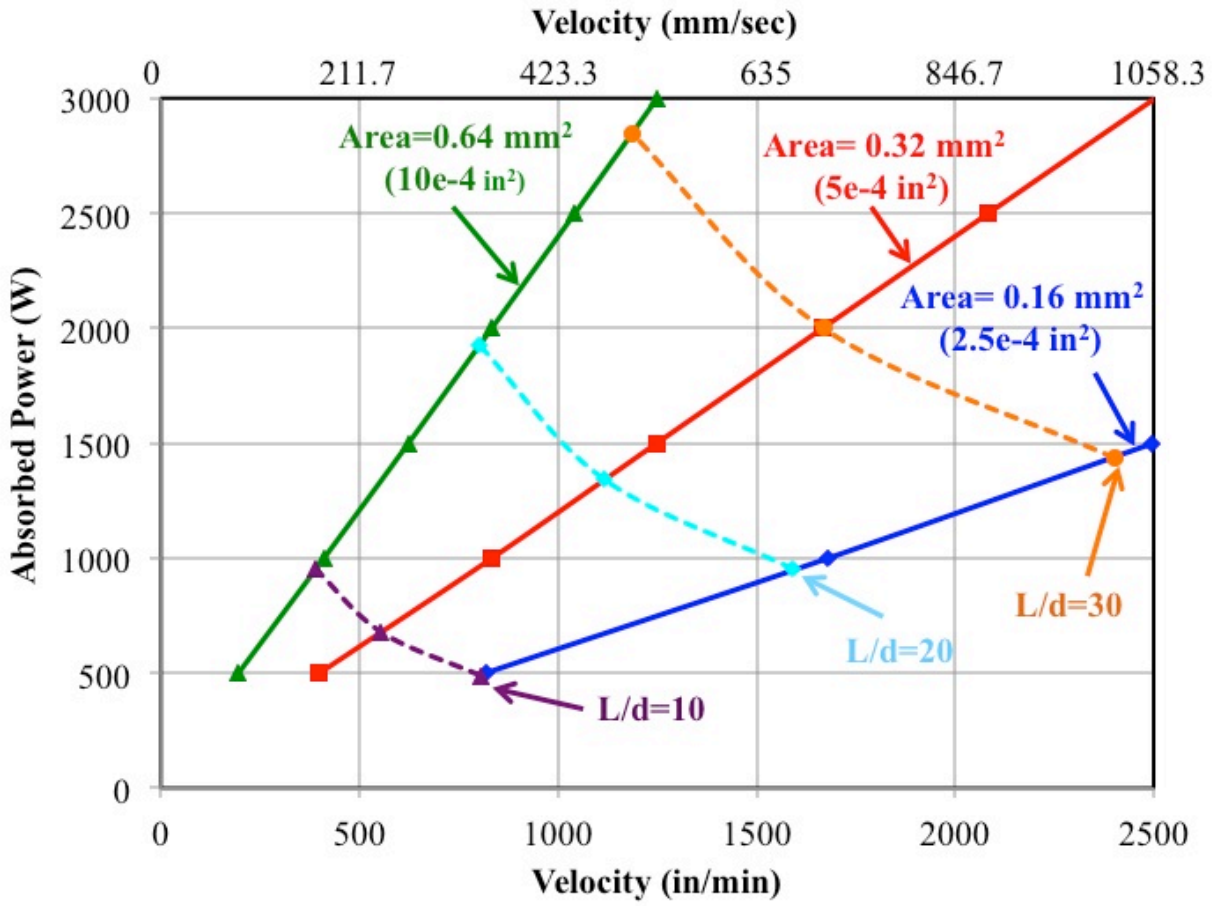

Figure 5.7: Melt pool dimensions process map for the electron beam powder bed process

5.4 Experimental Results

5.4.1 Bead Quality:

For some of the power and velocity combinations there are cases of not having a continuous bead. This is seen only in the 1-layer of powder cases. The non-continuous beads are

referred to as having a “bead up” and an example of which is shown in Figure 5.8. There are also experimental cases for which the material in the melt pool cross-section material is being pulled from the sides of the melt pool into the middle. This phenomenon is termed “dips.” An example cross section with dips is shown in Figure 5.9. The bead up and dips phenomenon are likely due to surface tension [95] and this work shows that these phenomenon are related to the melt pool size.

The experimental power and velocity combinations that exhibited either the bead up or dips are identified. The cases for which bead up and dips occur are grouped in regions of processing space. Lines are identified where bead up [96] and dips will begin to occur and are shown in Figure 5.10. For high power and low velocities, the dips phenomenon occurs which is indicated by the blue experiment points in Figure 5.10. The blue dashed line shows the boundary for which points above this line will have dips in the cross section. For lower powers and high velocities the bead up phenomenon occurs which is indicated by the red experimental points in Figure 5.10. The red dashed line shows the boundary for which points below this line will have bead up occurring. The lines for both dips and bead up are similar to lines of constant area in the melt pool dimensions process map of Figure 5.7. Therefore, for larger melt pool areas the dips will occur and for smaller melt pool areas the bead up will occur. It is expected that the location of the curves may shift based on the layer thickness of material that is being added.

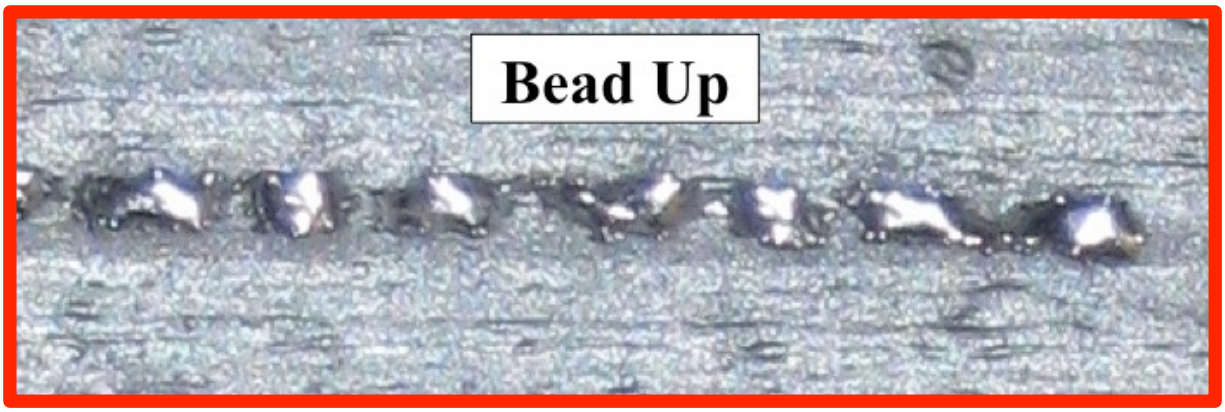

Figure 5.8: Single pass experiment top view beading up

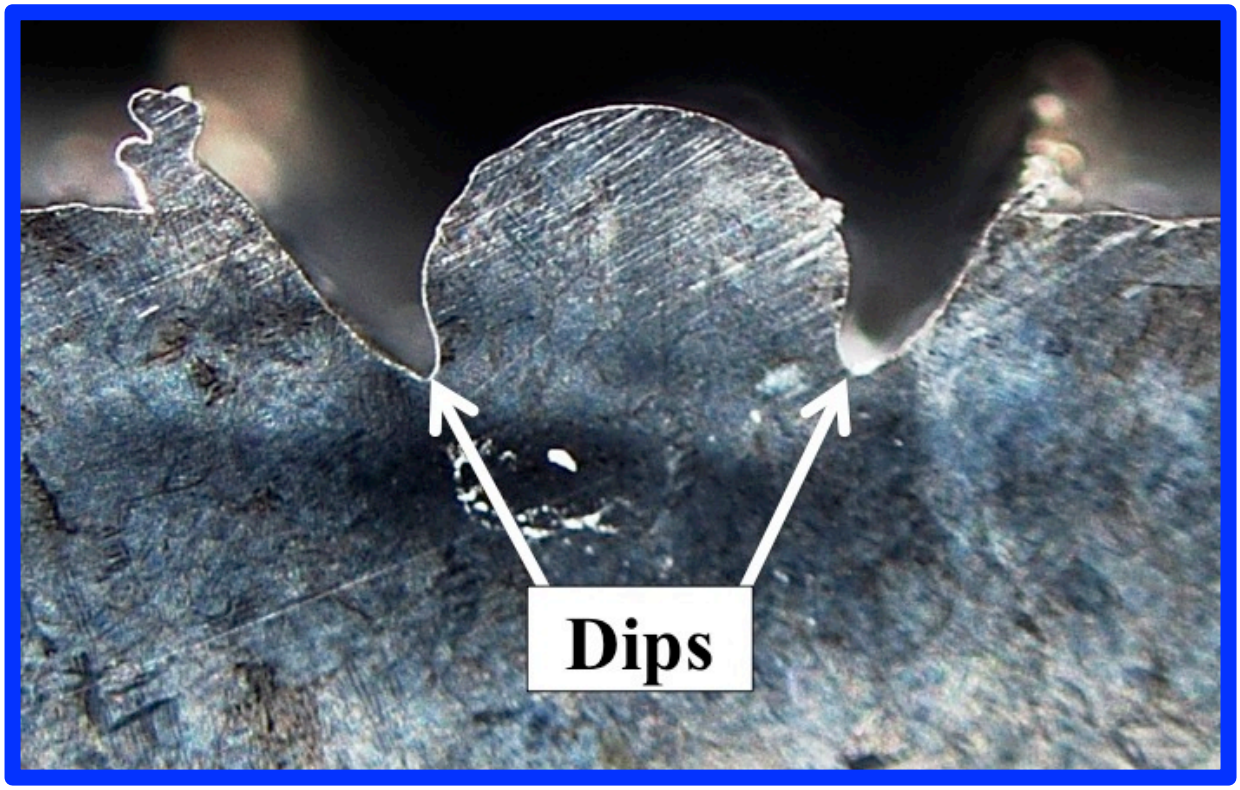

Figure 5.9: Dips phenomenon in single pass experiments

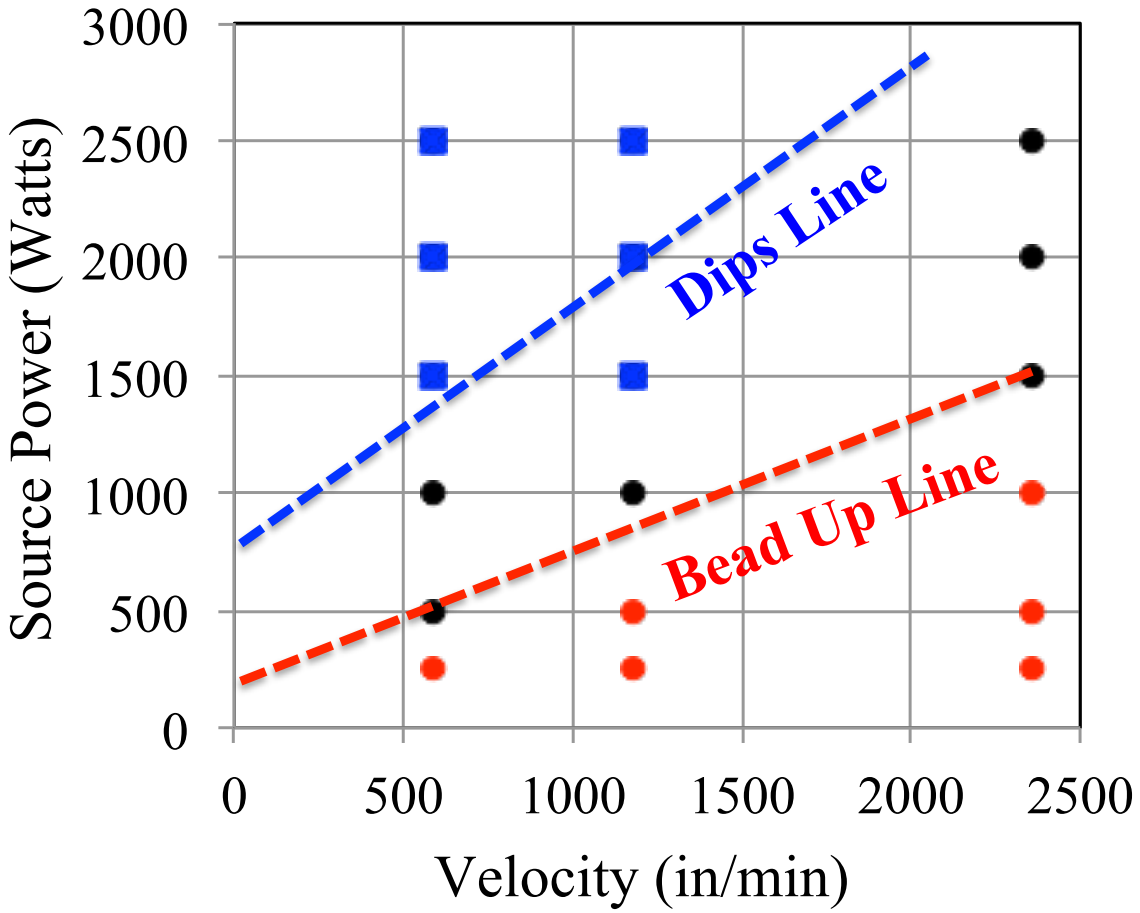

Figure 5.10: Bead up and dips lines in electron beam powder bed processing space

5.4.2 Melt Pool Area

The cross sectional melted area is measured for both the no added and 1-layer of powder cases. Because of the bead quality issues and the ambiguous melt pool boundary, the deposited versus melted regions cannot be measured for the electron beam powder bed process. The melted boundary is difficult to identify because there is no heat affect zone and epitaxial grain growth is occurring from grains in the substrate material.

The measured areas for the no powder and 1-layer of powder are compared in Table 5.1. In most cases the 1-layer of powder areas are larger than the no added material cases. The outlier at 1000W can be explained because the 1-layer of powder case is beading up. The cross section that was taken at a point in the bead where material was being pulled away from that cross section, therefore the area measured is too small. At the 2500 W outlier, the problem is likely with the no added measured area. The boundary is ambiguous and hence is difficult to identify the boundary and give an accurate measurement. In general, at any given power and velocity adding powder will result in a larger melted area than not adding powder.

Power	Velocity (in/min)	Velocity (mm/sec)	Cross Section Area (in^2)		Percent Difference
			1-Layer of Powder	No Powder	
500	591	250	0.00032		
1000	591	250	0.00083		
1000	1181	500	0.00013	0.00027	-70.3
1000	2362	1000	0.00023	0.00009	82.5
1500	591	250	0.00105	0.00086	20.5
1500	1181	500	0.00052	0.00031	51.3
1500	2362	1000	0.00044	0.00024	58.2
2000	591	250	0.00133	0.00120	10.1
2000	1181	500	0.00090	0.00050	56.3
2000	2362	1000	0.00043	0.00033	27.3
2000	591	250	0.00133	0.00120	10.1
2500	591	250	0.00174	0.00210	-18.8
2500	1181	500	0.00123	0.00076	47.3

Table 5.1: Cross section area in the electron beam powder bed process

The no added and 1-layer of powder cases are compared to the curves of constant melt pool area from finite element analysis. The experimental powers are converted to an absorbed power by multiplying by a factor of 0.9. The absorptivity is assumed to be the same value as that used for the electron beam wire feed process in the previous chapters. Comparison of the no added material experiments to the no added material finite element results will validate this assumption.

The experimental measurements are shown in Figure 5.11 plotted over the curves of constant melt pool area from finite element simulations. The no added material melt pool area measurements agree reasonably well with the finite element predictions, so the assumption of the absorptivity being 0.9 is correct. The melt pool area measurement values fall on the correct sides of the constant area curves. It is expected that the addition of powder will result in a larger melt pool area because conduction is constrained due to the lower conductivity of the powder surrounding the melted region. It is harder for heat to conduct away; therefore a larger melt pool is formed. The 1-layer of powder experimentally measured melt pool areas are larger than the areas predicted with the finite element models.

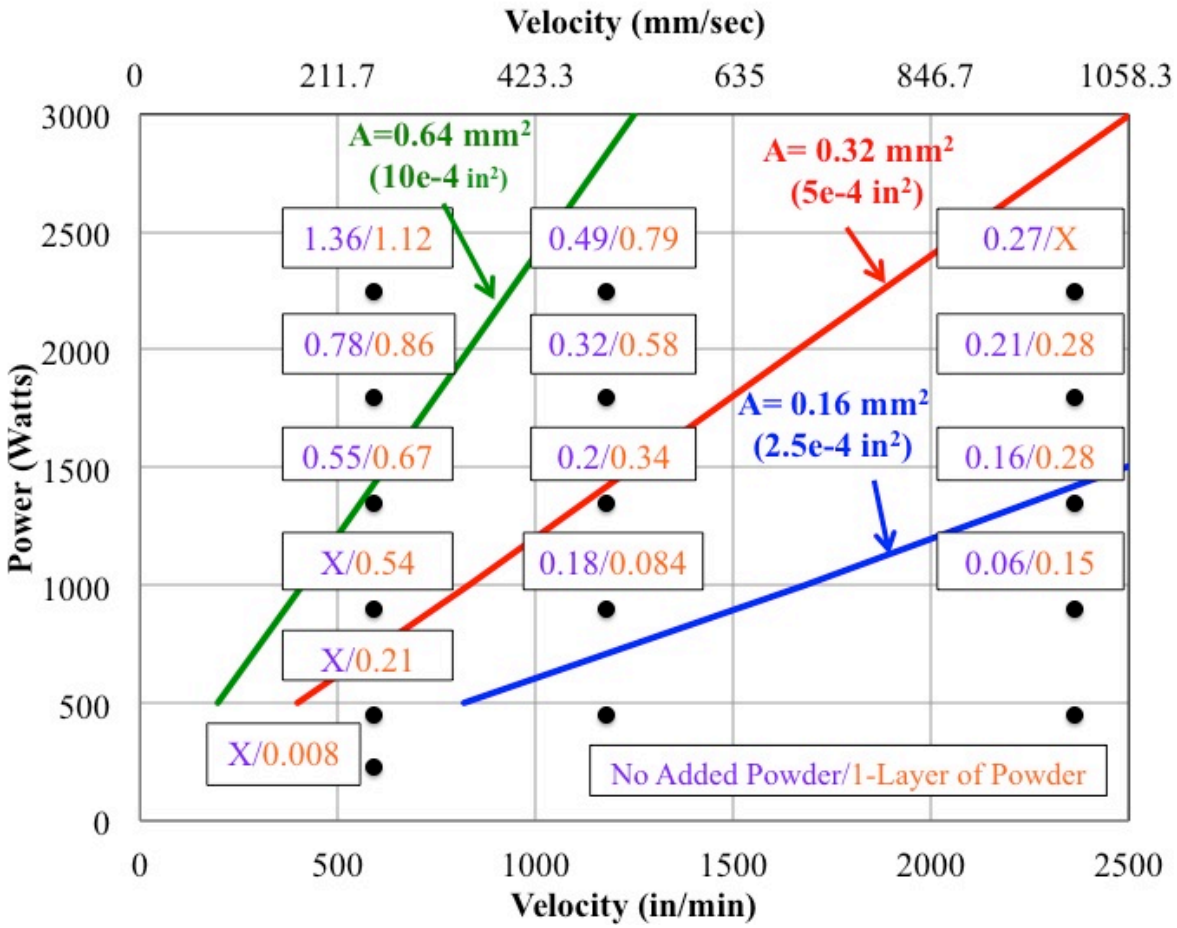

Figure 5.11: Melt pool area measurements in mm^2 of No added power/1-layer of power compared to curves of constant melt pool area from finite element simulations

The experimental melt pool cross section measurements are interpolated to identify the paths of constant melt pool area for three specified areas and are compared to finite element results. The interpolated experimental points for constant melt pool area and FEA curves of constant melt pool area for the electron beam powder bed process are seen in Figure 5.12. The hollow squares represent the no added material experimental cases while the solid circles represent the 1-layer of powder added experimental cases. The solid lines are the curves of constant melt pool area from the no added material finite element models. The interpolated experimental points are not shown for the area of 0.16 mm^2 because extrapolation would be required to obtain these points and the accuracy is reduced.

The no added material interpolated experiment points of constant area fall very close to the curves of constant area from finite element simulations. This result is expected because the addition of material is not being modeled. The 1-layer of powder interpolated points of constant melt pool area fall below the finite element curves. Therefore either the power must be reduced or the velocity should be increased in order to obtain the same melt pool area when material is added.

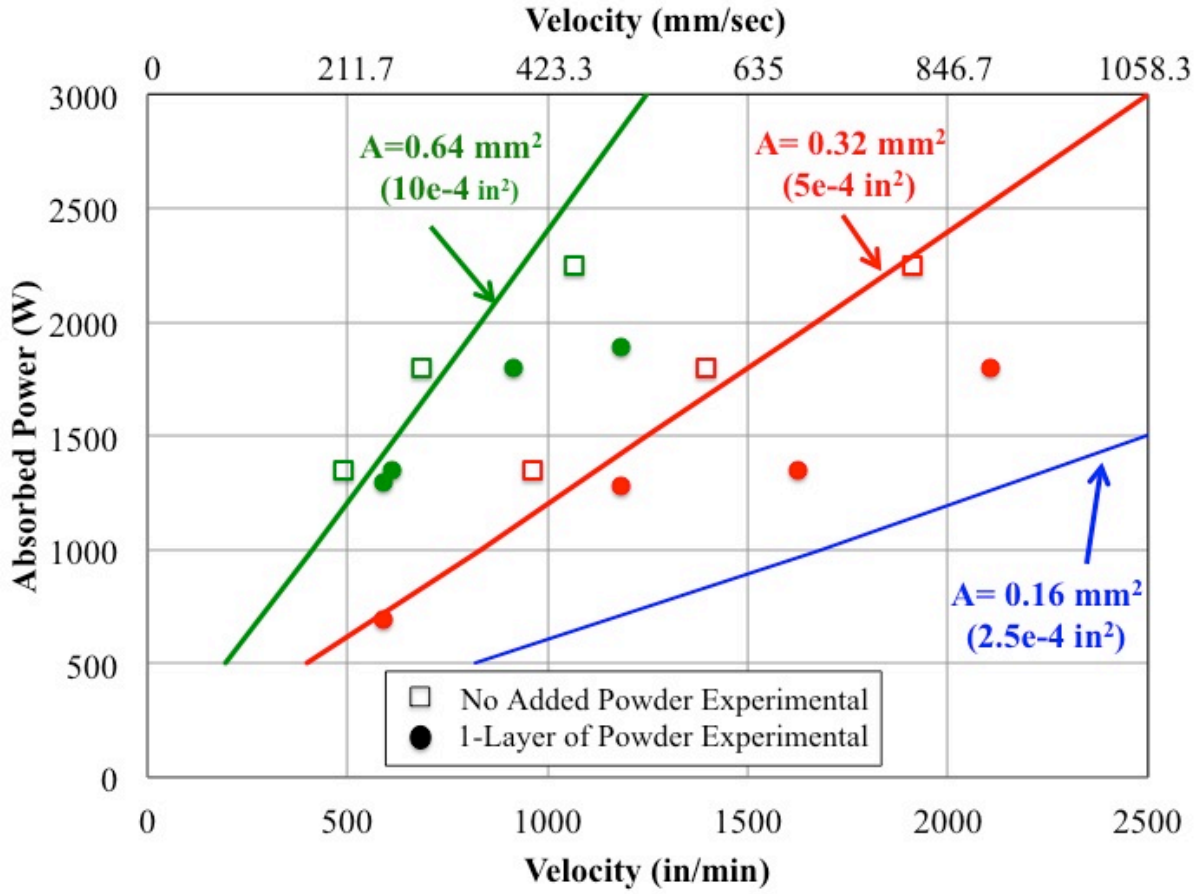

Figure 5.12: Interpolated experimental point for constant melt pool area and FEA paths of constant melt pool area

5.4.3 Solidification Microstructure

In the previous section, it is postulated that by maintaining a constant melt pool area, the grain size is also maintained constant. For both no added material and 1-layer of added material experiments, the beta grain size is measured. The beta grain width versus the effective melt pool width is plotted in Figure 5.13. In general, the grain size measured from the 1-layer of powder cross section is smaller than the no added experiments. This is the opposite of what is predicted because the cooling rate decreases when the paths of conduction is reduced. Additional experiments should be performed in order to obtain a higher number of data points to eliminate the possibility of discrepancy is due to scatter of the data.

The trend for both experimental cases is somewhat linear with a small amount of scatter that is normal for experimental measurements. For an increase in effective melt pool width, the grain width also increases. The grain size scales with the melt pool width with a ratio of approximately 7 grains per melt pool width. This is the same type of relationship that is seen for the electron beam wire feed process, but for that process the number of grains per width is approximately 20.

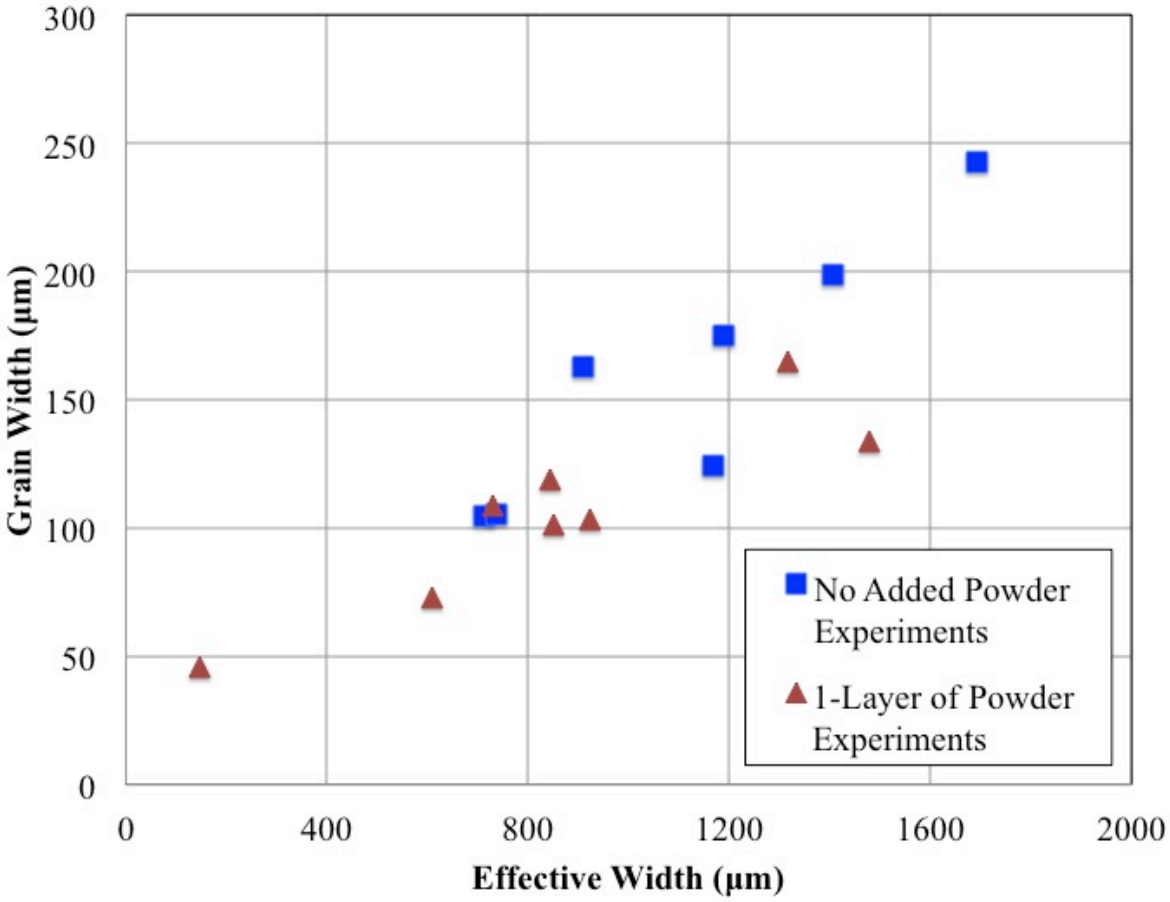

Figure 5.13: Beta grain size vs. effective melt pool width for single pass experiments in the electron beam powder bed process

The beta grain morphology for the single pass experiments is qualitatively observed. The predicted equiaxed transition indicates that equiaxed grains should be present in the no added power experimental cases. There are no clear regions of equiaxed grains as was seen in the electron beam wire feed systems. In the cases where equiaxed grains are present, there are scattered equiaxed and columnar grains mixed together. Detailed measurements of the aspect ratio of each grain should be performed in order to assess the grain morphology.

The solidification rates for this process are much higher than those on the previous solidification map used for the wire feed process and the data had to be extrapolated to obtain the mixed to equiaxed boundary in this region. This extrapolation may cause error in the predictions. Because the solidification rate is so high, there does not seem to be time for new grains to nucleate ahead of the columnar growth front and epitaxial growth from the substrate occurs. The experimental thermal conditions may also be different than those in the finite element model because of the bead up and dips phenomenon. In order to assess the validity of the solidification map by Kobryn [9] for the rapid solidification rates in the electron beam powder bed process, additional research must be completed. It is likely that the parameters in the solidification model must be modified.

5.5 Chapter Summary

The relationship between solidification microstructure and melt pool geometry is investigated for the electron beam powder bed process. The electron beam powder bed process has much smaller areas and higher cooling rates than the electron beam wire feed process. The process maps for both melt pool dimensions and solidification microstructure are presented. When comparing the two process maps it can be seen that by maintaining a constant melt pool area, a constant grain size will also be maintained. This is the same result as was seen for the electron beam wire feed process. The grain morphology boundary is no longer similar to the length to depth ratio.

Single bead experimental results are presented for a wide range of power and velocity combinations for no added material and 1-layer of powder cases. For the experimentally measured melt pool areas, the no added material melt pool area is smaller than the 1-layer of powder melt pool areas. This is an expected result because the paths of conduction are reduced when a layer a powder is added. The paths of constant melt pool area are identified for both sets of experiments. The no added experiments agree well with the finite element predictions, because no material was being added to the model. The trend of the 1-layer of powder experiments is the same but the constant melt pool area curve is shifted down in processing space.

The relationship between solidification microstructure and melt pool geometry is investigated for the electron beam powder bed process. The electron beam powder bed process has much smaller areas and higher cooling rates than the electron beam wire feed process. The process maps for both melt pool dimensions and solidification microstructure are presented.

When comparing the two process maps it can be seen that by maintaining a constant melt pool area, a constant grain size will also be maintained. This is the same result as was seen for the electron beam wire feed process. The grain morphology boundary is no longer similar to the length to depth ratio.

Single bead experimental results are presented for a wide range of power and velocity combinations for no added material and 1-layer of powder cases. For the experimentally measured melt pool areas, the no added material melt pool area is smaller than the 1-layer of powder melt pool areas. This is an expected result because the paths of conduction are reduced when a layer a powder is added. The paths of constant melt pool area are identified for both sets of experiments. The no added experiments agree well with the finite element predictions, because no material was being added to the model. The trend of the 1-layer of powder experiments is the same but the constant melt pool area curve is shifted down in processing space.

The measured beta grain size scales with the measured effective melt pool width, which confirms that the constant area and constant grain size relationship developed for the electron beam wire feed process can be extended to the electron beam powder bed process. However for the electron beam powder bed process the scaling factor is different, there are approximately 7 grains per melt pool width. This is the same type of relationship that was seen in the electron beam wire feed process, though the value of grains per width is different in both processes. There is no significant difference between the grain sizes in the no added and the 1-layer of powder cases. Further investigation must be performed to validate the grain morphology predictions in this region.

Chapter 6 Conclusions and Future Work

6.1 Conclusions

Part and process qualification has been identified as an important area of research for the AM field. This paper gives insight into regions or paths in processing space that can produce the desired solidification microstructure. In this work, P-V solidification microstructure process maps are created to represent solidification microstructure in terms of process parameters. Curves of constant beta grain size and regions of grain morphology are identified in beam power versus velocity space. These results are compared to the process maps for melt pool dimensions. Results show that integrated control of solidification microstructure and melt pool dimensions is possible for both single bead and thin wall geometries in the electron beam wire feed AM process and for single beads in the electron beam powder bed process. Integrated control of solidification microstructure and melt pool dimensions allows for the ability to indirectly control the solidification microstructure through direct, real time control of melt pool dimensions.

Comparing process maps for solidification microstructure (Figure 2.7 and Figure 4.7) to those for melt pool dimensions (Figure 2.8 and Figure 4.8) for both single bead and thin wall geometries in the electron beam wire feed process, shows that a constant melt pool area results in a constant grain size while moving through process space. Similarly, monitoring the length to depth ratio can control the grain morphology for single bead deposits. Experimentally, along a line of constant area, increasing the power results in more equiaxed grains and the grain size remains constant. A scaling factor of approximately 20 grains per melt pool width is identified

for the electron beam wire feed process. The scaling factor is geometry independent for deposition of single beads and thin walls seen in Figure 4.14.

The electron beam powder bed process has much smaller areas and higher cooling rates than the electron beam wire feed process, however the trends in solidification microstructure and melt pool dimensions are similar (Figure 5.6 and Figure 5.7). Maintaining a constant melt pool area results in a constant grain size. However, the scaling factor for the grains per melt pool width is now approximately 7 grains per width instead of 20 as seen in Figure 5.13. The effect of adding 1-layer of powder versus no added powder appears to have a significant effect on the melt pool area, but little effect on the grain size.

In situ microstructure control is possible by monitoring the real-time melt pool behavior. By integrating solidification microstructure and melt pool dimension control, balancing of high deposition rates, fine features and tailored microstructures results in efficiently produced near net shape parts with a consistent and predictable microstructure. This result can greatly accelerate process qualification and potentially allow for tailored microstructure and resulting mechanical properties for the desired application.

6.2 Implications of the Research

This research will give significant insight into regions of processing space that can produce the desired solidification microstructure and resulting mechanical properties. The added benefit of in-situ microstructure control is that it provides the ability to predict the microstructure

of different sections of a build based on the melt pool behavior, which will aid in decreasing the qualification time. Results of this work will potentially allow for tailoring of the microstructure and the resulting mechanical properties to the desired application.

6.3 Future Work

The process mapping approach for solidification microstructure is developed in this work to related solidification microstructure to input process variables. The major breakthrough in this work is the ability to indirectly control solidification microstructure through melt pool dimension control. Considerable progress has been made in the current research, and there are several directions that process mapping of microstructure can be extended further.

- Microstructural Characteristics: This work investigates the solidification microstructure (beta grain size and morphology), sometimes referred to as the macrostructure. The microstructure process mapping approach can be used to map out any other microstructural characteristics. For example, the cooling rate at the beta transus is a dominating factor in the alpha grain structure development. This cooling rate can be mapped out using the technique developed in this work. Determining the boundary for when martensite will be present has already completed as an extension of this work. [97]

- Material Systems: Ti-6Al-4V is the material investigated in this work. The microstructure process mapping approach can be used for any material system. The curves of constant cooling rate can be determined for any material for which the thermal properties are

know. Morphology regions require G and R solidification map data. This data can be found in the literature or developed through solidification modeling. [98]

- Types of Additive Manufacturing Processes: Electron beam wire feed and electron beam power bed additive manufacturing processes are explored in this work. The integrated process mapping of solidification microstructure and melt pool dimensions can be extended to any thermally based additive manufacturing process. Due to the deviation of the constant area and constant cooling rate at lower powers, it is expected that investigation of lower power additive manufacturing will show that the relationship no longer holds.

- Deposit Geometries: Single bead deposits and thin wall deposits are discussed in this work. Process mapping of additional key geometries such as depositing along a free edge, around a corner or depositing beads side by side can be used to strategically build an entire part with a tailored microstructure.

References

[1] I Gibson, D. W. Rosen, and B. Stucker, *Additive Manufacturing Technologies*. New York: Springer, 2010.

[2] K M Taminger and R A Hafley, "Electron Beam Freeform Fabrication: a rapid metal deposition process," in *3rd Annual Automotive Composites Conference*, 2003.

[3] K. M. Taminger and R. A. Hafley, "Electron Beam Freeform Fabrication for Cost Effective Near-Net Shape Manufacturing," NATO/RTOAVT-139 Specialist' Meeting on Cost Effective Manufacture via Net Shape Processing, Amsterdam, Netherlands, 2006.

[4] J W Sears, "Direct Laser Powder Deposition- "State of the Art," Knolls Atomic Power Laboratory, Schenectady, New York, Tech. Rep. 1999.

[5] J. Beuth et al., "Process Mapping for Qualification Across Multiple Direct Metal Additive Manufacturing Processes," in *Solid Freeform Fabrication Proceedings*, 2013.

[6] F. Arcella and F. Froes, "Producing Titanium Aerospace Components from Powder Using Laser Forming," *JOM*, vol. 52, pp. 28-30, 2000.

[7] M. Donachie, *Titanium: A Technical Guide*.: ASM, 2007.

[8] G. Lutjering and J. C. Williams, *Titanium, Second Edition*.: Springer, 2007.

[9] P. Kobryn and S. Semiatin, "Microstructure and Texture Evolution During Solidification Processing of Ti-6Al-4V," *Journal of Materials Processing Technology*, vol. 13, pp. 330-339, 2003.

[10] J. Beuth, N. Klingbeil, and J. Gockel, "Process Mapping of Cooling Rates and Thermal Gradient," PCT/US2013/055422, August 16, 2013.

[11] J. Beuth, N. Klingbeil, and J. Gockel, "Process Mapping of Cooling Rates and Thermal Gradients," Provisional Patent 61/742,734, August 17, 2012.

[12] J. L. Beuth, "Methods for Determing Process Variable Combinations Yielding Constant Melt Pool Geometry for Single Bead Deposits in Direct Digital Manufacturing," 6/574, 252, filed July 29, 2011.

[13] J. L. Beuth and J. C. Fox, "Process Mapping of Thermal Response Due to Process Variable Changes," filed March 15, 2013.

[14] P Kobryn and S Semiatin, "The Laser Additive Manufacture of Ti-6Al-4V," *JOM*, vol. 53, no. 9, pp. 40-42, 2001.

[15] J. Gockel and J. Beuth, "Understanding Ti-6Al-4V Microstructure Control in Additive Manufacturing via Process Maps," in *Solid Freeform Fabrication Proceedings*, Austin, 2013, pp. 666-674.

[16] R. Grylls, "Laser Engineered Net Shapes," *Advanced Materials and Processes*, p. 45, 2003.

[17] N. Dey, F. W. Liou, and C. Nedic, "Additive Manufacturing Laser Deposition of Ti-6Al-4V for Aerospace Repair Applications," *Solid Freeform Fabrication Symposium Proceedings*, 2013.

[18] [Online]. www.geaviation.com/company/additive-manufacturing.html

[19] S. Rawal, J. Brantley, and N. Karabudak, "Additive Manufacturing of Ti-6Al-4V Alloy Components for Spacecraft Applications," Lockheed Martin Space Systems, Tech Brief

2013.

[20] T. Horn and O. Harrysson, "Overview of current additive manufacturing technologies and selected applications," *Science Progress*, 2012.

[21] O. Harrysson, O. Cansizoglu, D. J. Marcellin-Little, D. R. Cormier, and H. A. West, "Direct metal fabrication of titanium implants with tailored materials and mechanical properties using electron beam melting technology," *Materials Science and Engineering C*, vol. 28, no. 3, pp. 366-373, 2008.

[22] T. Wohlers, "Wholers Report 2013: Additive Manufacturing State of the Industry: Annual World Wide Progress Report," Wholers Associates, 2013.

[23] ASTM Standard F2792-10, "Standard Terminology for Additive Manufacturing Technologies," ASTM International , 2013.

[24] K. Taminger and R. A. Hafley, "Electron Beam Freeform Fabrication: A Rapid Metal Deposition Process," in *Proceedings of the 3rd Annual Automotive Composites Conference*, Troy, MI, 2003.

[25] R Martukanitz, T. Simpson, and G. Messing, "Additive Manufacturing: Hype vs. Reality Perspectives from an Additive Manufacturing Demonstration Facility," Pennsylvania State University, Presentation 2014.

[26] R. P. Mudge and N. R. Wald, "Laser Engineered Net Shaping Advances Additive Manufacturing and Repair," *Welding Journal*, January 2007.

[27] S. Rengers, "Electron Beam Melting (EBM) vs. Select Metal Laser Sintering (DMLS)," in *DPM Workshop 2012*, November 2012.

[28] Arcam A2 Technical Data. [Online]. www.arcam.com/wp-content/uploads/Arcam-A2.pdf

[29] M. F. V. T. Pereira, M. Williams, and W. B. du Preez, "Application of laser additive manufacturing to produce dies for aluminum high pressure die-casting," *South African Journal of Industrial Engineering*, vol. 23, no. 2, Oct. 2012.

[30] J. Gausemeier, N. Echterhoff, and M. Wall, "Thinking Ahead the Future of Additive Manufacturing- Innovation Roadmapping of Required Advancements," Heinz Nixdorf Institute, University of Paderborn, 2013.

[31] [Online]. www.sciaky.com

[32] M. L Griffith et al., "Laser engineered net shaping (LENS) for the fabrication of metalic components," in *Advanced Materials Developement, Characterization, Processing and Mechanical Behavior (Book of Abstracts)*, 1996.

[33] Arcam. [Online]. www.arcam.com/technology/electron-beam-melting/

[34] H. Weiwei, J. Wenpeng, T. Haiyan, K. Xinting, and H. Yu, "Research on preheating of titanium alloy powder in electron melting technology ," *Rare Metal Materials Engineering* , vol. 40, no. 12, pp. 2072-2075, 2011.

[35] [Online]. www.3dsystems.com/quickparts/learning-center/sls-anatomy

[36] D. Eylon, J. R. Newman, and J. K. Thorne, *Metals Handbook*, 10th ed. Materials Park, OH: ASM Int, 1990, vol. 2.

[37] R. R. Boyer, "An overview on the use of titanium in the aerospace industry," *Materials Science and Engineering A*, pp. 103-114, 1996.

[38] Steve Lampman, "Properties of Titanium Alloy Welds," in *Weld Integrity and Performance*.: ASM International, 1997, pp. 311-327.

[39] J. Blackburn, "Laser welding of metals for aerospace and other applications," in *Welding and Joining of Aerospace Materials*.: Elsevier, 2011.

[40] J. W. Elmer, T. A. Palmer, S. S. Babu, W. Zhang, and T. DebRoy, "Phase transformation dynamics during welding of Ti-6Al-4V," *Journal of Applied Physics*, vol. 95, no. 12, June 2004.

[41] T. F. Broderick, A. G. Jackson, H. Jones, and F. H. Froes, "The effect of cooling conditions on the microstructure of rapidly solidified Ti-6Al-4V," *Metallurgical Transactions A*, vol. 16, no. 11, pp. 1951-1959, 1985.

[42] P. G. Boswell and G. A. Chadwick, "The Grain Size of Splat-Quenched Alloys," *Scripta Metallurgica*, vol. 11, pp. 459-465, 1977.

[43] P. Kobryn, E. Moore, and S. Semiatin, "The Effect of Laser Power and Traverse Speed on Microstructure, Porosity and Build Heightin Laser Deposited Ti-6Al-4V," *Scripta Materialia*, vol. 43, pp. 299-305, 2000.

[44] W. Hofmeister et al., "Investigating Solidification with the Laser-Engineered Net Shaping Process," *Journal of Materials*, vol. 51, no. 7, July 1999.

[45] J. D. Hunt, "Steady State Columnar and Equiaxed Growth of Dendrites and Eutectic," *Materials Science and Engineering* , vol. 65, pp. 75-83, 1984.

[46] S. C. Flood and J. D. Hunt, "Columnar and Equiaxed Growth Part II: Equiaxed growth ahead of a columnar front," *Journal of Crystal Growth*, vol. 82, 1987.

[47] M. Gaumann, R. Trivedi, and W. Kurz, "Nucleation ahead of the advancing interface in directional solidification," *Materials Science and Engineering A*, vol. 226-228, pp. 763-769, 1997.

[48] B. Baufeld, O. Van der Biest, and R. Gault, "Additive manufacturing of Ti-6Al-4V components by shaped metal deposition: Microstructure and Mechanical Properties," *Materials and Design*, vol. 31, pp. 106-111, June 2010.

[49] B. Baufeld, E. Brandl, and O. Van der Biest, "Wire based additive layer manufacturing: Comparision of microstructure and mechanical properties of Ti-6Al-4V componenets fabricated by laser-beam deposition and shaped metal deposition," *Journal of Materials Processing Technology*, vol. 211, no. 6, pp. 1146-1158, 2011.

[50] E. Brandl, C. Leyens, and F. Palm, "Mechanical Properties of Additive Manufactured Ti-6Al-4V Using Wire and Powder Based Processes," in *Trends in Aerospace Manufacturing*, 2009.

[51] E. Brandl, A. Schoberth, and C. Leyens, "Morphology, microstructure, and hardness of titanium (Ti-6Al-4V) blocks deposited by wire-feed additive layer manufacturing (ALM)," *Materials Science and Engineering A*, vol. 532, pp. 295-307, 2012.

[52] E. Brandl, B. Baufeld, C. Leyens, and R Gault, "Additive manufactured Ti-6Al-4V using welding wire: comparison of laser and arc beam deposition and evaluation with respect to aerospace material specifications," *Physics Procedia*, pp. 595-606, 2010.

[53] F. Wang, S. Williams, P. Colegrove, and A. A. Antonysamy, "Microstruture and Mechanical Properties of Wire and Arc Additive Manufactured Ti-6Al-4V," *Metallurgical and Materias*

Transactions A, vol. 44, no. 2, pp. 968-977, 2013.

[54] A. A. Antonysamy, J. Meyer, and P. B. Prangnell, "Effect of build geometry on the beta-grain structure and texture in additive manufacture of Ti6Al4V by selective electron beam melting," *Materials Characterization*, vol. 84, pp. 153-168, 2013.

[55] A. Antonysamy, P. Prangnell, and J. Meyer, "Effect of Wall Thickeness Transitions on Texture and Grain Structure in Additive Layer Manufacture (ALM) of Ti-6Al-4V," *Materials Science Forum*, pp. 205-210, 2012.

[56] L. Thijs, F. Verhaeghe, T. Craeghs, J. V. Humbeeck, and J. P. Kruth, "A study of the microstructural evolution during selective laser melting of Ti-6Al-4V," *Acta Materialia*, vol. 58, no. 9, pp. 3303-3312, 2010.

[57] K. Puebla et al., "Effect of Melt Scan Rate on Microstructure and Macrostructure for Electron Beam Melting of Ti-6Al-4V," *Materials Science and Applications*, vol. 3, pp. 259-264, 2012.

[58] N. Hrabe and T. Quinn, "Effects of processing on microstructure and mechanical properties of a titanium alloy (Ti-6Al-4V) fabricated using electron beam melting (EBM), Part 1: Distance from build plate and part size," *Materials Science and Engineering: A*, vol. 573, pp. 264-270, June 2013.

[59] N. Hrabe and T. Quinn, "Effects of processing on microstructure and mechanical properties of a titanium alloy (Ti-6Al-4V) fabricated using electron beam melting (EBM), Part 2: Energy input, orientation and location," *Materials Science and Engineering: A*, vol. 573, pp. 271-277, June 2013.

[60] N. W. Klingbeil, J. W. Zinn, and J. L. Beuth, "Measurement of residual stresses in parts created by shape deposition manufacturing," in *Solid Freeform Fabrication Proceedings*, Austin, 1997, pp. 125-132.

[61] N. W. Klingbeil, J. L. Beuth, R. K. Chin, and C. H. Amon, "Measurement and modeling of residual stress-induced warping in direct metal deposition processes," in *Solid Freeform Fabrication Proceedings*, Austin, 1998, pp. 367-374.

[62] R. Ong, J. L. Beuth, and L. E. Weiss, "Residual stress control issues for thermal deposition of polymers in SFF processes," in *Solid Freeform Fabrication Symposium*, Austin, 2000, pp. 209-218.

[63] N. W. Klingbeil, J. L. Beuth, R. K. Chin, and C. H. Amon, "Residual stress-induced warping in direct metal solid freeform fabrication," *International Journal of Mechanical Sciences*, vol. 44, pp. 57-77, 2002.

[64] A. Vasinonta, J. Beuth, and M. Griffith, "Process Map for Controlling Residual Stress and Melt Pool Size in Laser-Based SFF Processes," in *Solid Freeform Fabrication Proceedings*, Austin, TX, 2000, pp. 200-208.

[65] A. Vasinonta, J. L. Beuth, and M. L. Griffith, "Process maps for predicting residual stress and melt pool size in the laser-based fabrication of thin-walled structures," *ASME Journal of Manufacturing Science and Engineering*, vol. 129, no. 1, pp. 101-109, 2007.

[66] J. Beuth and N. Klingbeil, "The Role of Process Variables in Laser-Based Direct Metal Solid Freeform Fabrication," *JOM*, pp. 36-39, September 2001.

[67] A Vasinonta, "Process Maps for Melt Pool Size and Residual Stress in Laser-Based Solid

Freeform Fabrication," Carnegie Mellon University, PhD Thesis 2002.

[68] A. Vasinonta, J. Beuth, and M. Griffith, "Process maps for predicting residual stress and melt pool size in the laser-based fabrication of thin-walled structures," *Journal of Manufacturing Science and Engineering*, vol. 129, no. 1, pp. 101-109, 2007.

[69] A. Vasinonta, J. L. Beuth, and R. Ong, "Melt pool size control in thin-walled and bulky parts via process maps," in *Solid Freeform Fabrication Proceedings*, 2001, pp. 432-440.

[70] A. Vasinonta, J. Beuth, and M. Griffith, "A Process Map for Consistent Build Conditions in the Solid Freeform Fabrication of Thin-Walled Structures," *ASME Journal of Manufacturing Science and Engineering*, vol. 123, pp. 615-622, 2001.

[71] A. Vasinonta, J. Beuth, and M. Griffith, "Process Maps for Laser Deposition of Thin-Walled Structures," in *Solid Freeform Fabrication Proceedings*, Austin, TX, 1999, pp. 383-391.

[72] A. J. Birnbaum, P. Aggarangsi, and J. L. Beuth, "Process Scaling and Transient Melt Pool Size Control in Laser-Based Additive Manufacturing Processes," in *Solid Freeform Fabrication Proceedings*, Austin, 2003, pp. 328-339.

[73] P Aggarangsi, J Beuth, and M. L Griffith, "Melt pool size and stress control for laser-based deposition near a free edge," in *Solid Freeform Fabrication Proceedings*, Austin, TX, 2003, pp. 196-207.

[74] E. Soylemez, J. Beuth, and K. Taminger, "Controlling Melt Pool Dimensions Over a Wide Range of Material Deposition Rates in Electron Beam Additive Manufacturing," in *Solid Freeform Fabrication Proceedings*, Austin, TX, 2010, pp. 571-582.

[75] J. Fox and J. Beuth, "Process mapping of transient melt pool response in wire feed E-beam Additive Manufacturing of Ti-6Al-4V," in *Solid Freeform Fabrication Proceedings*, 2013, pp. 675-683.

[76] N W Klingbeil, C Brown, S Bontha, P Kobryn, and H Fraser, "Prediction of Microstructure in Laser Deposition of Titanium Alloys," in *Solid Freeform Fabrication Proceedings*, Austin, TX, 2002, pp. 142-149.

[77] N Klingbeil et al., "Effects of Process Variables and Size Scale on Solidification Microstructure in Laser-Based Solid Freeform Fabrication of Ti-6Al-4V," in *Solid Freeform Fabrication Proceedings*, Austin, TX, 2004.

[78] S Bontha, "The Effect of Process Variables on Microstructure in Laser Deposited Materials," Wright State University, PhD Thesis 2006.

[79] S. Bontha and N. Klingbeil, "Thermal Process Maps for Controlling Microstructure in Laser-Based Solid Freeform Fabrication," *Solid Freeform Fabrication Proceedings*, pp. 219-226, 2003.

[80] S. Bontha, N. Klingbeil, P. Kobryn, and H. L. Fraser, "Effects of Process Variables and Size Scale on Solidification Microstructure in Beam-Based Fabrication of Bulky 3D Structures," *Materials Science and Engienering A*, vol. 513-514, pp. 311-318, 2009.

[81] S. Bontha, N. Klingbeil, P. Kobryn, and H. Fraser, "Thermal Process Maps for Predicting Solidification Microstructure in Laser Fabrication of Thin Wall Structures," *Journal of Materials Processing Technology*, vol. 178, pp. 135-142, 2006.

[82] C. J. Brown, "Modeling of Solidification Microstructure in Laser-Deposited Ti-6Al-4V," Wright State University, Master's thesis 2003.

[83] J Davis, N Klingbeil, and S Bontha, "Effect of Free-Edges on Melt Pool Geometry and Solidification Microstructure in Beam-Based Fabrication of Bulky 3-D Structures," in *Solid Freeform Fabrication Proceedings*, Austin, TX, 2010.

[84] J Davis, N Klingbeil, and S Bontha, "Effect of Free-Edges on Melt Pool Geometry and Solidification in Beam-Based Fabrication of Thin-Wall Structures," in *Solidification Freeform Fabrication Proceedings*, Austin, TX, 2009.

[85] M. Gaumann, S. Henry, F. Cleton, J. D. Wagniere, and W. Kurz, "Epitaxial laser metal forming: analysis of microstructure formation," *Materials Science and Engineering: A*, vol. 271, no. 1-2, pp. 232-241, November 1999.

[86] M. Gaumann, C. Bezencon, P. Canalis, and W. Kurz, "Single-crystal laser deposition of superalloys: processing-microstructure maps," *Acta Materialia*, vol. 49, no. 6, pp. 1051-1062, April 2001.

[87] W. Kurz, C. Bezencon, and M. Gaumann, "Columnar to equiaxed transition in solidification processing," *Science and Technology of Advanced Materials* , vol. 2, pp. 185-191, 2001.

[88] W. Liu and J. N. DuPont, "Effects of melt-pool geometry on crystal growth and microstructure development in laser surface-melted superalloy single crystals. Mathematical modeling of single-crystal growth in a melt pool (part 1)," *Acta Materialia*, vol. 52, pp. 4833-4847, 2004.

[89] D Rosenthal, "The Theory of Moving Sources of Heat and Its Applications to Metal Treatments," *Transactions of ASME*, vol. 68, pp. 849-866, 1946.

[90] R Dykhuizen and D Dobranich, "Analytical Thermal Models for the LENS Process," *Sandia National Laboratories Internal Report*, 1998.

[91] R Dykhuizen and D Dobranich, "Cooling Rates in the LENS Process," *Sandia National Laboratories Internal Report*, 1998.

[92] D. Dobranich and R. C. Dykhuizen, "Scoping Thermal Calculation of the LENS Process," Sandia National Laboratories Internal Report, Internal Report 1998.

[93] ASTM Standard E112-13, "Standard Test Methods for Determining Average Grain Size," ASTM International, West Conshocken, PA, 2013.

[94] J. Fox, "Unpublished research," Carnegie Mellon University, Internal Report 2014.

[95] C. Korner, E. Attar, and P. Heinl, "Mesoscopic simulation of selective beam melting processes," *Journal of Materials Processing Technology*, vol. 211, no. 6, p. 978987, June 2011.

[96] D. Christiansen, "Unpublished Research," Carnegie Mellon University, Internal Report 2013.

[97] H. Doak, "Effect of process variables on sub-melt-thermal behavior and solid-state phase transformations in beam-based additive manufacturing of Ti-6Al-4V," Wright State University, Master's Thesis 2013.

[98] J. Thompson, "Relating microstructure to process variables in beam-based additive manufacturing of INCONEL 718," Wright State University, Master's Thesis 2014.

Appendix A Sample Preparation Procedure

The samples were polished using the procedure outlined below. The samples were etched using Krolls etchant, which consists of 92 ml distilled water, 6 ml Nitric Acid (HNO_3) and 2 ml hydrofluoric acid (HF). The surface of the sample was gently rubbed with a cotton swab dipped in the etchant for less than 15 seconds until the sample turned grey. The sample is then placed in a beaker of water and immediately sprayed with a sodium bicarbonate solution.

Ti-6Al-4V Polishing Procedure
240 grit
320 grit
400 grit
600 grit
6µ diamond spray with activated mastermet on high attack low nap cloth
1µ diamond spray with activated mastermet on high nap cloth
Final polish- colloidal silica